ISSN: 1847-9286
Open Access Journal
www.jese-online.org

JESE

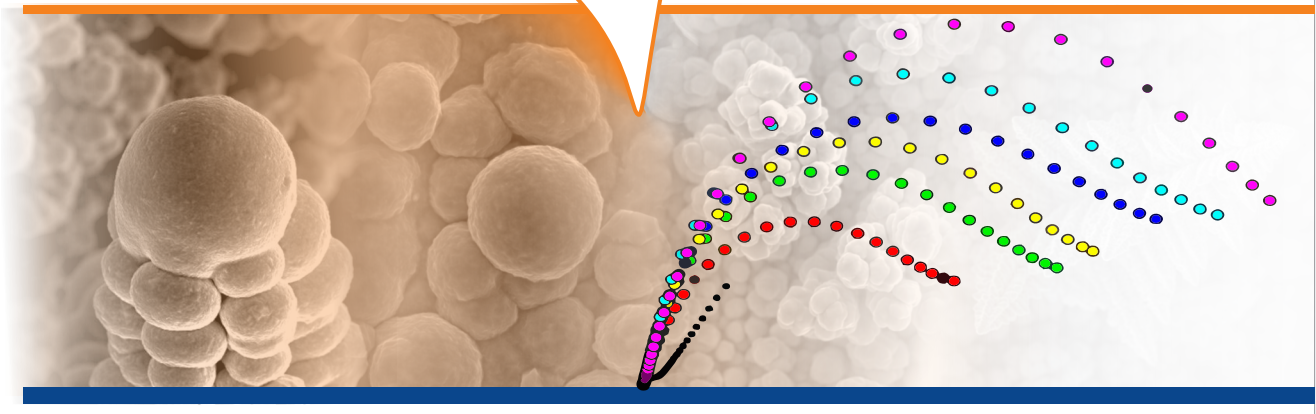

Journal of Electrochemical Science and Engineering

J. Electrochem. Sci. Eng. **7**(**4**) 2017, 153-235

IAPC Publishing

J. Electrochem. Sci. Eng. **7(4)** (2017) 153-166; DOI: http://dx.doi.org/10.5599/jese.419

Open Access : : ISSN 1847-9286

www.jESE-online.org

Original scientific paper

NO_x and propene conversion in $La_{0.85}Sr_{0.15}MnO_{3+d}/Ce_{0.9}Gd_{0.1}O_{1.95}$ symmetrical cells

Anja Zarah Friedberg, Kent Kammer Hansen✉

Department of Energy Conversion and Storage, Technical University of Denmark, DK-4000 Roskilde, Denmark

Corresponding authors E-mail: ✉kkha@dtu.dk, anzf@topsoe.dk

Received: August 14, 2017; Revised: September 23, 2017; Accepted: October 10, 2017

Abstract

The catalytic electrochemical reduction of NO with propene was investigated on $La_{0.85}Sr_{0.15}MnO_{3+d}/Ce_{0.9}Gd_{0.1}O_{1.95}$ symmetrical cells. The electrodes were infiltrated with BaO and Pt. The cells were catalytically active towards the selective catalytic reduction of NO_x with propene, but BaO infiltration lowered the NO conversion, probably because of active-site blocking on $La_{0.85}Sr_{0.15}MnO_{3+d}$. Pt infiltration enhanced the reduction of NOx with propene. When a voltage was applied to the cell with BaO infiltrated electrodes, the NO conversion increased in absence and presence of propene in the feed gas and presence of 10 % O_2. The addition of propene into the feed gas did not enhance the conversion of NO when the electrodes were infiltrated with BaO. When platinum was co-infiltrated with BaO, the catalytic activity towards the reduction of NO with propene was enhanced. However, almost no effect was observed when a voltage was applied. Additionally, when the cells were infiltrated with Pt, an electrochemical promotion was observed with respect to CO_2 formation.

Keywords

NO; Propene; LSM; CGO

Introduction

Diesel engines exhibit better fuel economy than Otto engines and are thus becoming more popular. Otto engines run at a stoichiometric fuel/air ratio, whereas diesel engines operate with excess air. The exhaust contains toxic NO_x, which for engines running under a stoichiometric fuel/air ratio is efficiently removed by the so-called three-way catalytic converter (TWC). A TWC does not operate in the presence of excess oxygen; therefore, NO_x removal from a diesel engine is impossible with a TWC [1]. When removing NO_x under net oxidizing conditions, selective catalytic reduction (SCR) with ammonia/urea and NO_x storage and reduction (NSR) are the most mature technologies.

The use of SCR and NSR technologies is not straightforward. SCR technology requires on-board storage of ammonia and an ammonia slip catalyst. For the NSR technology, sophisticated engine control is needed.

In 1991, Iwamoto and Hamada [2] showed that NO_x was reduced with hydrocarbons via a process referred to as HC-SCR method. This is a potentially attractive technology because hydrocarbons already exist in exhaust gas. The HC-SCR method has been studied on precious metals such as Pt [3–5], metal oxides [6] and Ag [7,8]. It is also possible to reduce NOx with hydrocarbons on zeolites [9–12] and perovskites [13–19]. The main issue with HC-SCR is that the activity is very low. One way to address this issue is to electrochemically promote the reduction of NOx with hydrocarbons.

Electrochemical promotion has been well described in the literature, see *i.e.* [20]. In some cases, the rate of the enhancement in a given reaction during cell polarization is larger than that predicted by Faraday's law. This effect is referred to as the non-Faradaic electrochemical promotion of catalytic activity (NEMCA) or electrochemical promotion (EP), and is due to the back spillover of *i.e*. oxide anions to the electrodes [20]. One defines the rate enhancements factor, ρ, as

$$\rho = r/r_o \quad (1)$$

where r is the reaction rate during polarization and r_0 is the reaction rate at OCV.

NO_x can be removed using an electrochemical reactor that is based on an oxide ion conducting electrolyte. The major drawback of the electrochemical reduction of NO_x is the simultaneous reduction of oxygen at the cathode, which leads to high power consumption. Therefore, both the activity and selectivity are important.

Jayaweera *et al*. [21] investigated the reduction of NO with CO under net oxidizing conditions. Using the perovskite $La_{0.8}Sr_{0.2}Co_{0.9}Rh_{0.1}O_{3-ç}$ as an electrode, they showed that the reaction was electrochemically promoted under net oxidizing conditions. Earlier studies focused on metal electrodes for NO_x reduction, see [20].

The combination of a storage compound (as used in NSR technology) and electrochemical promotion appears to be an attractive solution. Traulsen *et al.* [22] investigated the use of BaO as a storage compound in an all-ceramic electrochemical cell with $La_{0.85}Sr_{0.15}MnO_3/Ce_{0.9}Gd_{0.1}O_{1.95}$ electrodes (LSM_{15}/CGO_{10}) and found that NO could be reduced to N_2 with a conversion of 60 % at 400 °C in the presence of 10 % oxygen. Additionally, perovskites have been suggested as substitutes for Pt in NSR technology [23].

In this work, the influence of adding a reducing agent (propene) to the electrochemical reduction of NO in the presence of a storage compound BaO infiltrated in the cathode is studied. Hydrocarbons are used as reducing agents in NSR technology while an engine is running with a rich fuel/air mixture. Because Pt is normally used as a catalyst for NO oxidation in NSR technology, it is also investigated in this work.

Experimental

Symmetrical cell fabrication

For the evaluation of electrochemical cells for NO conversion with and without propene in the gas feed, symmetrical cells with LSM_{15}-CGO_{10} electrodes, as well as with LSM_{15}-CGO_{10} electrodes infiltrated with BaO, Pt, or BaO and Pt were used. Each of these cells consists of two identical electrodes with a dense CGO_{10} electrolyte. LSM_{15} powder was purchased from Haldor Topsoe A/S,

and CGO_{10} powder was a commercial product of Rhodia. A dense 300-µm-thick sintered tape purchased from Kerafol was used for CGO_{10} electrolyte.

An electrode ink was prepared by mixing 50 wt% LSM_{15} and 50 wt% CGO_{10} powders with terpineol. The mixture was then milled on a planetary mill. Next, an etylcellulose binder was added to the mixture, and the resulting ink was screen printed on the Kerafol electrolyte tape. The cells were then sintered at 1050 °C for 2 h and laser cut to round cells with a diameter of 13 mm. The thickness of the electrodes was approximately 15 µm. Gold was used as the current collector, sputtered-using magnetron sputtering on top of the electrodes to generate a 50 nm porous layer. More details on the sputtering procedure can be found in [24].

The infiltration with BaO was performed using a 0.32 M aqueous solution of $Ba(NO_3)_2$. The solution was prepared using $Ba(NO_3)_2$ from Merck and Millipore water with 1 wt% P123 (BASF) as the surfactant. The cells were soaked in the solution, placed in a vacuum chamber at 0.1 mbar for 15 s and then heated to 700 °C. Pt infiltration was conducted using a 34 mM solution of $Pt(NH_3)_4(NO_3)_2$ (Sigma Aldrich) in Millipore water with 3 wt% of Triton-X45 (Sigma Aldrich) as the surfactant. The infiltration procedure was as previously described, and the cell was dried for several hours at 80 °C before sintering at 300 °C to decompose both the Pt complexes and surfactant. It was not possible to evaluate Pt loading because the weight of the dense electrolyte was much higher than the weight gain obtained as a result of Pt infiltration.

Test setup

Each symmetrical cell was placed in a quartz glass tube in atmospheric pressure setup, and the tube was placed inside a homemade furnace. A gas flow of 2 L/h was fed using Brooks mass flow controllers. The composition of the gas feed was 1000 ppm NO (Air Liquide; 1 % ±0.02 % NO in Ar) + 10 % O_2 (Air Liquide; 20 % O_2 ±2 % Ar) in Ar or 1000 ppm NO (Air Liquide; 1 % ±0.02 % NO in Ar) + 1000 ppm C_3H_6 (Air Liquide; 1 % ±0.02 % C_3H_6 in Ar) + 10 % O_2 (Air Liquide; 20 % O_2 ±2 % Ar) in Ar.

The composition of the outlet gas was monitored and recorded by a chemiluminescence detector (Model 42i HL, Thermo Scientific, USA) for NO and NO_2 detection. The propene, CO, CO_2 and N_2O concentrations were monitored using an Agilent 490 Micro Gas Chromatograph connected to the reactor and equipped with Porapak Q and Molecular Sieve 5X columns and two thermal conductivity detectors.

Microstructure and electrochemical characterization

The structure of the gold current collector layer was investigated with a HITACHI TM 3000 microscope.

A Zeiss Supra 35 scanning electron microscope was used to characterize the microstructure of the electrodes and evaluate the BaO and Pt infiltration.

A Gamry Ref 600 potentiostat-galvanostat was used for the electrochemical measurements. The Gamry was used for applying a voltage and for electrochemical impedance spectroscopy. The impedance spectra were measured in the frequency range from 878787 Hz to 1.3 mHz with 6 points per decade and amplitude of 36 mV rms.

Catalytic and electrocatalytic conversion measurements

The same testing procedure was applied for all the different cells. Each cell was placed in the setup and heated to 300 °C in air. Then, the gas feed was changed to 1000 ppm NO + 10 % O_2, and the pure catalytic conversion of NO and propene was measured.

The electrochemical measurements were conducted as follows: Before and after polarization, impedance spectroscopy measurements were performed to check whether any degradation of the cell had occurred during testing. Polarization measurements were performed for 30 min at +2 V *vs.* open circuit voltage (OCV). The cell was then maintained at the OCV for 30 min or until steady-state was reached, before a new test was performed. The temperature was then increased to 350 and 400 °C, and the procedure was repeated. Afterwards, the gas feed was changed to 1000 ppm NO + 1000 ppm C_3H_6 + 10 % O_2, and the electrochemical tests were repeated.

Results

Structural characterization

Representative images of the gold current collector are shown in figure 1(a) and 1(b). As shown in the figure, the current collector layer is approximately 50 nm thick and is porous as needed.

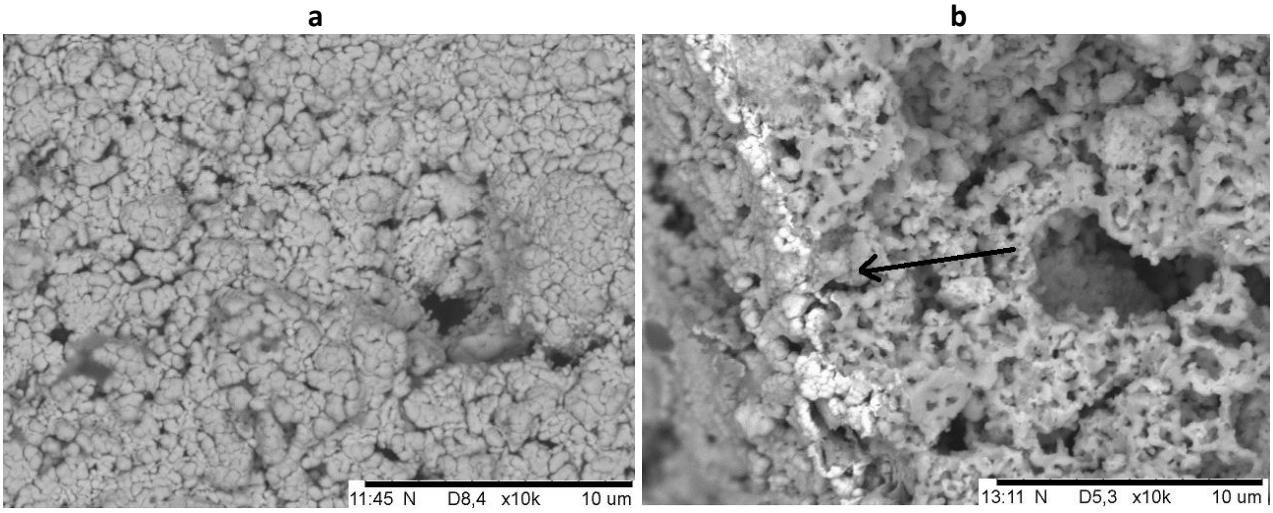

Figure 1. *Microscope images of symmetrical LSM_{15}-CGO_{10} cells: a) Gold-sputtered, porous structure. Top view; b) Gold-sputtered, thin gold layer. Side view*

In figure 2(a) and 2(b), the electrode structure with BaO infiltration is shown. It is seen that before testing, the BaO nanoparticles are distributed evenly on the LSM part of the electrodes (Fig. 2(a)).

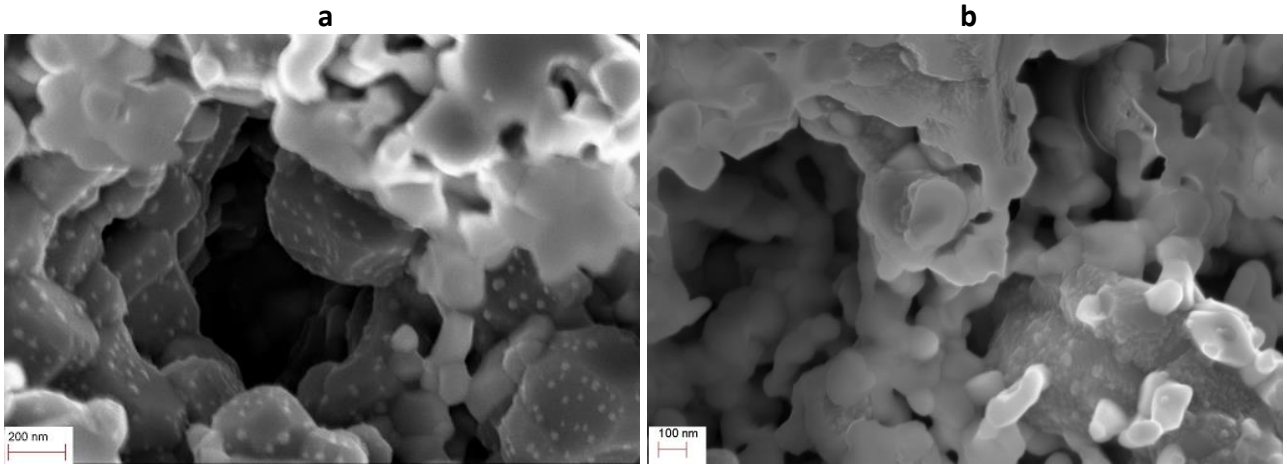

Figure 2. *Microscope images of symmetrical cells with BaO infiltrated LSM_{15}-CGO_{10} electrodes: a) before testing; b) after testing.*

After testing, the BaO nanoparticle structure is fluffier, and the particles have agglomerated, which shows that BaO nanoparticles are undergoing structural changes during testing (Fig. 2(b)).

The cell electrodes infiltrated with both, BaO and Pt appeared similar to those infiltrated with just BaO. No Pt nanoparticles were observed in the SEM images. Other studies [25] have shown that the presence of Pt could not be confirmed with an EDS measurement. This result was attributed to low Pt loading and a small particle size.

Conversion measurements

All cell electrodes showed activity for the catalytic removal of NO_x. Figure 3(a) and 3(b) shows the percentage of NO_x removed in the presence and absence of propene in the gas feed. The four types of electrodes behaved very differently. At the OCV, the non-infiltrated LSM_{15}-CGO_{10} electrodes were most active towards NO removal when propene was present, and NO conversion reached a maximum at 350 °C with a conversion degree of 8 %. When propene was absent in the gas feed, the activity decreased with increasing temperature and the NO conversion decreased to zero at 400 °C.

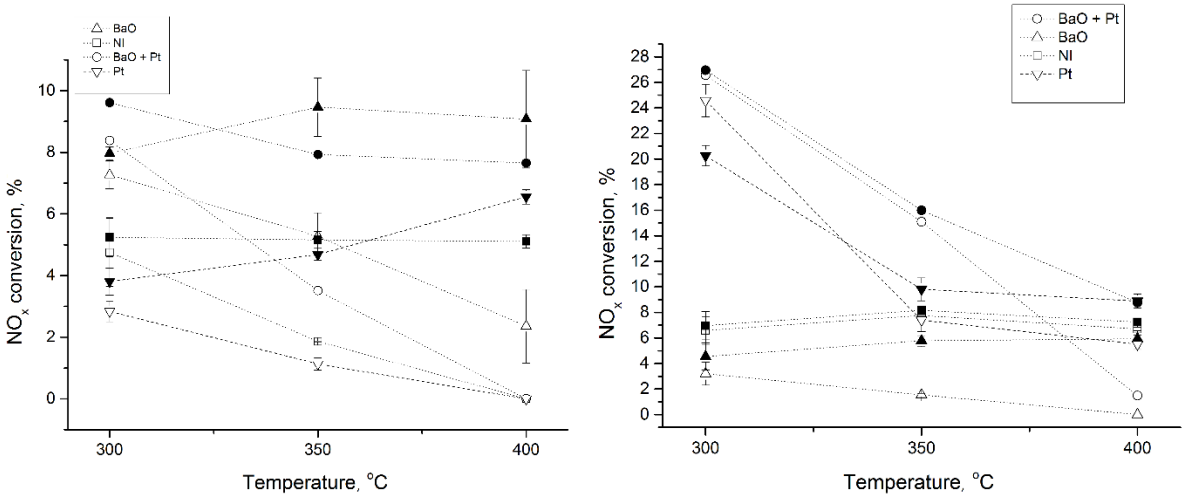

Figure 3. *Percentage of NO_x conversion as a function of temperature in symmetrical cells with non-infiltrated (NI), BaO-infiltrated and BaO + Pt-infiltrated LSM_{15}-CGO_{10} electrodes, measured at the OCV (open symbols) and during + 2 V polarization (solid symbols) in: a) 1000 ppm NO + 10 % O_2; b) 1000 ppm NO + 1000 ppm C_3H_6+ 10 % O_2.*

The activity of electrodes that were infiltrated with BaO decreased with increasing temperature in both atmospheres, being highest when no propene was present in the atmosphere. A conversion degree of up to 8 % was observed. The electrodes co-infiltrated with BaO and Pt revealed a higher conversion degree when propene was present. The results indicate that 27 % of NO_x was removed at 300 °C. The conversion for this cell showed highest decrease with increasing temperature. The catalytic activity of the electrodes that were infiltrated with only Pt showed activity similar to that of the non-infiltrated electrode in NO + O_2 atmosphere. In presence of propene, however, the activity increased to almost the same level as that for the BaO + Pt infiltrated electrodes. During testing in the NO + O_2 atmosphere, no N_2O was detected, and the nitrogen selectivity was 100 %. When propene was added to the gas feed, a small amount of N_2O was detected. The cells containing Pt showed the highest formation of N_2O. N_2O formation decreased with temperature as expected (N_2O is stable only at lower temperatures).

A positive effect of applying a voltage on the conversion of NO_x was observed for all types of cells under certain experimental conditions. The effect was most pronounced in the 1000 ppm NO + 10 % O_2 atmosphere (see figure 3(a) and 3(b), solid points). The selectivity to N_2 was 100 % for the non-infiltrated and Pt-infiltrated electrodes, but a small quantity of N_2O was detected for the electrodes that contained BaO. When propene was added to the feed gas, only a small polarization

effect was observed (see Table 1). The rate enhancement ratio with the polarization of the electrodes infiltrated with only BaO was highest in the presence of propene, but the extra converted NO was almost the same in both atmospheres. At 300 and 350 °C, the polarization effect on the cell with BaO + Pt infiltrated electrodes was low and less than 1 % extra NO was removed. The activity enhancement under polarization of the electrodes with only Pt and atmosphere without propene, was very similar to that of the BaO + Pt electrodes in presence of propene in gas feed, whereas it was much lower in the absence of propene. The amount of N_2O formed during polarization was the same as that at OCV. Thus, it might be argued that the NO_x converted by polarization generates N_2, whereas the NO_x that was catalytically decomposed generates N_2O.

Table 1. Rate enhancement ratio of NO_x conversion for four types of LSM15-CGO10 electrodes

	T / °C	ρ	
Gas composition:		1000 ppm NO + 10 % O_2	1000 ppm NO + 10 % O_2 + 1000 ppm C_3H_6
BaO	300	1.1	1.5
	350	1.9	3.8
	400	6.4	∞
BaO + Pt	300	1.1	1
	350	2.3	1
	400	15.3	6
NI	300	1	1
	350	3	1
	400	∞	1
Pt	300	1.3	1
	350	4.3	1.3
	400	13	1.6

In figure 4(a) and 4(b), the conversions of propene and selectivity to CO_2 for the cells with BaO-infiltrated and non-infiltrated electrodes are plotted as a function of temperature.

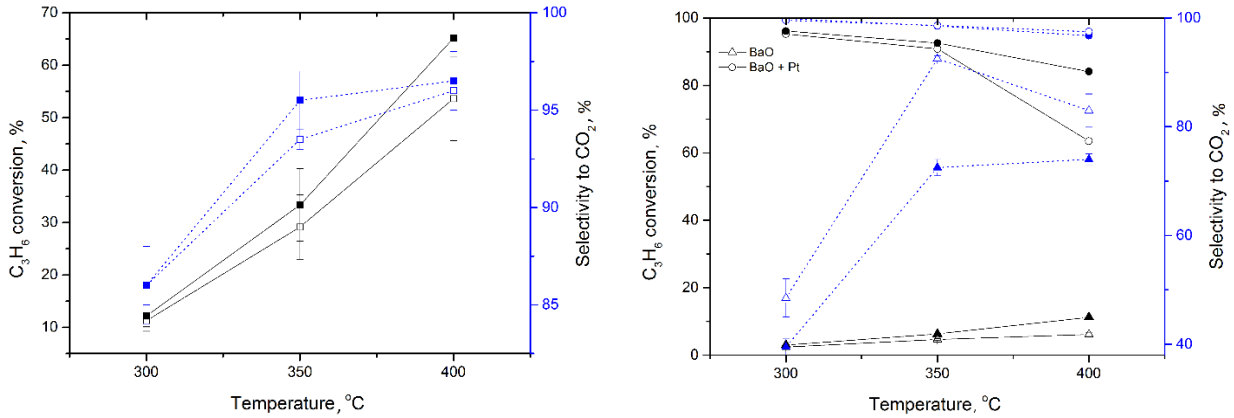

Figure 4. *Temperature dependence of propene conversion (solid lines) and selectivity to CO_2 (dotted lines) in symmetrical cells measured at the OCV (open symbols) and during polarization (solid symbols) for: a) BaO and BaO + Pt-infiltrated LSM_{15} - CGO_{10} electrodes ; b) non-infiltrated LSM_{15} - CGO_{10} electrodes.*

The cells with non-infiltrated electrodes revealed a high catalytic activity, with over 60 % conversion in one of the cells at 400 °C. The cells with BaO-infiltrated electrodes showed a much lower catalytic activity towards the oxidation of propene with the highest value being just below 7 % at 400 °C. The cell with electrodes containing BaO + Pt exhibited a high catalytic conversion, where 95 % of the propene was removed at 300 °C. The conversion of propene decreased with

increasing temperature in this type of cell. The cells with only Pt infiltrated electrodes showed a 100 % conversion of propene, except at 300 °C, where only about 70 % was converted. All propene was oxidized to CO_2 since no CO was detected. For the non-infiltrated electrodes, the selectivity to CO_2 increased with increasing temperature, whereas the selectivity peaked at approximately 350 °C for the BaO-infiltrated electrodes. Almost all propene was oxidized to CO_2 in the cell with BaO + Pt electrodes at 300 and 350 °C.

The propene conversion increased to 74 % at 400 °C for the most active non-infiltrated electrodes when the cell was polarized. Additionally, when the cell was polarized, it was possible to obtain only 11 % conversion at 400 °C for the cell with BaO-infiltrated electrodes. For all the cells, the highest enhancement was obtained at 400 °C, and 84 % of the propene was removed at 400 °C in the cell with BaO + Pt infiltrated electrodes.

Electrochemical impedance spectroscopy

All impedance spectra recorded at the OCV were fitted with equivalent circuits corresponding to three and four arcs appearing in the Nyquist plots, depending on temperature and atmosphere. Most of the arcs were best fitted by an ohmic resistance model in parallel with a constant phase element (CPE). Some of the low-frequency arcs, however, could be fitted using a Voigt element, as they were almost perfect semicircles. The admittance (Y) of a CPE (denoted shortly as Q) is given by:

$$Y = Y_0 (j\omega)^n \quad (2)$$

where Y_0 is a constant, ω is the angular frequency, and n is an exponent. Y_0 and n values are estimated from the fitting of the selected equivalent circuit to the experimentally measured impedance data. The near equivalent capacitance, C_ϖ, values were estimated using the following equation:

$$C_\varpi = (Y_0)^{1/n} R^{(1-n)/n} \quad (3)$$

The impedance spectra were fitted using Elchemea Analytical Software [26]. All impedance spectra were Kramers-Kronig validated before fitting. In the propene-containing atmosphere, the low-frequency part of the impedance spectrum obtained for the cell with BaO + Pt-infiltrated electrodes did not reach steady-state and therefore it was not possible to be fitted. Representative examples of impedance spectra and their spectral deconvolution are shown in figures 5 and 6 for the cells with non-infiltrated and BaO infiltrated electrodes measured at 400 °C.

In all Nyquist plots, two high-frequency arcs, denoted Arc I and Arc II, were observed. When propene was present in the gas feed, a small arc that could not be fitted was found in the high-frequency part of Arc I at 300 °C. Due to the high summit frequencies of Arc I (see Tables 2 and 3), part of this arc is often "dragged" down by the inductance below the real axis. This arc has an activation energy, E_a, of approximately 1 eV, and C_ϖ is independent of the atmosphere and temperature, with a value of $1\times10^{-7} - 9\times10^{-8}$ F/cm^2. Arc II exhibits a low n value (0.44-0.54). For the cells with the BaO-infiltrated and the non-infiltrated electrodes, C_ϖ increased with temperature. This increase was steeper for the cell with BaO-infiltrated electrodes, for which the capacitances were also higher than those for the cell with non-infiltrated electrodes. The resistance of this arc, that concerns the activation energy of the corresponding process, decreased when propene was present in the cells with non-infiltrated electrodes. No dependence on the presence of propene was observed for the resistance of this arc for the cells with BaO-infiltrated electrodes. In all impedance spectra, the dominating arc, denoted as Arc III, was observed in the middle frequency range. The activation energy of the corresponding process increased in the presence of propene for the cells

with non-infiltrated electrodes, whereas no dependence on presence of propene was observed for the cells with the BaO-infiltrated electrodes.

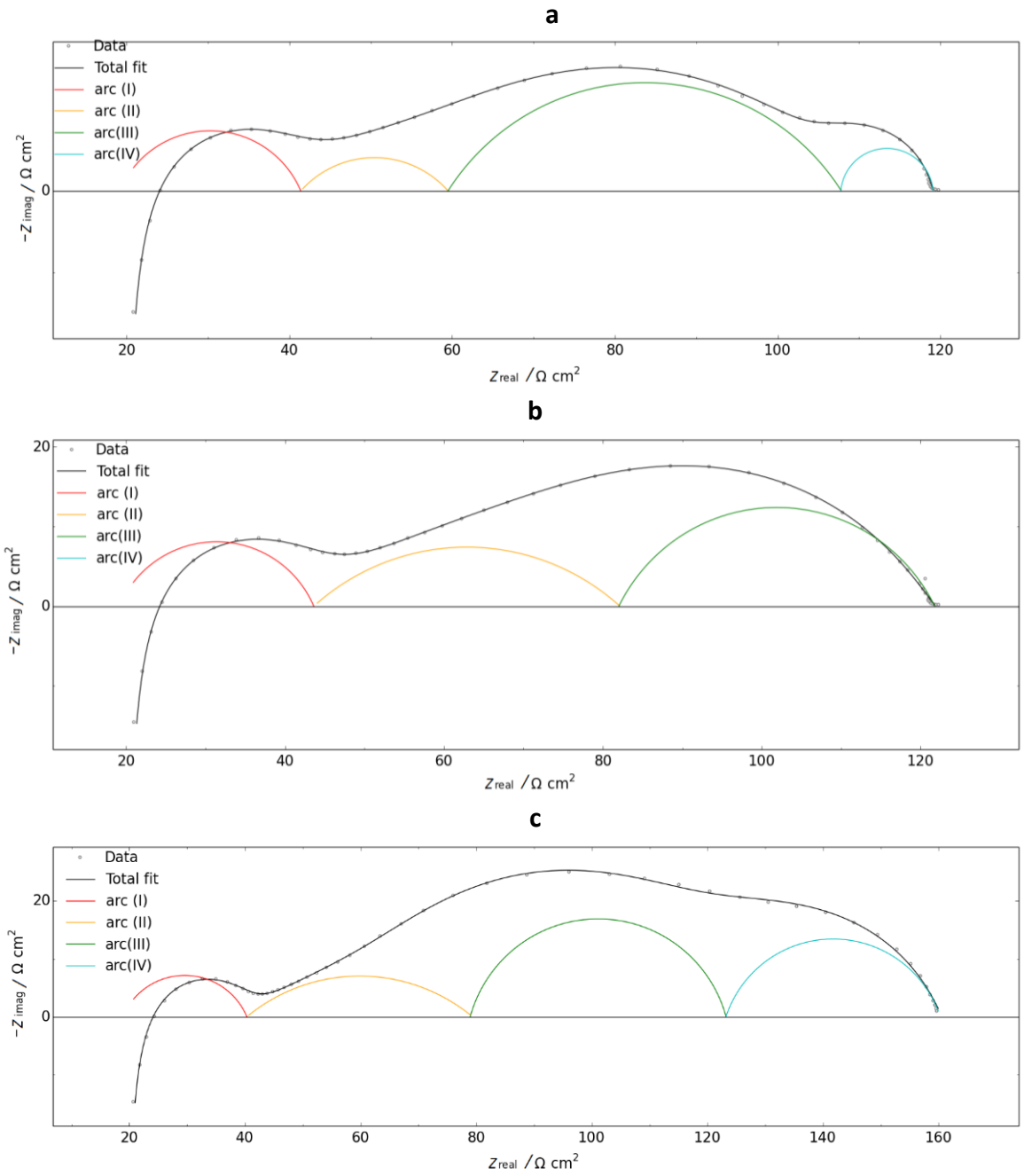

Figure 5. *Nyquist plots of the impedance spectra measured at 400 °C for symmetrical cells with:*
a) non-infiltrated LSM_{15} - CGO_{10} electrodes in 1000 ppm NO + 10 % O_2;
b) non-infiltrated LSM_{15} - CGO_{10} electrodes in 1000 ppm NO + 1000 ppm C_3H_6 + 10 % O_2;
c) BaO-infiltrated LSM_{15} - CGO_{10} electrodes in 1000 ppm NO + 10 % O_2.

It was not possible to fit the high-middle to middle frequency region of the impedance spectrum of the cell with the BaO + Pt infiltrated electrodes with RQ elements having the same *n* (CPE) value at all three temperatures. The fitting results were not improved even after addition of more elements. The *n* values for Arc I and Arc IV (the low-frequency arc) were the same as for the cell with BaO infiltrated electrodes, but the *n* values of Arc II and Arc III changed with temperature. Therefore, no activation energies or capacitance values could be calculated for Arc II and Arc III for this cell. Instead, the total resistance of these two arcs was used to obtain activation energies of

0.91 eV and 0.97 eV in the presence and absence of propene, respectively. A low-frequency arc (Arc IV) with a high *n* value was observed in the impedance spectra of all cells. This arc appeared only in the NO + O_2 atmosphere for the cell with non-infiltrated electrodes, but in the cells with BaO infiltrated electrodes, the arc was observed in both types of gas mixture. This arc was not observed at 300 °C. In all cases, the *n* value of the CPE was the highest at 350 °C. For the cell with non-infiltrated electrodes, the change in *n* value with increasing temperature was small, with *n* decreasing from 0.97 to 0.92. However, the *n* value was higher for the cell with BaO infiltrated electrodes, especially in the presence of propene, where it decreased from 1 to 0.6. The behavior was the same in the BaO + Pt cells. The resistance corresponding to this arc was changed by only a small amount with increasing temperature.

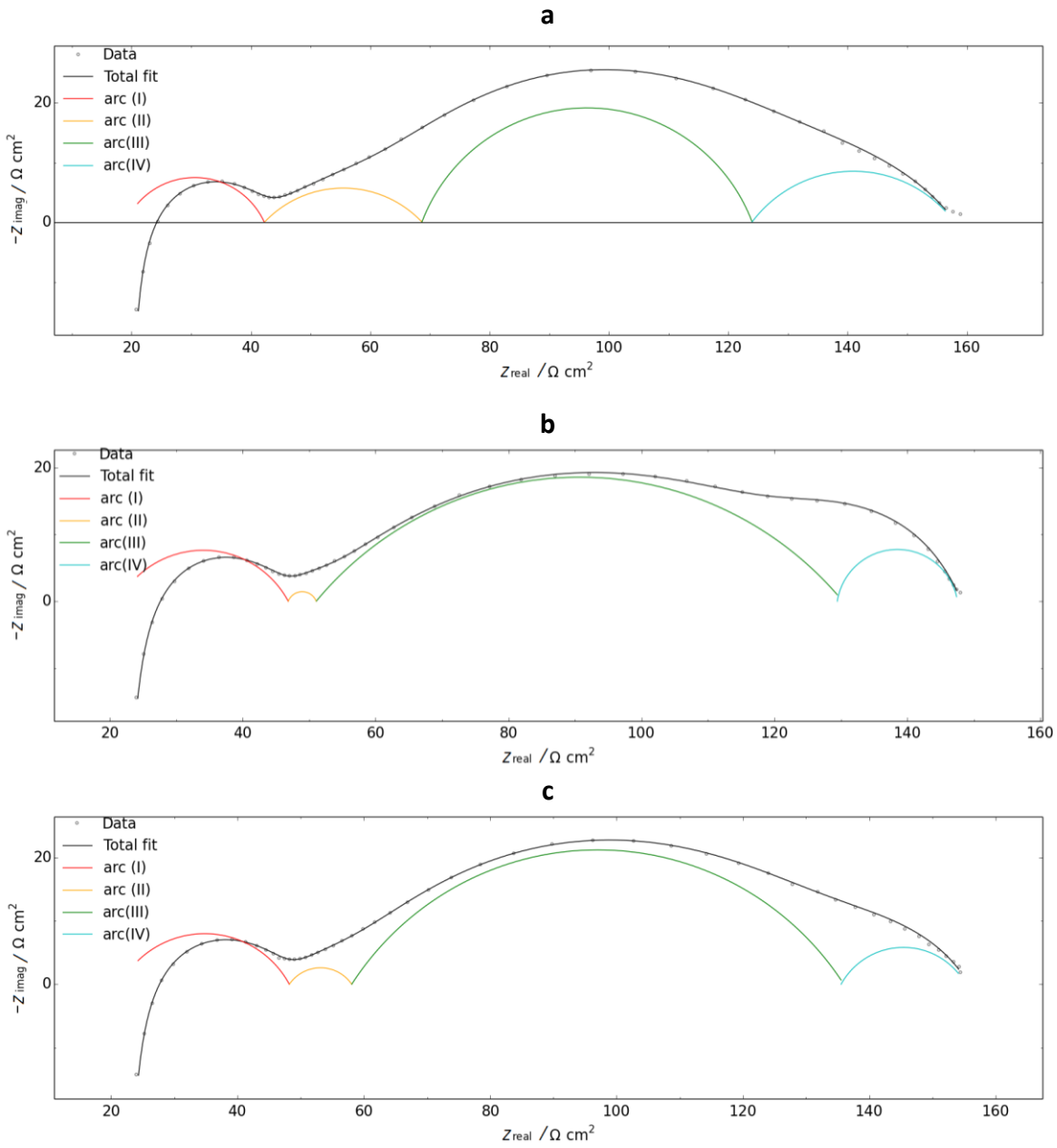

Figure 6. *Nyquist plots of the impedance spectra measured at 400 °C for symmetrical cells with: a) BaO-infiltrated LSM_{15} - CGO_{10} electrodes in 1000 ppm NO + 1000 ppm C_3H_6 + 10 % O_2; b) BaO + Pt-infiltrated LSM_{15} - CGO_{10} electrodes in 1000 ppm NO + 10 % O_2; c) BaO + Pt-infiltrated LSM_{15} - CGO_{10} electrodes in 1000 ppm NO + 1000 ppm C_3H_6 + 10 % O_2.*

Table 2. *Characteristics of the processes corresponding to different arcs of the impedance spectra of the symmetrical cell with non-infiltrated LSM_{15}-CGO_{10} electrodes, measured at 300-400 °C in the atmosphere containing 1000 ppm NO +10 % O_2*

Processes/Arcs	f_{summit} / Hz	C_ϖ / F cm^{-2}	Characteristics
I	4×10^3–9×10^5	~10^{-7} Independent of temperature and atmosphere.	E_a = 0.9 ± 0.06 eV Independent of atmosphere.
II	17-661	$4 \times 10^{-6} - 3.5 \times 10^{-5}$ Increased with increasing temperature. Higher values in the presence of propene.	E_a = 0.75-1 eV Decreases when propene is present. Resistance decreases with polarization. f_{summit} values are higher when propene is present. n = 0.44 – 0.54
III	0.5-19	$1.6 \times 10^{-4} - 6 \times 10^4$ Independent of temperature. Higher values in the presence of propene.	E_a = 0.71-0.92 eV Increases when propene is present. f_{summit} values are independent of atmosphere.
IV			High n value (n = 1) Appears at 350 and 400 °C at OCV in NO + O_2. Appears in the presence and absence of propene. Resistance is independent of temperature.

Table 3. *Characteristics of the processes corresponding to different arcs of the impedance spectra of the symmetrical cell with BaO-infiltrated LSM_{15}-CGO_{10} electrodes, measured at 300-400 °C in the atmosphere containing 1000 ppm NO + 1000 ppm C_3H_6 + 10 % O_2.*

Processes/Arcs	f_{summit} / Hz	C_ϖ / F cm^{-2}	Characteristics
I*	3000-90000	~10^{-7} Independent of temperature and atmosphere.	E_a = 0.94 ± 0.02 eV
II	3-65	5.4×10^{-5} - 2×10^{-4} Increased with increasing Temperature. Higher values in absence of propene.	E_a ~0.95 ± 0.1 eV f_{summit} is higher when propene is present. n = 0.44 – 0.54
III	0.2-2	$9 \times 10^{-4} - 1.6 \times 10^4$ Increased with higher temperatures. Higher values in presence of propene.	E_a = 0.81-0.93 eV Increases when propene is present f_{summit} are independent of atmosphere.
IV*	0.012-0.1		Appears at 350 and 400 °C at the OCV n = 0.6

* including results for the BaO + Pt infiltrated electrode

Discussion

Conversion and the effect of propene

When a voltage was applied to the cells with BaO infiltrated electrodes, the NO_x conversion increased. The enhancement factor, ρ, was highest in a propene atmosphere, but the amount of N_2 formed was almost the same in the presence and absence of propene. A higher ρ observed in the propene-containing atmosphere can be attributed to the lower catalytic activity in this case. The lower catalytic activity in the propene-containing atmosphere suggests that the reduction of NO was inhibited by propene when BaO is used as a storage compound. However, the catalytic activity

of the non-infiltrated electrodes was promoted in the presence of propene, which supports the findings of Hansen *et al.* [13], who found that LSM is a catalyst for the SCR of NO with propene. It is well known that NO_2 is an intermediate in the reduction of NO to nitrogen when using a storage compound. Propene and NO will then compete for the same active sites on LSM. When propene is present, fewer active sites are available for NO oxidation, and BaO will cover some of the active sites on LSM. This coverage could be the reason for the lower activity of BaO infiltrated electrodes in the presence of propene. The catalytic reduction of NO on the BaO + Pt infiltrated electrodes showed a dependence on temperature similar to the other tested electrodes, but NOx conversion was much higher and much more dependent on temperature. For the cells with electrodes infiltrated with Pt and BaO, the higher conversion in the NO + O_2 atmosphere could be attributed to both, the removal via a storage compound and Pt. In the presence of propene, the higher conversion in this cell at high temperatures could be attributed to the excellent oxidation ability of the Pt catalyst. The positive effect of polarization in the propene-containing atmosphere was highest for the cell with BaO-infiltrated electrodes at all three temperatures. However, the total NO_x conversion was low for this type of the cell but equally high as that for the cell with the BaO + Pt infiltrated electrodes when propene is present. The presence of platinum together with BaO in electrodes provided a higher NO conversion in the presence of propene at 300 and 350 °C, compared to electrodes with either Pt or BaO. This finding may indicate that Pt enhances nitrate formation by forming NO_2, which is the step preceding nitrate formation [27]. The higher conversion could also be simply attributed to the sum of the reactions via BaO and Pt. The amount of N_2O found for the cell with the BaO + Pt infiltrated electrodes was much higher than that formed in the cells with electrodes infiltrated only with BaO, where almost nothing was formed when propene was present. The amount of N_2O formed in the cell with BaO + Pt infiltrated electrodes was similar, but still higher than that formed in the cell with electrodes infiltrated only with Pt. The reduction route via the storage compound is still not known for certain [28], but formation of N_2O could suggest that the production from nitrate occurs via Pt, which simply reduces it only to N_2O in the presence of propene. The total conversion of NO_x in the presence of propene was higher on the non-infiltrated electrodes than in BaO infiltrated ones. The reduction of NO could occur via different routes, depending on the nature of the catalyst. The LSM behaved as a catalyst for the SCR of NO with propene, and this reaction was not significantly enhanced by polarization. In the cells with BaO-infiltrated electrodes, the reduction could also proceed via nitrate formation. The formation of N_2 in the presence and absence of propene suggests that nitrate formation was not coupled with propene oxidation. On the Pt containing electrodes, the reduction could proceed via LSM or Pt. In the presence of propene, polarization decreased NO_x conversion on the Pt containing electrodes. This effect might be explained by the behavior of NO_x reduction on Pt, which is known to peak as a function of temperature. This peak occurs at a lower temperature upon polarization [29], which means that if one is looking at only three temperatures, the peak could easily be missed, and the observed behavior can look like if the polarization has a negative effect.

Impedance analysis

The polarization resistance of the cells with non-infiltrated electrodes is similar for the two tested cells, which indicates good reproducibility. In all impedance spectra obtained at 300 °C in the propene-containing gas, a small arc in the high-frequency range was observed. It was not possible to fit the arc, but it was clear that it overlapped with the larger high-frequency arc, referred as Arc I.

Clearly, something occurred in the presence of propene in the atmosphere, which caused this response at high frequencies. At this point, it is not possible to determine the origin of this arc.

The change in the activation energy corresponding to the resistance of the high-frequency arc (Arc I) with the addition of propene can be explained by the presence of this small high-frequency arc. The capacitance and summit frequencies together with an E_a close to 1 eV indicate that oxide ion transport across the interface of the electrode and electrolyte is responsible for this impedance response [30-32].

The near-equivalent capacitance of Arc II was higher in the cells containing BaO infiltrated electrodes. In these cells, the value of C_ϖ decreased when propene was introduced in the atmosphere. The opposite was observed for the cells with non-infiltrated electrodes, in which the presence of propene increased the capacitance. The higher value of C_ϖ for the cell with BaO-infiltrated electrodes can be associated with the presence of BaO and better adsorption of NO on BaO sites compared to LSM sites.

The capacitance value of the Arc II was close to capacitance values associated with oxygen adsorption and dissociation on the composite electrode [22]. The higher capacitance of the cells with BaO-infiltrated electrodes could be related to the production of active oxygen species by reduction of nitrates. The decrease in C_ϖ observed when propene is present in the cell with BaO-infiltrated electrodes could indicate that propene interacts via the above mentioned reaction, which is supported by a decrease in NO reduction in the presence of propene. In the cells with non-infiltrated electrodes, propene could interact with adsorbed oxygen, thereby forming more active oxygen species for dissociation on the electrode surface. The near-equivalent capacitance correlated well with the capacitance values related to oxygen adsorption and dissociation on the electrode surface reported in earlier findings from our group [22,33].

In the case of Arc II, the C_ϖ value of the MF arc (Arc III) observed for the cells with BaO infiltrated electrodes was higher than that for non-infiltrated electrodes. The increase of C_ϖ and decrease of the resistance of this arc with increasing temperature indicates that the responsible process is related to the extension or broadening of the three-phase boundary [34]. The E_a corresponding to this process increased for both cells with the non-infiltrated and BaO-infiltrated electrodes, when propene was introduced in the gas feed. The values of E_a are in good agreement with previous findings of our group [33,35], where the processes related to the corresponding arc were stated as adsorption, surface diffusion and transfer across the triple-phase boundary (TPB). The sensitivity of E_a in the presence of propene was reasonable since different species will adsorb in two atmospheres, while propene is believed to interact with adsorbed oxygen [34]. For these reasons, the Arc III is ascribed to the triple-phase boundary that is related to adsorption, diffusion and/or charge transfer involving oxygen and nitric oxide species.

The change in the *n* values for Arc II and Arc III observed for the cell with BaO + Pt infiltrated electrodes suggests that these arcs represent different processes at different temperatures. In this cell, propene conversion decreased with increasing temperature, opposite to what is expected for a platinum catalyst [29]. This result suggests that something changes in the structure of the cell that inhibited this oxidation reaction. One explanation could be that the BaO nanoparticles which created a fluffier structure after testing covered the platinum nanoparticles, thereby inhibiting the reaction by lowering the number of active sites. This change in microstructure could also lead to a change in the impedance response. Arcs II and III were related to the adsorption, dissociation, and diffusion of surface species at BaO infiltrated and non-infiltrated electrodes. These processes were very dependent on the infiltrated materials.

Adsorption on BaO is believed to proceed through NO_2 [22], whereas the chemisorption of NO is expected on Pt [29,36]. This means that when both, Pt and BaO nanoparticles are present, the adsorption and reduction of NO can proceed via different pathways. The impedance response, shown as Arc II and Arc III, might correspond to a mixture of these processes.

In some of the impedance spectra, a low-frequency arc was found, but not for the cells with non-infiltrated electrodes in the presence of propene. The size of this arc and the *n* value were difficult to be determined from the impedance spectra measured at the OCV. In view of the low activation energy related to this arc, the fact that it appears at low frequencies of impedance spectra of all cells regardless of impregnation material, is in good agreement with the gas diffusion impedance, as described by Mogensen [37].

In both cells with BaO and BaO + Pt infiltrated electrodes, the low-frequency parts of impedance spectra changed at 350 °C and 400 °C. The *n* value of the low-frequency arc was found to be approximately 0.9 in the absence of propene, but it decreased to approximately 0.7 in the presence of propene at 400 °C. It was not possible to create a better fit with additional arcs. The different *n* values of the arcs could represent two different processes at two different temperatures in the presence of propene in the gas phase.

Conclusions

In this work, it was shown that the catalytic reduction of NO by propene on $La_{0.85}Sr_{0.15}MnO_3/Ce_{0.9}Gd_{0.1}O_{1.95}$ (LSM_{15}/CGO_{10}) electrodes in the presence of excess of oxygen was not electrochemically enhanced. However, the direct reduction of NO was enhanced in the presence of excess oxygen. The impregnation of LSM_{15}/CGO_{10} with BaO increased the removal of NO, and an electrochemical enhancement was observed in the absence and presence of propene in the gas feed. No coupling between the oxidation of propene and reduction of NO via BaO was observed. Propene oxidation was inhibited by the presence of BaO nanoparticles on the LSM_{15}/CGO_{10} surface because they covered the active sites for propene oxidation. The impregnation of LSM_{15}/CGO_{10} with Pt significantly enhanced the HC-SCR, but only a minor electrochemical promotion of this reaction was achieved.

References

[1] N. Guillen-Hurtado, V. Rico-Perez, A. Garcia-Garcia, D. Lozano-Castello, A. Bueno- Lopez, *DYNA* **79** (2012) 114-121
[2] M. Iwamoto, H. Hamada, *Catalysis Today* **10** (1991) 57-71
[3] R. Burch, J.P. Breen, F.C. Meunier, *Applied Catalysis B: Environmental* **39** (2002) 283-303
[4] A. Iglesias-Juez, A.B. Hungria, A. Martinez-Arias, A. Fuerte, M. Fernandez-Garcia, J.A. Anderson, J.C. Conesa, J. Soria, *Journal of Catalysis* **217** (2003) 310-323.
[5] A. Obuchi, A. Ohi, M. Nakamura, A. Ogata, K. Mizuno, H. Ohuchi, *Applied Catalysis B: Environmental* **2** (1993) 71-80.
[6] H. Hamada, *Catalysis Today* **22** (1994) 21-40.
[7] E. F. Iliopoulou, A. P. Evdou, A. A. Lemonidou, I. A. Vasalos, *Applied Catalysis A: General* **274** (2004) 179-189.
[8] H. Kannisto, H. Ingelsten, M. Skoglundh, *Journal of Molecular Catalysis A: Chemical* **302** (2009) 86-96
[9] M. Sasaki, H. Hamada, Y. Kintaichi, T. Ito, *Catalysis Letter* **15** (1992) 297-304.
[10] H. Hamada, Y. Kintaichi, M. Sasaki, T. Ito, M. Tabata, *Applied Catalysis* **70** (1991) L15-L20.
[11] G. P. Ansell, A. F. Diwell, S. E. Golunski, J. W. Hayes, R. R. Rajaram, T. J. Truex, A. P. Walker, *Applied Catalysis B: Environmenta,* **2** (1993) 81-100.
[12] K. A. Headon, D. K. Zhang, *Industrial & Engineering Chemistry Research*, **36** (1997) 4595-4599.
[13] K. K. Hansen, E. M. Skou, H. Christensen, T. Turek, *Journal of Catalysis* **199** (2001) 132-140.

[14] X. Wu, L. Xu, D. Weng, *Catalysis Today* **90** (2004) 199-206.
[15] F. C. Buciuman, E. Joubert, J. Barbier, J. C. Menezo, *Applied Catalysis B: Environmental* **35** (2001) 149-156.
[16] R. Zhang, A. Villanueva, H. Alamdari, S. Kaliaguine, *Applied Catalysis A: General* **307** (2006) 85-97.
[17] J. Lentmaier, S. Kemmler-Sack, G. Knell, P. Kessler, E. Plies, *Material Research Bulletin* **31** (1996) 1269-1976.
[18] V. N. Stathopoulos, V. C. Belessi, T. V. Bakas, S. G. Neophytides, C. N. Costa, P. J. Pomonis, A. M. Efstathiou, *Applied Catalysis B: Environmental* **93** (2009) 1-11.
[19] J.C. Menezo, S. Inkari, T. Bertin, J. Barbier, N. Davias-Bainier, R. Noirot, T. Seguelong, *Applied Catalysis B: Environmental* **15** (1998) L1-L4.
[20] C.G. Vayenas, S. Bebelis, C. Pliangos, S. Brosa, D. Tsiplakides, *Electrochemical Activation of Catalysis: Promotion, Electrochemical Promotion, and Metal-Support Interactions*, Kluwer Academic/Plenum Publishers, New York (2001).
[21] P. Jayaweera, A. Sanjurjo, G. Krishnan, E. D. Wachsman, *Solid State Ionics* **136** (2000) 775-782.
[22] M. L. Traulsen, K. B. Andersen, K. K. Hansen, *Journal of Materials Chemistry* **22** (2012) 11792-11800.
[23] C. Hwan Kim, G. Qi, K. Dahlberg, W. Li, *Science*, **327**(5973) (2010) 1624-1627
[24] H. Abdul, J., Mohammed, J. V. T. Høgh, W. Zhang, E. Stamate, K. Thydén, N. Bonanos, *Journal of Power Sources* **212** (2012) 247-253.
[25] J. Shao, *Low Temperature NO_x decomposition using an electrochemical reactor*, Ph.D. Thesis, DTU Energy Conversion, (2013)
[26] Elechemea analytical. http://www.elchemea.com, 2012. Acessed: 2014-07-08.
[27] S. Matsumoto, *CATTECH* **4** (2000) 102-109.
[28] G. Liu, P. Gao. *Catalysis Science &. Technology* **1** (2011) 552-568.
[29] B. Beguin, F. Gaillard, M. Primet, P. Vernoux, L. Bultel, M. Henault, C. Roux, E. Siebert, *Ionics* **8** (2002) 128-135.
[30] M. J. Jorgensen, M. Mogensen, *Journal of Electrochemical Society* **148** (2001) A433-A442.
[31] M. L. Traulsen, K. K. Hansen, *Journal of Electrochemical Society* **158** (2011) P147-P161.
[32] D. Ippolito, K. B. Andersen, K. K. Hansen, *Journal of Electrochemical Society* **159** (2012) P57.
[33] J. Shao, K. K. Hansen, *Journal of Electrochemical Society* **160** (2013) H494-H501.
[34] D. Ippolito, K. K. Hansen, *Journal of Solid State Electrochemistry* **17** (2013) 895-908.
[35] R. M. L. Werchmeister, K. K. Hansen, M. Mogensen, *Journal of Electrochemical Society* **157** (2010) P107-P112.
[36] M. Konsolakis, I. V. Yentekakis, *Journal of Hazardous Materials* **149** (2007) 619-624.
[37] S. Primdahl, M. Mogensen, *Journal of Electrochemical Society* **146** (1999) 2827-2833.

J. Electrochem. Sci. Eng. **7(4)** (2017) 167-179; DOI: http://dx.doi.org/10.5599/jese.460

Open Access : : ISSN 1847-9286

www.jESE-online.org

Original scientific paper

Electrochemical determination of the levels of cadmium, copper and lead in polluted soil and plant samples from mining areas in Zamfara State, Nigeria

Modupe Ogunlesi✉, Wesley Okiei, Aderinsola Adio-Adepoju, Michael Oluboyo

Chemistry Department, University of Lagos, Akoka, Lagos, Nigeria

Corresponding authors E-mail: ✉mayogunlesi@yahoo.com; Tel.: +2348033353238

Received: October 10, 2017; Revised: October 18, 2017; Accepted: October 31, 2017

Abstract

The concentrations of lead, copper and cadmium in soil and plant samples collected from Abare and Dareta villages in Anka local government area of Zamfara State, Nigeria have been electrochemically determined. The study was carried out because of the high mortality of women and children under five, reported for these areas in June 2010. The cause was ascribed to the lead poisoning which has been related to the mining and processing of gold-containing ores. Linear sweep anodic stripping voltammetry technique was used with the glassy carbon working, Ag/AgCl reference and platinum auxiliary electrodes. Voltammetric peaks for lead, copper and cadmium that were observed at -495 mV, -19.4 mV and -675 mV, respectively, have formed a basis for construction of the corresponding calibration plots. The concentrations (in mg/kg) of lead, copper and cadmium in the soil samples were found in the ranges of 18.99−26087.70, 2.96−584.60 and 0.00−1354.25, respectively. The concentration values for lead were far above already established USEPA (2002) and WHO (1996) maximum permissible limits for residential areas. The concentrations of lead, copper and cadmium in the food samples ranged between 5.70−79.91, 11.17−41.21 and 0.00−5.74 mg/kg. Several of these values are found well above the FAO/WHO limits of 0.1, 2 and 0.1 mg/kg, respectively. The results indicate that in addition to the lead poisoning, copper and cadmium poisoning may also be responsible for sudden and high mortality in this population.

Keywords

Heavy metals; Mining activities; Soil; Plants; Anodic stripping voltammetry

Introduction

In June 2010, the Zamfara State Ministry of Health of Nigeria was alerted by Médecins Sans Frontières (MSF) for an increasing number of several deaths and illness among women and children

under five years in some villages in Bukkuyum and Anka local government area. They contacted the United States Centers for Disease Control (US CDC) who deployed a response team to assist in investigating the outbreak. At the same time, the Blacksmith Institute, USA, sent a team from Terra Graphics Environmental Engineering Inc. to conduct an environmental assessment of the area. These teams worked with the national and state authorities, MSF, and the country office of the World Health Organization (WHO). The investigations confirmed severe lead poisoning in more than 100 children in the villages of Dareta and Yargalma, having a mean blood lead concentration of 119 μg/dL. Moreover, soil in and some residential areas in Abare exhibited lead concentrations exceeding 100,000 mg/kg. A random sample of 56 children under 5 years from the villages of Abare and Dareta revealed that over 90 % of them had blood lead concentration $>$ 45 μg/dL and over 70 % had concentrations $>$ 0 μg/dL [1]. A high incidence of convulsions and deaths of young children had been recorded in these villages and lead poisoning was implicated. It is generally thought that lead was introduced in the environment by the illegal mining of gold ores.

In the previous study [2], it was reported that our team visited Abare and Dareta villages and observed various processing activities of the ores which could promote metal contamination of the soil, water and vegetables and may constitute health hazards. These include handling the ores with bare hands, eating with unwashed hands, crushing the ores in residential areas, washing the ores in water bodies, exposure of wells to these ores and sometimes drinking polluted water. The concentrations of lead and copper in water from wells, boreholes, ponds and stream from these villages and environs were already reported [2]. Our observations on the research visit to Abare and Dareta villages attributed pollution of soils in the residential areas and farms to the practices of bringing the ores to the residential areas where they are crushed, and irrigating of farmlands by the water already used in processing the ores.

High concentrations of heavy metals in soil would increase potential uptake of these metals by plants and their entering into the food chain [3]. Contamination of food chain becomes increasingly important in a view of its role in human health and nutrition [3-7]. The main threats to human health from heavy metals are associated with exposure to lead, copper, cadmium, mercury and arsenic. These metals may enter the human body through inhalation of dust, consumption of contaminated drinking water and ingestion of food plants grown in contaminated soils [8,9]. The uptake of metals by plants can be affected by several factors which include metal concentrations in soils, soil pH, soil texture, cation exchange capacity, organic matter content of soils as well as the age of the plants [10-12]. Mining activities have been reported to have adverse effects on water resources and farmlands [13] and this could lead to accumulation of heavy metals in plants grown in such contaminated soils.

The aim of this study is to ascertain the level of heavy metal contamination of the soils and plants such as guinea corn and maize seeds in Abare, Dareta and environs, using linear sweep anodic stripping voltammetry technique which offers high sensitivity and rapid response time.

Experimental

Collection of soil samples

Soil samples were collected from 30 sites in Abare, Dareta and environs in July 2010. Sampling was done in a 'W' fashion at sites 10 m apart. Soil samples were taken at 5 cm depth. The sampling sites designated DA 01−10 and AB 05−10 were residential areas in Dareta and Abare, where grinding of the ore was carried out. The mining sites in Dareta were designated DA 11−15. The areas around a pond and at the bank of a stream in Abare where the ores were washed are designated AB 01−05

and AB 11−15, respectively. The coordinates of the sampling stations were recorded using a Garmin 38 global positioning system (GPS) device. About 500 g of each soil sample was collected in polythene bags and labeled. Each sample was then air-dried, sieved (size 2.3 mm) and stored in an air tight glass jar.

Collection of plant samples

Samples of various plants and food items were collected from Abare and Dareta in July 2010. The items which included guinea corn and millet leaves were collected randomly from 50 plants in Dareta. The guinea corn leaves and the millet leaves were each mixed thoroughly before analysis. Elephant grass was obtained from the area of cattle grazing in Abare. Guinea corn and millet seeds were purchased from the homes in Abare and Dareta, while the maize and beans were purchased from the homes in Abare.

Preparation of soil samples

1.0 g of each soil sample was added to 20 cm^3 of a mixture of concentrated HNO_3 and H_2O_2 (30 %) (Sigma-Aldrich) in the ratio 3:1. The mixture was heated gradually to 120 °C and kept at this temperature for 2 hours till a clear solution was obtained. The solution was allowed to cool and filtered into a 50 cm^3 standard flask and supplemented with deionized water before transferring to a pre-cleaned plastic bottle.

Preparation of plant samples

The samples were air-dried in a dust-free environment for three weeks and pulverized using a domestic blender. The digestion of samples was carried out by sequential treatment with 65 % HNO_3 and $HClO_4$ (Sigma-Aldrich) according to the method earlier reported [14]. 1 g of the fine powder of the sample was digested with 20 cm^3 of 65 % HNO_3 at 80 °C for one hour. On cooling, 2 cm^3 of 70 % $HClO_4$ was added and digested again at 250 °C, until a clear solution was obtained. The mixture was allowed to cool and 20 cm^3 of deionized water was added. It was filtered into a 100 cm^3 standard flask, supplemented with deionized water and stored in a pre-cleaned plastic container for the heavy metals analysis which was carried out in triplicate within 24 h.

Voltammetric measurements

A Basi-Epsilon potentiostat/galvanostat was used in the study. The concentrations of heavy metals were determined by linear sweep anodic stripping voltammetry technique [2,15]. The working electrode (3 mm diameter) was glassy carbon, while platinum electrode (1.6 mm diameter) served as the auxiliary electrode and Ag/AgCl as the reference electrode. The working electrode was polished with alumina powder to obtain a mirror-like image, washed with de-ionized water and placed in a pyranha solution for 2 min, washed with de-ionized water and dried.

Calibration curve

Standard solution of each metal was prepared by dissolving the weighed amount of the salt (0.1598 g of $Pb(NO_3)_2$), (0.3929 g of $CuSO_4{\times}5H_2O$) and 0.2745 g of $Cd(NO_3)_2{\times}4H_20$), (all from Sigma-Aldrich) in 100 cm^3 of deionized water to give 1000 ppm of lead, copper and cadmium, respectively. From these solutions, serial dilutions were made with 0.1 M acetate buffer, pH 4.50 containing 80 ppm $Hg(NO_3)_2$ and 0.2 M KNO_3 to give the working concentrations of 250, 500, 1000, 2000 and 2500 ppb of each metal. These diluted solutions were used to obtain the calibration curves. For this purpose, 10 cm^3 of each of the standard solution of the metal was transferred into the electrochemical cell and purged with nitrogen for 10 min. The pre-concentration of the metal was

carried out at -900 mV for 120 s with stirring and after a quiet time of 30 s, the stripping process was carried out by scanning the potential from -900 mV to 200 mV at the scan rate of 20 mV/s. Peak currents for lead, copper and cadmium were observed at -495 mV, -19.4 mV and -675 mV, respectively. These peak current values were used to construct the calibration plots for determination of the concentrations of Pb, Cu and Cd.

Analysis of samples

5 cm^3 of each digested soil or plant sample was transferred into the electrochemical cell and 5 cm^3 of 0.2 M acetate buffer, pH 4.50, containing 160 ppm $Hg(NO_3)_2$ and 0.2 M KNO_3 was added and mixed thoroughly. The solution was purged with nitrogen for 10 min and the potential scanned as described for the standard solutions. The values of the peak current obtained at -495 mV, -19.4 mV and -675 mV were used to determine the concentrations of Pb, Cu and Cd in the samples.

Results

Similarly to already described determinations of calibration plots for Pb and Cu [2], Figure 1 shows the overlay of voltammograms of standard solutions of Cd, while Figure 2 shows the calibration plot for Cd in the concentration range of 250−2000 ppb.

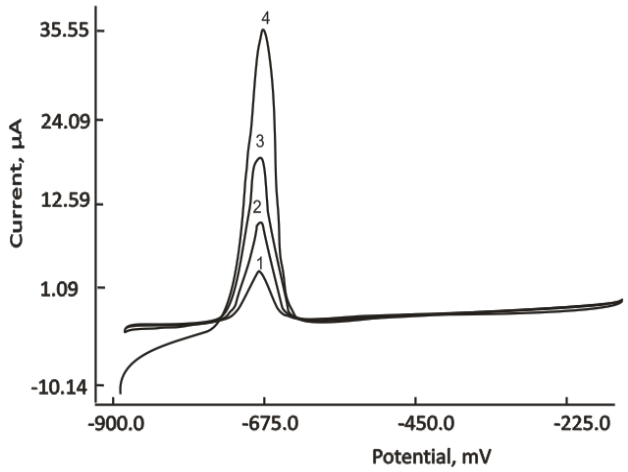

Fig. 1. *Overlay of the voltammograms obtained for standard solutions of $Cd(NO_3)_2 \times 4H_20$ in 0.1M acetate buffer, pH 4.5 containing 80 ppm $Hg(NO_3)_2$ and 0.2 M KNO_3. Cd concentration: 250 ppb (1), 500 ppb (2), 1000 ppb (3), 2000 ppb (4).*

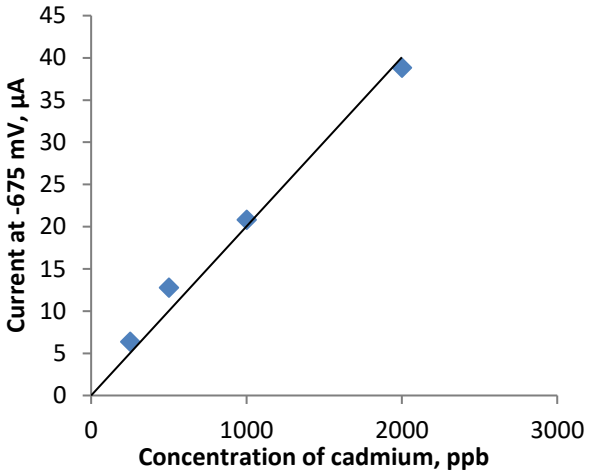

Fig. 2*. Calibration plot of peak currents at -675 mV against Cd concentration in 0.1 M acetate buffer pH 4.50, containing 80 ppm $Hg(NO_3)_2$ and 0.2 M KNO_3.*

The voltammograms obtained for the determination of metals in soil samples AB 04 and AB 13 are shown in Figures 3 and 4, respectively.

Figures 5 and 6 show voltammograms for the determination of Pb, Cu and Cd in millet leaves and guinea corn from Dareta.

The results showing the concentrations of Cu, Cd and Pb in soils from the various sampling sites are presented in Table 1, while the corresponding results for the plants are listed in Table 2.

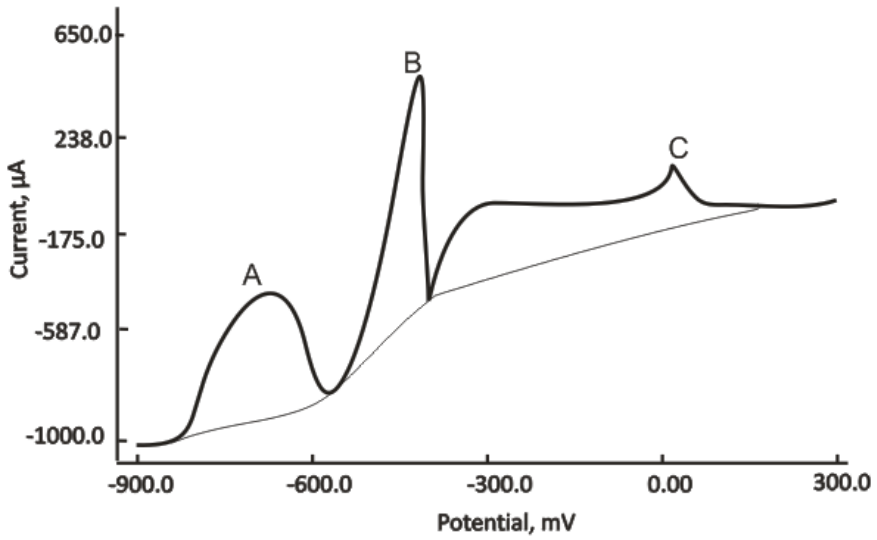

Fig. 3. *Voltammograms of the soil sample from Abare AB 04 in 0.1 M acetate buffer, pH 4.5 containing 80 ppm $Hg(NO_3)_2$ and 0.2 M KNO_3. Peaks A, B and C correspond to Cd, Pb and Cu respectively.*

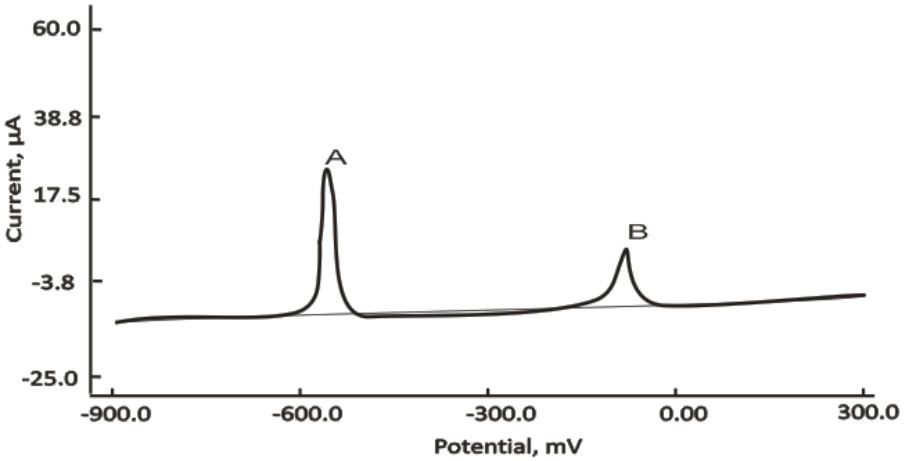

Fig. 4. *Voltammogram of the soil sample from Abare, AB 13 in 0.1 M acetate buffer, pH 4.5 containing 80 ppm $Hg(NO_3)_2$ and 0.2 M KNO_3. Peaks A and B correspond to Pb and Cu, respectively.*

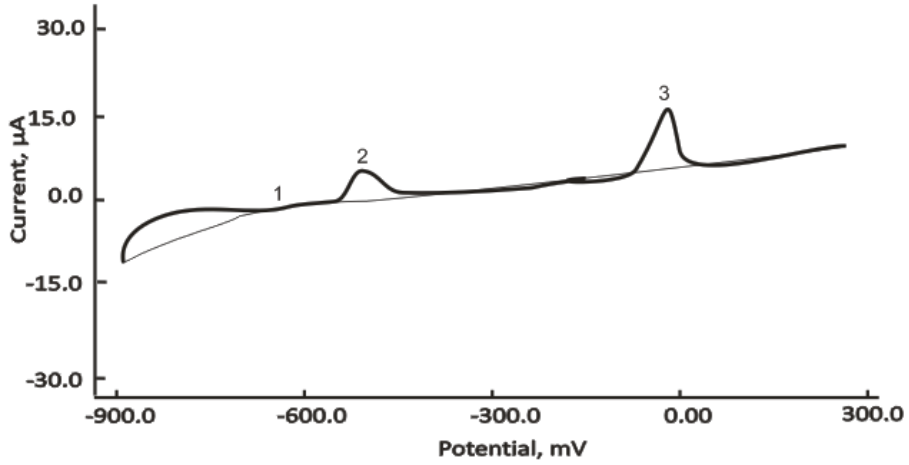

Fig 5. *Voltammogram of millet leaves from Dareta in 0.1M acetate buffer, pH 4.5, containing 80 ppm $Hg(NO_3)_2$ and 0.2 M KNO_3. Peaks 1, 2, and 3 correspond to Cd Pb and Cu*

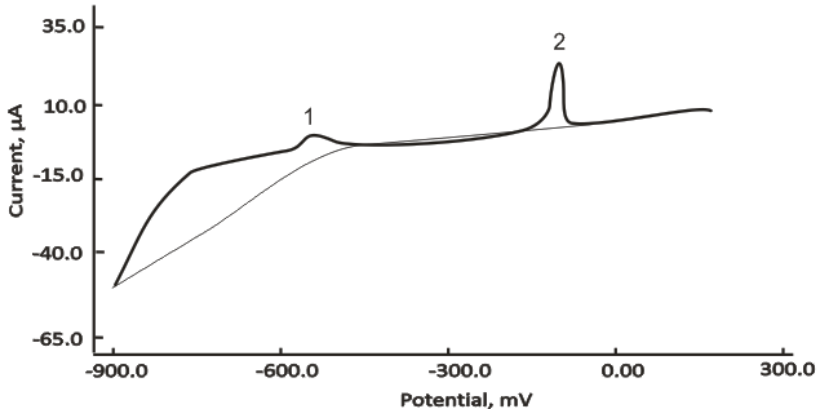

***Fig. 6**. Voltammogram of guinea corn seed from Dareta in 0.1 M acetate buffer pH 4.5, containing 80 ppm $Hg(NO_3)_2$ and 0.2 M KNO_3. Peaks 1 and 2 correspond to Pb (-495 mV) and Cu (-19.4 mV)*

***Table 1.** Concentrations of Pb, Cu and Cd in soil samples from Dareta and Abare villages in Zamfara State*

Soil sample	Coordinate	Content of Pb, mg/kg	Content of Cu mg/kg	Content of Cd, mg/kg
DA 01 (Grinding site)	N 12⁰ 01'50.2'' E 005⁰ 57'30.5''	1175.00 ± 8.40	36.604 ± 6.00	ND
DA 02(Grinding site)	N 12⁰ 01'42.6'' E 005⁰ 57'18.7''	40.04 ± 1.10	2.96 ± 0.28	ND
DA 03(Grinding site)	N 12⁰ 01'41.6'' E 005⁰ 57'18.7''	36.16 ± 0.18	10.86 ± 1.80	ND
DA 04(Grinding site)	N 12⁰ 01'29.6'' E 005⁰ 57'44.0''	18.99 ± 0.70	32.84 ± 0.50	ND
DA 05(Grinding site)	N 12⁰ 01'39.5'' E 005⁰ 57'32.1''	21.06 ± 0.24	6.56 ± 0.11	ND
DA 06(Grinding site)	N 12⁰ 01'51.8'' E 005⁰ 57'21.3''	26087.70 ±16.20	78.51 ± 1.66	ND
DA 07(Grinding site)	N 12⁰ 01'51.7'' E 005⁰ 57'21.2''	438.56 ± 2.20	9.73 ±1.27	ND
DA 08(Grinding site)	N 12⁰ 01'52.0'' E 005⁰ 57'20.9''	438.56 ± 1.30	9.73 ± 0.54	ND
DA 09(Grinding site)	N 12⁰ 01'51.7'' E 005⁰ 57'21.2''	701.30 ±0.91	33.26 ± 1.20	ND
DA 10(Grinding site)	N 12⁰ 01'51.8'' E 005⁰ 57'21.0''	339.46 ± 1.10	38.69 ± 1.10	ND
DA 11(Mining site)	N 12⁰ 01'15.8'' E 005⁰ 57'34.0''	1128.51 ± 26	123.08 ± 2.91	804.50 ± 5.60
DA 12(Mining site)	N 12⁰ 01'15.3'' E 005⁰ 57'34.3'	630.70 ± 1.22	54.30 ± 1.80	ND
DA 13(Mining site)	N 12⁰ 01'15.0'' E 005⁰ 57'34.0''	167.54 ± 1.00	54.30 ± 1.40	ND
DA 14(Mining site)	N 12⁰ 01'14.7'' E 005⁰ 57'34.0''	3760.96 ± 4.1	213.80 ± 2.80	1354.25 ± 7.50
DA 15(Mining site)	N 12⁰ 01'14.9'' E 005⁰ 57'34.2''	481.14 ± 6.50	48.64 ± 1.80	ND
AB 01(Washing site)	N 12⁰ 04'41.2'' E 005⁰ 57'29.1''	900.40 ± 1.30	92.53 ± 3.50	ND
AB 02(Washing site)	N 12⁰ 04'42.1'' E 005⁰ 57'30.6''	4051.76 ± 28	458.37 ± 1.50	ND
AB 03(Washing site)	N 12⁰ 04'41.5'' E 005⁰ 57'29.0''	606.14 ± 2.80	33.71 ± 2.50	ND
AB 04(Washing site)	N 12⁰ 04'41.2'' E 005⁰ 57'29.7''	3720.62 ± 3.00	584.60 ± 2.85	1216.25 ± 9.50
AB 05(Washing site)	N 12⁰ 04'40.6'' E 005⁰ 57'29.2''	390.79 ± 5.10	50.91 ± 3.50	ND
AB 06(Grinding site)	N 12⁰ 04'41.3'' E 005⁰ 57'26.2''	38.16 ± 0.87	15.16 ± 1.25	ND
AB 07(Grinding site)	N 12⁰ 04'40.7'' E 005⁰ 57'26.2''	489.48 ± 1.80	17.19 ± 0.68	ND

Soil sample	Coordinate	Content of Pb, mg/kg	Content of Cu mg/kg	Content of Cd, mg/kg
AB 08(Grinding site)	N 12^0 04’41.3’’ E 005^0 57’26.4’’	111.899 ± 2.10	24.35 ± 1.35	ND
AB 09(Grinding site)	N 12^0 04’40.7’’ E 005^{0}57’26.8’’	1615.79 ± 3.20	49.10 ± 3.50	ND
AB 10(Grinding site)	N 12^0 04’41.3’’ E 005^0 57’27.0’’	207.89 ± 1.85	10.86 ± 1.67	ND
AB 11(Washing site)	N 12^0 04’22.7’’ E 005^0 57’28.3’’	287.54 ± 0.87	92.69 ± 2.50	8.03 ± 1.35
AB 12(Washing site)	N 12^0 04’21.7’’ E 005^0 57’27.6’’	1323.68 ± 4.51	204.52 ± 3.45	ND
AB 13(Washing site)	N 12^0 04’23.1’’ E 005^0 57’28.8’’	205.56 ± 1.25	40.04 ± 2.31	ND
AB 14(Processing site)	N 12^0 04’22.9’’ E 005^0 57’29.3’’	390.79 ± 3.10	69.91 ± 1.40	ND
AB 15(Washing site)	N 12^0 04’23.1’’ E 005^0 57’29.5’’	51.586 ± 1.20	23.55 ± 1.48	ND

ND: Not detected.

Table 2. *Concentrations of metals in samples of plants and food from Abare and Dareta, Zamfara State.*

Plant/food SAMPLE	LOCATION	Content of Pb, mg/kg	Content of Cu mg/kg	Content of Cd, mg/kg
Elephant grass	Abare	24.63 ±0.05	27.37 ± 0.08	ND
Guinea Corn seeds	Abare	15.60 ± 0.15	11.17 ± 0.07	ND
Maize	Abare	24.56 ± 0.04	12.72 ± 0.06	5.74 ± 0.13
Beans	Abare	10.64 ± 0.05	30.41 ± 0.10	ND
Millet seeds	Abare	5.70 ± 0.06	14.84 ± 0.06	ND
Guinea corn seeds	Dareta	79.91 ±0.07	41.21 ± 0.05	ND
Guinea corn leaves	Dareta	36.86 ± 0.10	19.05 ± 0.03	ND
Millet seeds	Dareta	22.29 ± 0.09	11.53 ± 0.10	ND
Millet leaves	Dareta	22.76 ± 0.09	40.58 ± 0.20	5.34 ± 0.08
FAO/WHO (2011)	--	0.1	2	0.1

ND: Not Detected

Discussion

Soil analysis

The concentration levels of Pb, Cu and Cd in soil samples listed in Table 1 can be considered based on the processes carried out at each specific location. DA 01−10 are residences where grinding of ores is carried out by women and children. DA 11−15 denote the mining sites located 3.5 km from Dareta. Sites AB 01−05 are located around a pond in Abare. Sites AB 06−10 are grinding areas located in residences in Abare, while AB 11−15 are sites located by the stream in Abare where the processors wash the powdered ores to obtain gold.

Data in Table 1 show that in the residential areas in Dareta (DA 01−DA 10), concentrations of Pb were detected in the range 18.99-26087.70 mg/kg, Cu was detected in the range 2.96−78.51 mg/kg, while Cd was not detected at all. At the mining sites in Dareta (DA 11−DA 15), the levels of Pb and Cu were in the range 167.54−3760.96 mg/kg and 48.64−123.08 mg/kg, respectively. Cadmium was found at two mining locations in Dareta (DA 11 and DA 14) in concentrations of 804.50 mg/kg and 1354.25 mg/kg, respectively. At the pond environ sites in Abare (AB 01−AB 05), the levels for Pb and Cu were in the range 390.79−4051.76 mg/kg and 33.71−584.60 mg/kg, respectively, while Cd was found at one site (AB 04) in the concentration of 1216.25 mg/kg. The levels of Pb and Cu at grinding

sites of residential areas in Abare (AB 06−AB 10) were detected in the range of 38.16−1615.79 mg/kg and 10.86−49.10 mg/kg, respectively. Cadmium was not detected in these samples. At the ore washing sites in Abare (AB 11−AB 15) at the bank of a stream, the levels of Pb and Cu were detected in the range 51.59−1323.68 mg/kg and 23.55−204.52 mg/kg, respectively. Cadmium in the concentration of 8.03 mg/kg was found at only one site in Abare (AB 11).

The permissible level of Pb in soil of residential areas in the US is 400 mg/kg [16,17]. This value is exceeded in a home in Dareta (DA 01) and grinding sites in Dareta (DA 06−09), and is probably due to the volume of ore being processed over time. The concentration values for Pb, Cu and Cd are comparable for the residential grinding sites DA 01−05 and DA 07−10 in Dareta and AB 06−10 (36.16−1615.79 mg/kg) in Abare. DA 06 appears to be an isolated case. It is pertinent to note that even though there is no mine in Abare, the inhabitants of the two villages appear to be processing about similar quantities of ores. With the exception of site DA 13, the levels of Pb at the mining sites in Dareta (DA 11−15) exceeded the USEPA limit. It should be noted that the site DA 14 is located at the entrance of the main mining site. The mining activities have severely polluted this site and are responsible for the very high level of Pb observed in DA 14 (3760.96 mg/kg). In the pond environment in Abare (AB 01−05), the Pb levels in the soil were very high, with 4051.76 mg/kg and 3720.62 mg/kg detected at sites AB 02 and AB 04, respectively. This may be due to the gathering of processors at these sites. The levels of Pb were moderately high at AB 01 and AB 03 showing values of 900.40 mg/kg and 606.14 mg/kg, respectively. At powdered ore washing sites in Abare (AB 11−15), high levels of Pb were found at AB 12 (1323.68 mg/kg) and AB 15 (51.586 mg/kg). It is significant that these values were recorded in Abare where there are no mines. However, the stream and pond in Abare are both used by the two communities for the washing of the ores. The high concentration value of Pb found at AB 15 maybe due to several processors who converge at this site.

The permissible limit for Cu in the soil of residential areas is 190 mg/kg [18]. Data in Table 1 show that Cu levels in the soil samples from Dareta were under the permissible limit except for DA 14 located at the mining site, where 213.8 mg/kg was detected. In Abare, this permissible limit was highly exceeded at pond sites (AB 02 and AB 04) with the values of 458.37 and 584.60 mg/kg, respectively and marginally exceeded in the residential processing site (AB 12) where 204.52 mg/kg of Cu was detected.

The permissible limit of Cd in the soil is 12 mg/kg [18]. Cadmium was not detected in soil samples taken from the residences in Dareta (DA 01−10), but two sites in the mining areas (DA 11 and DA 14) showed Cd levels of 804 and 1354 mg/kg, respectively. These concentrations of Cd were 67 and 113 times higher than the permissible limit. Cadmium was also detected at two locations in Abare (AB 04 and AB 11). High level of 1216.25 mg/kg found in AB 04 is 101 times higher than the permissible limit, while the level of Cd in AB 11 is under the limit. It is pertinent to note here that all sites where Cd was detected (DA 11, DA 14 and AB 04), exhibited high levels of Pb too.

In summarizing the results given in Table 1, it can be said that more than 50 % of the soil samples collected from Dareta and Abare were contaminated by Pb, 20 % by Cu and 12 % by Cd. This is in agreement with the Joint United Nations Environment Programme−Office for the Coordination of Human Affairs (UNEP/OCHA) Environmental Unit (JEU) report [19] on lead pollution and poisoning crisis in Zamfara State. This report showed that the top soil collected from various locations in Dareta and Abare were heavily polluted by Pb. At a processing site near a mosque in Abare, the Pb level in the soil was reported as 1210 mg/kg, while for the top soil from a near site close to a private well, the Pb level of 27000 mg/kg was reported. The UNEP/OCHA study has also reported Pb levels

of 23600 mg/kg in top soil from a grinding site in Abare and 37500 mg/kg in top soil from a processing site near a well in Dareta [19]. However, the UNEP/OCHA study did not report any pollution of the soil by Cu and/or Cd.

A study on the assessment of lead, mercury and arsenic levels in soils of Dareta, Bagega, Sunke, Abare and Yargalma villages in North−Western Nigeria was reported in 2014 [20]. Lead concentrations in soil samples were found to be in the range of 6.91−4157 mg/kg. The average concentration of Pb in farmlands in Abare was reported to be 515 mg/kg [21].

The results of all these studies, as well as those presented in this report show that top soil in several parts of Abare and Dareta residences are heavily polluted by Pb as a result of mining activities. In a household survey carried out by Blacksmith Institute, 2011 in two villages, Dareta and Yargalma in Anka area, it was reported that 66 % of the population in the villages undertook at least one mining activity within their residences [22]. These mining activities include crushing of the ore, grinding, washing, drying, extracting gold with mercury and/or melting gold. The results of the study show the impact of anthropogenic activities on abundance of potentially harmful elements in the soils of the area. The mining activities exposed the women and children to high levels of Pb in the soil and this may be responsible for the mean blood lead concentration of 119 µg/dL found in children from these villages. Blood levels as low as 10 µg/dL are associated with impaired neurological development in young children [23].

In the present paper, the levels of Cu were generally found under the limit at most of the sites. However, prolonged exposure to these metals could lead to bioaccumulation. Some of the most commonly reported adverse health effects of Cu are gastrointestinal distress, nausea, vomiting, abdominal pain irritation of the respiratory tract, coughing, sneezing and pulmonary fibrosis [24]. The levels of Cd found at two sites in Dareta (DA 11 and DA 14) and one site in Abare (AB 04) are excessively high and pose a health risk to the processors in these sites. The kidney is the main organ affected by the chronic Cd exposure and toxicity. Cadmium accumulates in the kidney which may result in renal failure [25].

In a study carried out in 2014, on discharges of potentially harmful elements (PHEs) in soils from various sites in Anka Local Government Area where artisanal mining for gold was carried out, concentrations of Pb equal to 2637, 1960, 3920, 290 and 3326 mg/kg were reported for mine site, ore processing site and village square, respectively [26]. The corresponding values for Cu at the same places were reported as 159, 159, 117, 29 and 223 mg/kg, while the corresponding values for Cd were reported as 4.5, 8.7, 3.6, 0 and 6.9 mg/kg.

In our study, the corresponding values for Pb shown in Table 1 for the mining sites (DA 11–DA 15) and residential processing sites (DA 01–DA 10 and AB 06–AB 10) ranged between 167−3761 and 19−1615 mg/kg, respectively. Here, the highest value of 26088 mg/kg was observed at only one location (DA 06). The corresponding values for Cu ranged between 49−214 mg/kg at the mining sites and between 3−49 mg/kg for the residential sites, respectively. It should be noted that 79 mg/kg of Cu was detected at DA 06. The corresponding values for Cd ranged between 0−1354 mg/kg and are detected at the mining sites only.

It must be noted here that the values of Pb in the mine and processing sites in two studies are comparable, except for the high value of 26,088 detected at DA 06. Also, the values for Cu in the mine sites in the two studies are not far apart, but the values for the processing site in our study are significantly lower than those reported in 2014 [26]. The values for Cd for some mine sites in our study are significantly higher, while those for Cu are lower than the values reported in 2014 [26]. However, no GPS values were provided in the study carried out in 2014 [26].

Plants/food analysis

Concentrations of metals in the samples of plants and food presented in Table II show that concentrations of Pb in the cereals; guinea corn, maize and millet seeds from Abare were in the range of 5.70−24.56 mg/kg. The value for beans was 10.64 mg/kg, while the value for the elephant grass was 24.63 mg/kg. In Dareta, the values of Pb in guinea corn and millet seeds were 79.91 and 22.29 mg/kg, while the corresponding values found in guinea corn and millet leaves were 36.86 and 22.76 mg/kg, respectively. The concentrations of Cu in the cereals in Abare were in the range of 11.17−14.84 mg/kg, while the corresponding value for beans was 30.41 mg/kg and the value for elephant grass was 27.37 mg/kg. In Dareta, the values of copper in guinea corn and millet seeds were 41.21 mg/kg and 11.53 mg/kg, respectively, while the levels of Cu in guinea corn leaves and millet leaves were 19.05 and 40.58 mg/kg respectively. Cadmium was not detected in guinea corn, millet, beans and elephant grass in Abare, but the maize from Abare was found to contain 5.74 mg/kg of Cd. In Dareta, Cd was not detected in the cereals, but the level found in millet leaves was 5.34 mg/kg.

Guinea corn, maize and millet are the main food in this sub region, and therefore the concentrations of heavy metals in the food samples grown in the contaminated soils are pertinent to health. It is shown in Table II that the levels of Pb in guinea corn and millet seeds in Abare were 15.60 and 7.50 mg/kg, respectively, while the corresponding values for these samples in Dareta were 79.91 mg/kg and 22.29 mg/kg, respectively. The values for Dareta samples were understandably higher than the values for Abare samples because the tonnage of gold ore processed in Dareta is much higher than that of Abare. The permissible limit of Pb in cereals is 0.1 mg/kg [27]. This value is highly exceeded by factors in the range 156−799 for guinea corn seeds and 57−223 for millet seeds. The level of Pb in the maize sample from Abare exceeds the permissible level by a factor of 245. The corresponding factor in beans is 106. Thus, all the cereals in Abare and Dareta are not good for human consumption because of the high level of Pb. Elephant grass, guinea corn leaves and millet leaves that are consumed by cattle also showed very high levels of Pb. Thus, Pb can enter the food chain and will be transferred to humans who consume meat from such cattle. The permissible limit for Cu in cereals is 2 mg/kg [27]. The value for millet seeds was 14.84 mg/kg and 11.17 mg/kg in guinea corn seeds in Abare while in Dareta, the value for millet seeds was 11.53 mg/kg and that for guinea corn seeds was 41.21 mg/kg. The values for millet seeds in Abare and Dareta were comparable but the value for guinea corn seeds in Dareta of 41.21 mg/kg, is more than double the values for guinea corn and millet seeds in Abare and the millet seeds in Dareta. The value of 30.41 mg/kg for beans obtained in Dareta was also much higher than those for the other food items except for guinea corn seeds. The values for the elephant grass in Abare and the guinea corn and millet leaves from Dareta also exceeded the permissible level by factors ranging from 10−20, if the permissible value of 2 mg/kg for cereal is adopted. Cadmium was detected in the maize from Abare and millet leaves in Dareta, and both values exceeded the permissible limit of 0.1 mg/kg for Cd by a factor of about 50.

According to data in Table 2, it seems that all the plant samples were polluted by Pb and Cu, while maize in Abare and millet leaves in Dareta were found to contain Cd as a third contaminant. The samples that were collected from the field, namely elephant grass, guinea corn leaves and millet leaves had Pb values in the range 22.76−36.86 mg/kg, while the food items purchased from homes with the exception of guinea corn from Dareta had Pb values in the range 5.70−24.56 mg/kg. The plants obtained from the fields would be contaminated by dusts from ore-processing. It should also be borne in mind that items kept in the residences could also be contaminated by dusts from ore-

processing activities in the residential areas. This is probably responsible for the value of 79.91 mg/kg for Pb and 41.21 mg/kg for Cu in guinea corn seeds obtained from Dareta.

The possible sources of heavy metal contamination of the food samples are: direct contact with the ores, uptake from polluted soils, uptake from metal-polluted air, deposition on the surface of plants and exposed food items and contact with polluted water used for irrigation. All these are potential sources of contamination in Abare and Dareta. However, irrigation was not observed in Dareta. Crops and vegetables grown in soils contaminated with heavy metals have been reported to accumulate higher levels of heavy metals than those grown in uncontaminated soils [28,29].

The consumption of the contaminated cereals, millet, guinea corn and maize seeds as well as beans by the inhabitants of Dareta and Abare will pose a risk to human health. The elephant grass obtained from Dareta with mean Pb concentration of 24.63 mg/kg is also unsafe for the livestock.

In a study carried out on the human health risk characterization of lead pollution in plants harvested from contaminated farmlands of Abare village, Pb concentration of sorghum exceeded the FAO/WHO limit by a factor of 3500 [21]. The time of sampling, however, was not stated.

One of the most widely studied mechanisms of action of toxic metals is oxidative damage due to direct generation of free radical species and depletion of antioxidant reserves [30]. Mercury, cadmium and lead can effectively inhibit glutathione peroxidase thereby reducing the effectiveness of this antioxidant defense system for detoxification [31]. Some heavy metals act as molecular mimics of nutritionally essential trace elements and compete with metallic cofactors for entry into cells and incorporation into enzymes [32]. Cadmium can compete with and displace zinc from proteins while lead and thallium are chemically similar to calcium and potassium [32-34].

Lead toxicity in human adults can lead to poor muscle coordination, nerve damage to the sense organs and nerves controlling the body, increased blood pressure, hearing and vision impairment and decreased sperm count. In children it can lead to damage to the brain, nervous system, liver, kidney and death [35]. Children less than seven years old are largely at risk [16].

The health implication of the results presented in this study is the possible occurrence of Pb, Cu and Cd poisoning in all the people exposed to the ores. Ores are processed in residential areas by women and older children. Children including infants sometimes put unwashed hands in their mouths thus ingesting the ore dust. They also inhale the dust during processing of the ore. They have less tolerance to heavy metal toxicity and hence high mortality of exposed children is inevitable. The women are equally exposed and mortality though not as high as in children, would be expected. All the inhabitants ingest the contaminated foods and thus would be victims of heavy metal toxicity, namely lead and cadmium. Lead toxicity is implicated in abdominal pain, confusion, anemia, seizures, coma and deaths [36] while cadmium toxicity is implicated in lung cancer, kidney and bone damage [37].

All reports on high mortality in Zamfara State have attributed the deaths to the Pb poisoning [38]. The electrochemical method used in this study has made it possible to establish the presence of other heavy metal pollutants, namely copper and cadmium which may also be implicated in the high mortality.

Conclusions

Linear sweep anodic stripping voltammetry has been found very useful in the identification and determination of heavy metal pollutants, copper, cadmium and lead in the soil and plants/food samples. Presence of very high concentrations of these metals in the samples from several parts of Abare and Dareta regions reported in this study is related to the mining of ores at these locations

and may be implicated in the high mortality in Zamfara State. It is obvious that to address this health risk, safe mining practices should be enforced and soil remediation of all these areas should be carried out. Educating the people, especially children, on toxicity of heavy metals and monitoring of these toxic metals in their blood should also be carried out periodically.

References

[1] MedecinsSansFrontieres. MSF Briefing Paper, (2012) http://www.msf.org/en/article/lead-poisoning-crisis-zamfara-state-northern-nigeria (Accessed on 8th October, 2017).
[2] W. O. Okiei, M. Ogunlesi, A. Adio, M. Oluboyo, *International Journal of Electrochemical Science* **11** (2016) 8280-8294.
[3] S. Khan, Q. Cao, Y. M. Zheng, Y. Z. Huang, Y.G. Zhu, *Environmental Pollution* **152** (2008) 686-692.
[4] E. D. Doe, A. K. Awua, O. K. Gyamfi, N. O. Bentil, *American Journal of Applied Chemistry* **1** (2013) 17-21.
[5] W. J. O. Oti, International Journal of Environmental Science and Toxicology Research **3 (2)** (2015) 16-21.
[6] S. O. Salihu, J.O . Jacob, M. T. Kolo, *Pakistan Journal of Nutrition* **13** (2014) 722-727.
[7] W.A. Tegegne, Ethiopia Journal of Cereals and Oilseeds **6** (2015) 8-13.
[8] E. J. Martinez-Finley, S. Chakraborty, S. Fretham, M. Aschner, *Metallomics* **4** (2012) 593-605.
[9] A. T. Jan, M. Azam, K. Siddiqui, A. Ali, I. Choi, Q. M. R. Haq, *International Journal of Molecular Sciences* **16** (2015) 29592-29630.
[10] D. A. Cataldo, R. E. Wildung, *Environmental Health Perspectives* **27** (1978) 149-159.
[11] M. C. Jung, *Sensors* **8** (2008) 2413-2423.
[12] B. V. Tangahu, S. R. S. Abdullah, H. Basri, M. Idris,N. Anuar, M. Mukhlisin, *International Journal of Chemical Engineering* **2011** (2011) 1-31.
[13] M. A. Adegboye, *Journal of Science and Environmental Management* **3** (2013) 77-83.
[14] Z. Y. Hseu, *Bioresource Technology* **95** (2014) 53-59.
[15] P. Chooto, P. Wararatananurak, C. Innuphat, *ScienceAsia* **36** (2010) 150-156.
[16] US EPA. United States Environmental Protection Agency. 40 CFR Part 745 [OPPTS-62156H; FRL-6763-5] RIN 2070-AC63. Lead; identification of dangerous Levels of Lead: Final Rule, 2001
[17] US EPA. Supplemental guidance for developing soil screening levels for superfund sites. Office of Solid Waste and Emergency Response, Washington, D.C. (2002) http://www.epa.gov/superfund/health/conmedia/soil/index.htm (Accessed on 8th October, 2017).
[18] WHO. Permissible limits of heavy metals in soil and plants, (Genava: World Health Organization), Switzerland (1996).
[19] UNEP/OCHA, Joint UNEP/OCHA Environment Unit. Lead Pollution and Poisoning Crisis Environmental Emergency Response Mission Zamfara State, Nigeria (2010).
[20] K. D. Tsuwang, I. O. Ajigo, U. A. Lar, International Journal of Science and Environmental Technology **3** (2014) 187-197.
[21] A. Abdul, A. A. Yusuf, African Journal of Environmental Science and Technology **7** (2013) 911-916.
[22] Blacksmith Institute. UNICEF Programme. Environmental Remediation – Lead Poisoning in Zamfara State FINAL REPORT, September 2010-March 2011.
[23] CDC. Centre for Disease Control and Prevention. New lead information. National Center for Environmental Health. Division of Emergency and Environmental Health Services, 2017.
[24] ATSDR, Agency for Toxic Substances and Disease Registry. Toxicological profile for copper. U.S. Department of Health and Human Services Public Health Service, 2004. http://www.atsdr.cdc.gov/toxprofiles/tp132.pdf (Accessed on 8th October, 2017).
[25] N. Johri, G. Jacquillet, R. Unwin, *Biometals* **23** (2010) 783-792.
[26] L. Uriah, C. T. Ngozi-Chika, K. Tsuwang, *American Journal of Environmental Protection* **3(6-2)** (2014) 14-18.
[27] FAO/WHO. Joint FAO/WHO Food Standards Programme. Codex Alimentarius Commission.Report of the fifth Session of the Codex Committee on Contaminants in Foods.Thirty-fourth Session, Geneva, Switzerland, 2011, www. ftp://ftp.fao.org/codex/meetings/CCCF/cccf5/cf05_INF.pdf (Accessed on 8th October, 2017).

[28] G. Guttormsen, B. R. Singh, A. S. Jeng, *Fertilizer Research* **41** (1995) 27-32.
[29] C. K. Bempah, A. B. Kwofie, A. O. Tutu, D. Denutsui, N. Bentil, *Elixir International Journal* **39** (2011) 4921-4926.
[30] N. Ercal, H. Gurer-Orhan, N. Aykin-Burns, *Current Topics in Medicinal Chemistry* **1** (2001) 529-539.
[31] C. C. Reddy, R. W. Scholz, E. J.Massaro, *Toxicology and Applied Pharmacology* **61** (1981) 460-468.
[32] D. H. Jang, R.S. Hoffman, *Neurologic Clinics* **29** (2011) 607-622.
[33] G. W. Buchko, N. J. Hess, M. A. Kennedy, *Carcinogenesis* **21** (2000) 1051-1057.
[34] F. Thevenod, W.K. Lee, *Metal Ions in Life Sciences* **11** (2013) 415-490.
[35] ATSDR, Agency for Toxic Substances and Disease Registry. Toxicological profile for lead. Division of Toxicology and Environmental Medicine, Atlanta, GA, 2007. http://www.atsdr.cdc.gov/toxprofiles/tp13-p.pdf (Accessed on 8th October, 2017).
[36] ATSDR. Agency for Toxic Substances and Disease Registry. Case studies in environmental medicine (CSEM). Lead toxicity. Course WB 1105. Atlanta GA, 2010.
[37] ATSDR. Agency for Toxic Substances and Disease Registry. Toxicological profile for cadmium, US Department of Health and Human Services, Atlanta, GA. 2012, pp 1-487.
[38] WHO. World health Organization. Nigeria: Mass lead poisoning from mining activities, Zamfara State, 2010. http://www.who.int/csr/don/2010_07_07/en/ (Accessed on 8th October, 2017).

J. Electrochem. Sci. Eng. **7(4)** (2017) 181-191; DOI: http://dx.doi.org/10.5599/jese.422

Open Access : : ISSN 1847-9286

www.jESE-online.org

Original scientific paper

Carbon nanofiber modified with osmium based redox polymer for glucose sensing

Amos Mugweru[1,✉], Reaz Mahmud[2], Kartik Ghosh[2], Adam K. Wanekaya[3]

[1]*Department of Chemistry and Biochemistry, Rowan University, Glassboro, NJ 08028, USA*
[2]*Physics Astronomy and Materials Science Department, Missouri State University, Springfield, Missouri 65897, USA*
[3]*Chemistry Department, Missouri State University, Springfield, Missouri 65897, USA*

Corresponding authors E-mail: ✉mugweru@rowan.edu, Tel.: +1-856-2565454; Fax: +1-856-256-4478

Received: August 22, 2017; Revised: October 26, 2017; Accepted: November 12, 2017

Abstract

Electrochemical detection of glucose was performed on carbon nanofibers containing an osmium based redox polymer and using glucose oxidase enzyme. Redox polymer assembled on the nanofibers provided a more stable support that preserved enzyme activity and promoted the electrical communication to the glassy carbon electrode. The morphologies, structures, and electrochemical behavior of the redox polymer modified nanofibers were characterized by scanning electron microscope, energy dispersive spectrometer and voltammetry. The glucose oxidase showed excellent communication with redox polymer as observed with the increased activity toward glucose. Both cyclic voltammetry and amperometry showed a linear response with glucose concentration. The linear range for glucose determination was from 1 to 12 mM with a relatively high sensitivity of 0.20±0.01 μA mM^{-1} for glucose oxidase in carbon nanofibers and 0.10±0.01 μA mM^{-1} without carbon nanofibers. The apparent Michaelis–Menten constant (K_m) for glucose oxidase with carbon nanofibers was 0.99 mM. On the other hand, the K_m value for the glucose oxidase without the nanofibers was 4.90 mM.

Keywords

Cyclic voltammetry; Amperometry; Michaelis-Menten kinetics; Glucose sensors

Introduction

Regular monitoring of glucose concentration in the blood is a key in the diagnosis as well as treatment of diabetes. There is continuous interest in low cost, stable and sensitive biosensors for glucose. Many glucose sensing platforms have been developed using glucose oxidase enzyme and various forms of redox mediators on electrodes [1-4]. Glucose oxidase (GOX) is the most popular enzyme extensively used in fabrication of electrochemical glucose biosensor [5] as well as in other

bio-catalytic systems [6,7]. Previously, osmium based redox polymer was used as a mediator entrapped together with GOX hydrogels through the UV-initiated free radical cross-linking [1,2].

The advantage of using electrochemical methods with glucose oxidase enzyme in glucose sensors is the fact that the enzyme is very selective to glucose. Like all enzymes, glucose oxidase stability is affected by the environment conditions such as pH and temperature [8]. Incorporating conducting nanomaterials as a transducer material provides fast and accurate electron transfer at electrode surface. The combination of nanomaterials and conducting polymers has attracted remarkable attention for development of new immobilization matrices for enzymes.

Many glucose sensors are incorporating carbon nanotubes for immobilization of different electron transfer mediators [9,10]. Carbon nanomaterials have excellent properties and unique structure for use in the study of direct electrochemistry of enzymes [11,12]. Enzyme immobilization techniques are the key in improving its performance. Recently, nanofibers have shown to be ideal in immobilization of enzymes [13,14]. Carbon nanofibers made from nylon have been used for bio-sensing applications due to their excellent stability and biocompatibility [15,16]. Nylon nanofibers have porous structure and have large surface area [17]. In general, the nanofibers are good materials for enzyme immobilization due to high loading resulted from high interfacial adhesion. Direct electron transfer (DET) between glucose oxidase enzyme and electrode surface would be ideal in glucose sensor. Then, the electron transfer process is quite sluggish [18] and hence use of mediators is initiated. Inclusion of mediators and carbon-based nanomaterials can greatly improve the electro-catalytic performance of these sensors. Enzymes, including GOX may denature upon absorption on the nanostructured surface. Denaturation of the enzyme may result in decreased or total loss of function as a result of altered structure [19]. Hybrid materials comprising of carbon nanofibers and redox polymer can induce a synergic effect of protecting the enzyme from the nanostructured surface, as well as providing a stable surface for immobilization onto a carbon surface. This can facilitate charge transfer from GOX to redox polymer, as well as increase of conductivity of the composite polymeric film. Nanofibers are promising nanomaterials as enzyme immobilization matrices [20].

In this work, poly[vinylpyridine Os(bipyridine)$_2$]Cl (referred here as redox polymer) coupled with carbon nanofibers were used as materials in which GOX was immobilized. New literature suggests that this redox polymer can also mediate electron transfer between cells and electrodes [21]. The osmium based redox polymer has well-established redox chemistry and has been used before in different matrices [22-24]. The Os(II)/(III) redox potential is lowered when the osmium is complexed with ligands. We have previously used osmium redox polymers in construction of different biosensors [25,26]. The new material containing carbon nanofibers and osmium based redox polymers were used to fabricate a stable glucose sensor.

Experimental

Materials and reagents

Glucose oxidase (GOX, EC 1.1.3.4, Type X-S, 128 units/mg, solid from Aspergillus niger), hexafluorophosphate, sodium dithionite, ether, N,N-Dimethyl formamide, hydrochloric acid, ethyl alcohol, ethylene glycol, and acetonitrile were purchased from VWR (West Chester, PA). Pyrolytic graphite electrodes (area 0.07 cm^2) were obtained from momentive performance materials Quarts Inc. The polishing alumina and 1 µm diamond polish were obtained from Bioanalytical Systems Inc (West Lafayette IN). Graphitized carbon nanofibers free from iron, poly(4-vinyl pyridine) and poly(ethylene glycol) di-acrylate (MW 575), were purchased from Sigma-Aldrich, while hexa-fluoro-

phosphate, sodium dithionite, ether, N,N-Dimethyl formamide, ammonium hexa-chloroosmate (IV) and 2-bromoethylamine hydro-bromide, were from Alfa Aesar.

Synthesis of redox polymer poly[vinylpyridine Os(bipyridine)$_2$]Cl

The poly-cationic redox polymer, poly[4-vinylpyridine Os(bipyridine)$_2$]Cl (noted as Poly-BiPy-OsCl) was synthesized according to a procedure described previously [27-29]. Os(bpy)$_2$Cl$_2$ was synthesized according to a standard procedure with minor modifications [30]. Briefly, bipyridine (1.44 g) and ammonium hexa-chloroosmate (IV) (2.0 g) were mixed in 100 mL ethylene glycol before refluxing for one hour. Addition of a supersaturated solution of sodium dithionate to the reaction mixture precipitated Os(bpy)$_2$Cl$_2$. The product was repeatedly washed with water and finally with ether.

In synthesis of poly[vinylpyridine Os(bipyridine)$_2$]Cl, Os(bpy)$_2$Cl$_2$ (0.988 g) and poly(4-vinyl-pyridine) (0.860 g) were mixed and then heated to reflux under a nitrogen atmosphere to prevent oxidation. After two hours of reflux, the solution was cooled down to room temperature. 60 mL of DMF and 3.0 g of 2-bromoethylamine hydro-bromide were added and then stirred overnight at 50 °C. A crude polymer precipitate was formed by pouring the solution into rapidly stirred acetone. The soluble portion of the synthesized redox polymer was used in this work. The structure of this polymer is shown in Figure 1.

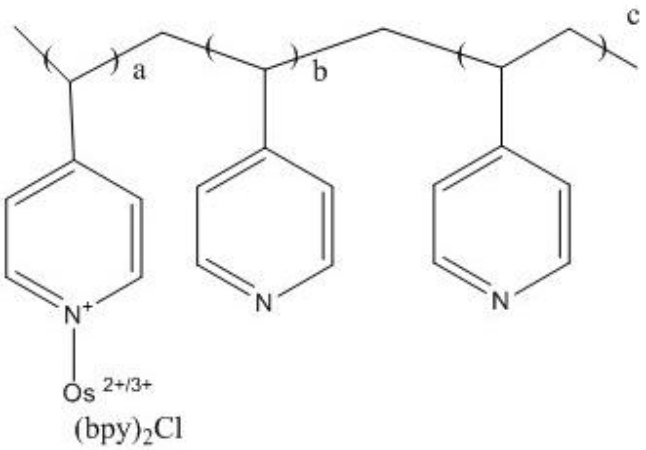

Figure 1. *Structure of poly[vinylpyridine Os(bipyridine)$_2$]Cl redox polymer, (Poly-BiPy-OsCl) (a = 1, b = 4, c = 1) are based on initial reaction conditions*

Electrochemical apparatus and preparation procedure

Cyclic voltammetry (CV) and amperometric techniques were carried out with a computer controlled electrochemical workstation (CHI 660c, USA) with 98 % ohmic drop (IR) compensation. A three-electrode electrochemical cell was used for all electrochemical experiments. The working and the counter electrodes were obtained from Bioanalytical Systems Inc (West Lafayette, IN). Glassy carbon electrodes (0.07 cm^2) were polished with 1 µm diamond polishing paste then ultra-sonicated in ethanol and distilled water successively for 1 min followed by rinsing in water.

A pyrolytic graphite (PG) electrode functionalized with composite materials of carbon nanofibers, osmium based redox polymer and glucose oxidase was used as the working electrode. Platinum wire was used as the counter electrode. Ag/AgCl, equipped with a glass tip, separated from the sample solution compartment by a salt-bridge containing KCl and terminating in a medium porosity glass frit, was used as the reference electrode. All electrochemical measurements were carried out at ambient conditions. The concentration of acetate buffers were 50 mM. A precursor solution 2 mL

of 10 mg/mL redox polymer and 0.5 mL of 50 mg/mL GOX was made using the acetate buffer. This precursor solution was mixed with 0.5 g of carbon nanofibers (CNF) and then diluted to 10 ml with acetate buffer. After mixing well, 10 µL of this composite mixture was casted as dispersion on the electrode and left to dry at room temperature. Using the electrode area of 0.07 cm^2, we can estimate the polymer loading to be 0.3 mg/cm^2, glucose oxidase was 0.36 mg/cm^2 while the CNF loading was 7.1 mg/cm^2. The electrode containing redox polymer, CNF and GOX was later rinsed with water before use. The pictorial representation of the electrode preparation is shown in Figure 2.

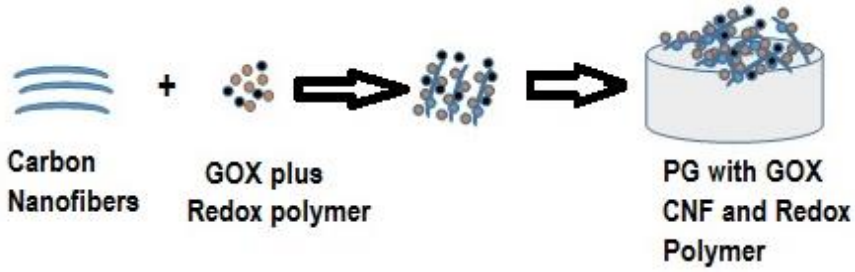

Figure 2. *Schematic illustration of the preparation of electrode containing carbon nanofiber-redox polymer-glucose oxidase, PG-CNF-(Poly-BiPy-OsCl)-GOX*

Results and discussion

Scanning electron microscopy and Energy-dispersive X-ray spectroscopy

The scanning electron microscope images were recorded using a FEI Quanta 200 Scanning Electron Microscope with an Oxford Inca EDS detector. Figure 3 shows SEM images of redox polymer with GOX on CNF at different regions and different magnification.

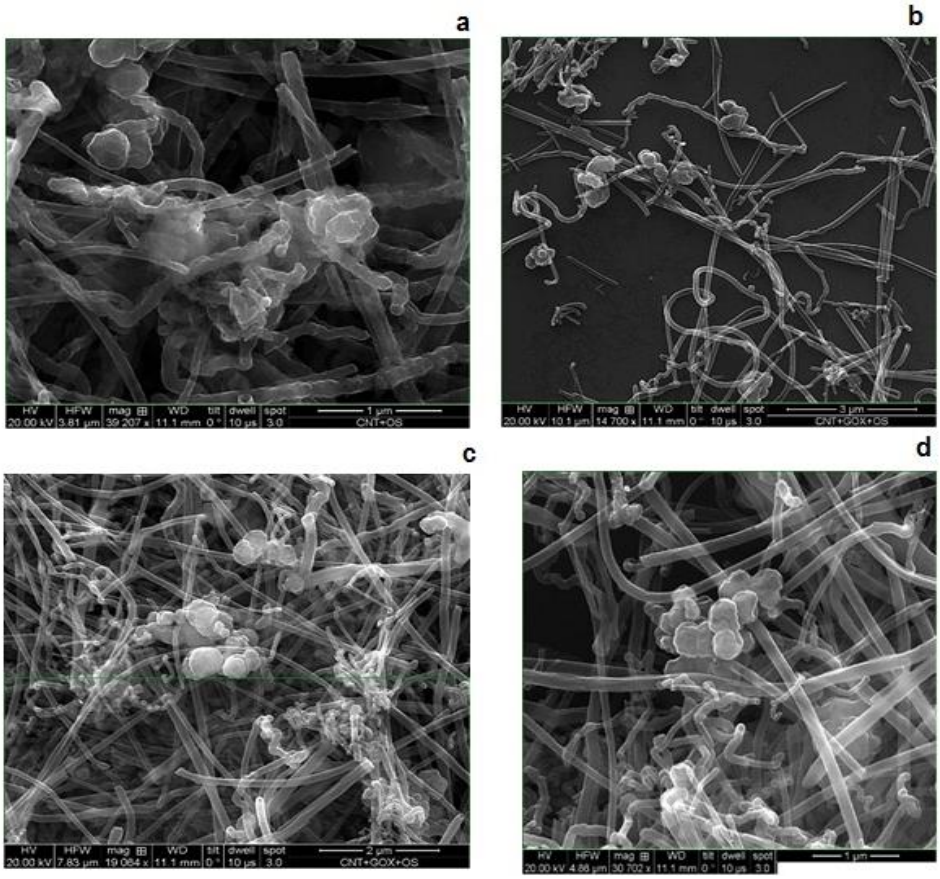

Figure 3. *SEM images at different magnification of carbon nanofibers with redox polymer and glucose oxidase*

The graphitized conical CNF were used as the anchor for both, the redox polymer and the GOX. From Figure 3 we can estimate the length of the longest nanofiber to about 5 µm. Figure 3a shows the CNF functionalized with the redox polymer. The redox polymer is not uniformly distributed on the CNF, but it is making some CNF to be bound closer together. Immobilization of the redox polymer on CNF results in formation of globular particles around the nanofibers (Figure 3a). Figures 3b-d show images at various magnifications of CNF with both, the redox polymer and the GOX. It is obvious from these images, that the carbon nanofibers integrity was not affected. GOX adhered well onto carbon nanofibers after immobilization. However, the adherence of GOX to the nanofiber surface was not well-organized.

Figure 4 shows the energy-dispersive X-ray spectroscopy (EDX) of composite materials of CNF and the osmium based redox polymer. The presence of the osmium signal indicates that the polymer was incorporated into the composite material.

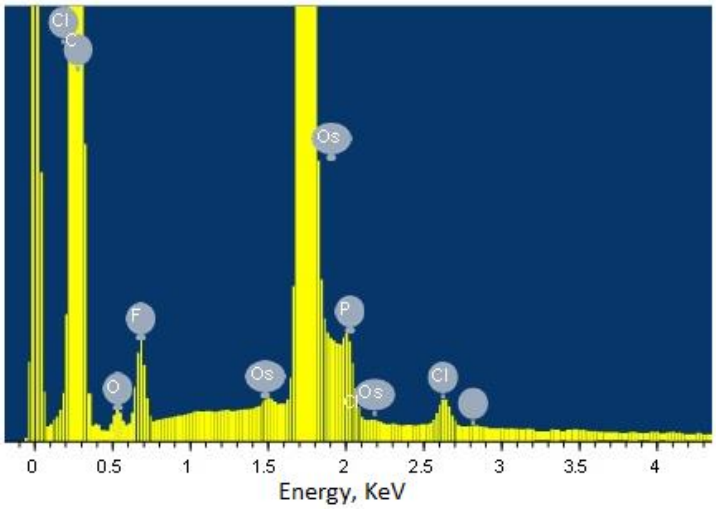

Figure 4. *EDX spectrum of the redox polymer carbon nanofiber composite directly casted on the glassy carbon*

Cyclic voltammetry

Figure 5 shows cyclic voltammograms of the redox polymer casted on a glassy carbon electrode with and without CNF. Reversible pairs of oxidation-reduction peaks correspond to the Os(II)/Os(III) redox couple.

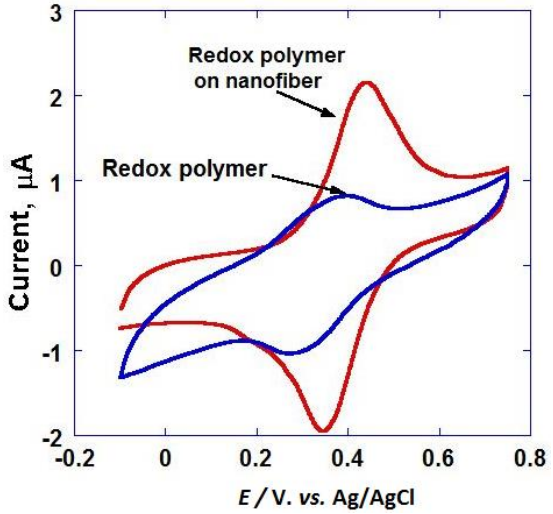

Figure 5*. Cyclic voltammograms of redox polymer on glassy carbon electrode recorded at 50 mV/s scan rate in 50 mM acetate buffer, pH 5.5: (blue) (Poly-BiPy-OsCl); (red) CNF-(Poly-BiPy-OsCl)*

The redox polymer on CNF shows an enhanced signal compared with polymer electrode, what is seen as peak amplitudes that are about three times greater than those of the redox polymer by itself. However, incorporation of the redox polymer in the CNF resulted in a 0.05 V positive potential shift of the redox peak. The oxidation peak for redox polymer recorded at 50 mV/s scan rate occurred at about 0.44 V, while the reduction peak occurred at 0.34 V using the CNF.

The oxidation peak for polymer by itself on the electrode surface appeared at 0.39 V while the reduction peak appeared at about 0.29 V. In earlier literature, the redox polymer trapped in polyethylene glycol gel still gave similar voltammograms but the peak current was unstable after continuous scanning [31,32]. For the redox polymer modified nanofibers, scanning several times over three weeks yielded the same peak current, indicating thus a good stability of redox polymer adsorbed on CNF.

In presence of glucose the current using PG-CNF-(Poly-BiPy-OsCl)-GOX was found to increase (Figure 6). Presence of glucose caused the current increase. Flavin adenine dinucleotide of glucose oxidase GOX(FAD) reacts with β-D-glucose to form a reduced form GOX($FADH_2$) and gluconic acid and hydrogen peroxide. The reduced form of GOX ($FADH_2$) is in turn oxidized by the electrochemically generated Os^{3+} form of the redox polymer, setting up a catalytic pathway which produces an enhanced oxidation peak. The electrons are transferred from the enzyme to the redox polymer, shuttled between the redox sites in self exchange reaction until being transferred to an electrode surface. The catalytic current produced is proportional to the glucose concentration.

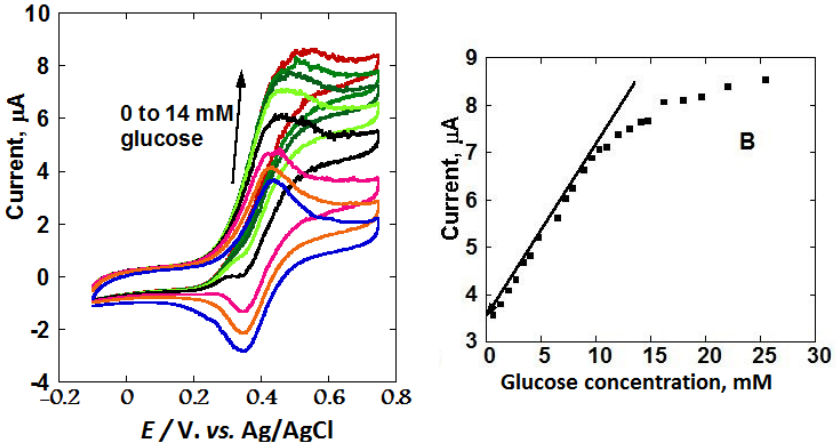

Figure 6. *(a) Cyclic voltammograms of PG-CNF-(Poly-BiPy-OsCl)-GOX in 50 mM acetate buffer, pH 5.5, recorded at 50 mV s^{-1} scan rate after continuous addition of glucose; (b) calibration curve for glucose*

Figure 6a shows the cyclic voltammograms of PG-CNF-(Poly-BiPy-OsCl)-GOX system recorded after continuous addition of glucose. The resultant voltammogram in presence of glucose shows a significant increase in the magnitude of the oxidation peak. Figure 6b shows the observed peak current values plotted against concentration. The glucose concentration shows a linear relationship with the peak current up to about 12 mM of glucose. A plot of increase in the peak current versus the concentration of glucose yielded linear plot (y = 3.4 + 0.35x, R=0.996, n=10) with 0.20 ± 0.01 µA mM^{-1} sensitivity. Glucose concentration higher than 12 mM did not yield a current in the linear region. The linear response obtained in the range of 1 to 12 mM is an improvement related to 0.05–100 µM reported recently for comparable systems [33-35]. In the present system, presence of oxygen did not influence the rate of the reaction and hence the catalytic current is obtained. There was no difference in results obtained when oxygen was removed by bubbling the solution with nitrogen and blanketing the solution with nitrogen.

PG-CNF-(Poly-BiPy-OsCl)-GOX and PG-(Poly-BiPy-OsCl)-GOX systems were also compared using the cyclic voltammetry results. The oxidation peak currents of both systems were recorded with increased amount of glucose in the reaction cell. The catalytic currents obtained for both systems at different glucose concentrations are compared in Figure 7. It is clear that presence of CNF in the system amplifies the catalytic current obtained using cyclic voltammetry.

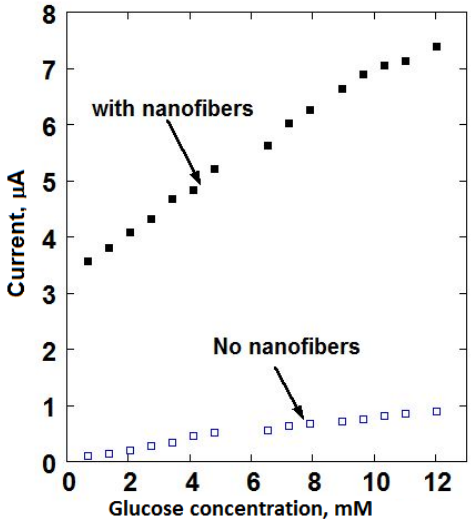

Figure 7. *Comparison of glucose calibration curves for the electrode with nanofibers, PG-CNF-(Poly-BiPy-OsCl)-GOX and without nanofibers, PG-(Poly-BiPy-OsCl)-GOX*

Amperometry

Figure 8a shows amperometric responses of both, PG-CNF-(Poly-BiPy-OsCl)-GOX and PG-(Poly-BiPy-OsCl)-GOX electrodes. Each electrode was held at 0.35 V *vs*. Ag/AgCl and the current was continuously monitored as a function of time. For both systems, the amperometric responses showed a clear stepwise increase in the current value upon addition of glucose. However, the amperogram using PG-CNF-(Poly-BiPy-OsCl)-GOX shows a much higher current increase than PG-(Poly-BiPy-OsCl)-GOX using the same amount of glucose.

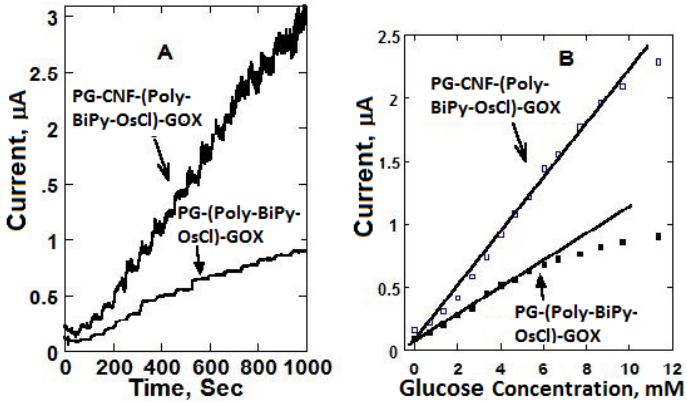

Figure 8*. (a) Current versus time curve of PG-CNF-(Poly-BiPy-OsCl)-GOX and PG-(Poly-BiPy-OsCl)-GOX in 50 mM acetate buffer, pH 5.5, at 0.35 V vs. Ag/AgCl after continuous addition of glucose (b) Comparison of current versus glucose concentration for PG-(Poly-BiPy-OsCl)-GOX and PG-CNF-(Poly-BiPy-OsCl)-GOX sensors.*

This could probably be due to a three-dimensional structure formed by anchoring the GOX on CNF. This three-dimensional structure coupled with the large surface area of CNF resulted in the high sensitivity observed. Glucose oxidase is comprised of two identical subunits. The two units have

two moles of flavin adenine dinucleotide (FAD) which are located deep inside the enzyme [36]. For our sensor to provide immediate response, analytes have to move into the GOX and electrons have to move into the redox polymer. The rapid response observed imply that this movement is not hindered at the same time as the CNF containing the redox polymer must remain in place. Each step current observed represents an increase of 0.70 mM of glucose concentration. A plot of change of current versus the glucose concentration also yielded a linear plot (Figure 8b). Higher sensitivity of PG-CNF-(Poly-BiPy-OsCl)-GOX sensor compared to PG-(Poly-BiPy-OsCl)-GOX was observed.

The sensitivity of electrodes with carbon nanofibers was 0.21 ± 0.01 μA mM^{-1}, while the sensitivity of electrodes without the carbon nanofibers was 0.10 ± 0.01 μA mM^{-1}. The use of CNF improves the sensitivity of this sensor by around fifty percent. The sensitivity of the current sensor is much lower compared with others recently reported [37,38]. For the system with CNF, the peak current plateaued at about 12 mM glucose concentration, while without CNF, the peak current plateaued at about 6 mM.

Glucose oxidase is known to have a short operational life due to the lack of stability. This is a major drawback in the construction of glucose biosensors [39]. To compare the enzymatic glucose metabolism in PG-CNF-(Poly-BiPy-OsCl)-GOX and PG-(Poly-BiPy-OsCl)-GOX systems, the Michaelis–Menten kinetics were determined and compared. Based on the equations (1) and (2) and using the plots drawn in Figure 9, I_{max} and Michaelis-Menten constant (K_m) values for the GOX were calculated for both systems.

$$I_{ss} = \frac{I_{max} c_{glucose}}{K_m + c_{glucose}} \quad (1)$$

$$\frac{1}{I_{ss}} = \frac{1}{I_{max}} + \frac{K_m}{I_{max}} \frac{1}{c_{glucose}} \quad (2)$$

In equations (1) and (2), I_{max} represents the maximum current achieved in the system, while the I_{ss} is the steady state current.

Figure 9 shows the Lineweaver-Burk plots of PG-CNF-(Poly-BiPy-OsCl)-GOX and PG-(Poly-BiPy-OsCl)-GOX, respectively. The apparent K_m values with respect to glucose were estimated using the eq. (2) and plots in Figure 9.

These enzymatic kinetics studies showed that PG-CNF-(Poly-BiPy-OsCl)-GOX system had a K_m of 0.99 mM, while the calculated K_m value for PG-(Poly-BiPy-OsCl)-GOX was 4.90 mM. It is obvious that glucose oxidase enzyme catalytic property of PG-CNF-(Poly-BiPy-OsCl)-GOX is much higher than of PG-(Poly-BiPy-OsCl)-GOX enzymes. Mass transfer limitations of glucose is the same in both electrodes and the only explanation for higher activity at CNF could be due to a loss of glucose oxidase activity in PG-(Poly-BiPy-OsCl)-GOX electrode. This might be due to the conformation change of the enzyme in this system. For most enzymes a favorable environment is essential for the optimum enzyme activity. Our results indicate an extraordinary stability of the PG-CNF-(Poly-BiPy-OsCl)-GOX system as compared to PG-(Poly-BiPy-OsCl)-GOX.

The recent literature showed that K_m for glucose oxidase immobilized at other materials is equal to 2.84 mM [40]. Here obtained value of the Michaelis-Menten constant of 0.99 mM is much lower than 5.20 mM for GOX/gold-platinum alloy nanoparticles/carbon nanotubes/chitosan system [41] and also 1.42 mM for GOX/PVA-Fe_3O_4/Sn [42]. Our experiment was performed in the acetate buffer of pH 5.5 which is slightly different from the optimum pH for GOX activity. However, this pH is optimum for redox polymer mediator.

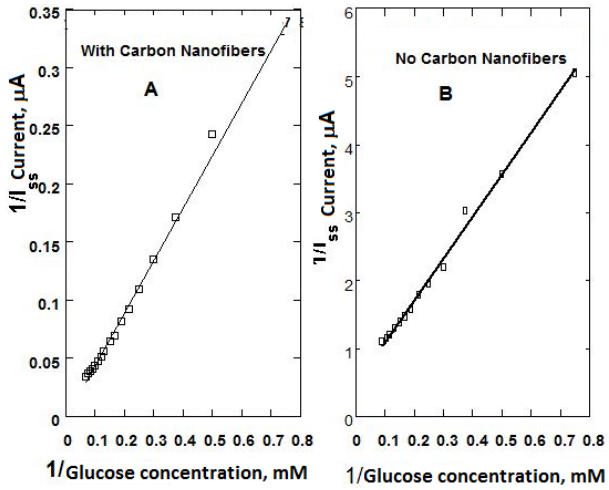

Figure 9. *Lineweaver-Burk plots for glucose oxidase (a) PG-CNF-(Poly-BiPy-OsCl)-GOX; (b) PG-(Poly-BiPy-OsCl)-GOX*

The ability of a sensor to discriminate other interfering species with similar properties to the target analyte is very important. Oxidative species such as uric acid, fructose, sodium chloride and sucrose among others co-exist with glucose in human blood. The interference study was carried using amperometry by spiking 1.4 mM of each of the interfering agent in the electrolyte. The resulting amperogram for PG-CNF-(Poly-BiPy-OsCl)-GOX is shown in Figure 10.

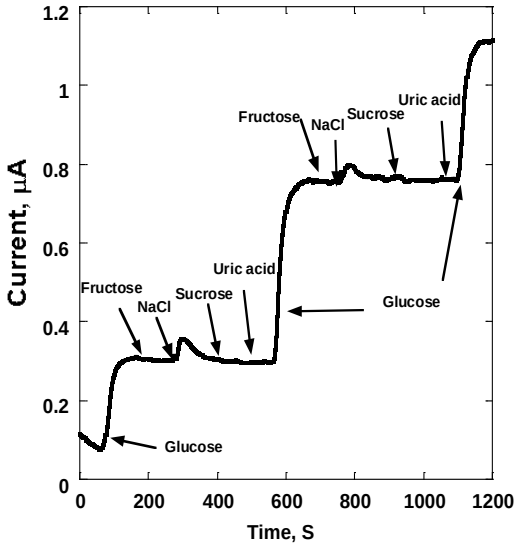

Figure 10*. Current versus time curve of PG-CNF-(Poly-BiPy-OsCl)-GOX in 50 mM acetate buffer, pH 5.5 at 0.35 V vs. Ag/AgCl after continuous addition of glucose, fructose, sodium chloride sucrose and uric acid*

The peak current obtained from glucose solution and interfering ions was noted and it proves that glucose oxidation current was dominant when compared to oxidation currents of uric acid, fructose, sucrose and sodium chloride. The small rise with addition of sodium chloride suggests the electrolyte solution may not have been properly buffered. In general, the PG-CNF-(Poly-BiPy-OsCl)-GOX sensor shows high selectivity towards glucose.

Conclusions

In this work, carbon nanofibers were used in conjunction with poly[vinylpyridine Os(bipyridine)$_2$]Cl to prepare a sensor for glucose determination. Both, the glucose oxidase and the

osmium based redox polymer adhered strongly onto the carbon nanofibers as observed from SEM images. In this new system, glucose oxidase was found to be almost two fold active and more stable, using both cyclic voltammetry and amperometry techniques. The Michaelis-Menten constant (K_m) and steady state current (I_{ss}) values showed the improved GOX performance in presence of carbon nanofibers, what is partly due to enhanced electron transfer from the glucose oxidase to the redox polymer. If properly optimized, the new material could be promising in improving glucose biosensors involving glucose oxidase enzymes.

Acknowledgements: *The authors would like to thank the Zahilis Mazzochette and the department of Chemistry and Biochemistry, Rowan University.*

References

[1] A. Mugweru, B. L. Clark, M. V. Pishko, *Electroanalysis* **19** (2007) 453-458.
[2] A. Mugweru, B. L. Clark, M. V. Pishko, *Journal of Diabetes Science and Technology* **1** (2007) 366-371.
[3] A. Heller, Current Opinion in Chemical Biology **10** (2006) 664-672.
[4] P. Åsberg, O. Inganäs, *Biosensors & Bioelectronics* **19** (2003) 199-207.
[5] Y.-T. Wang, L. Yu, Z.-Q. Zhu, J. Zhang, J.-Z. Zhu, C.-H. Fan, *Sensors and Actuators B: Chemical* **136** (2009) 332-337.
[6] A. Heller, *Physical Chemistry Chemical Physics* **6** (2004) 209-216.
[7] S. Cosnier, A. Le Goff, M. Holzinger, *Electrochemistry Communications* **38** (2014) 19-23.
[8] L.M. Lu, L. Zhang, F.L. Qu, H.X. Lu, X.B. Zhang, Z.S. Wu, S.Y. Huan, Q.A. Wang, G.L. Shen, R.Q. Yu, *Biosensors and Bioelectronics* **25** (2009) 218-223.
[9] S. Xi, *Sensors and Actuators A: Physical* **198** (2013) 15-20.
[10] M. Rezaeinasab, *Electroanalysis* **29** (2017) 423-432.
[11] X. Zhang, D. Liu, L. Li, T. You, *Scientific Reports* **5** (2015) 9885.
[12] S.-G. Hong, *Biotechnology and Bioprocess Engineering* **21** (2016) 573-579.
[13] H. Liang, S. Jiang, Q. Yuan, G. Li, F. Wang, Z. Zhang and J. Liu, *Nanoscale* **8** (2016) 6071-6078.
[14] D. Liu, X. Zhang, T. You, *ACS Applied Materials & Interfaces* **6** (2014) 6275-6280.
[15] M. Scampicchio, A. Arecchi, A. Bianco, A. Bulbarello, C. Bertarelli, S. Mannino, *Electroanalysis* **22** (2010) 1056-1060.
[16] M. Yasuzawa, Y. Omura, K. Hiura, J. Li, Y. Fuchiwaki, M. Tanaka, *Analytical Sciences* **31** (2015) 1111-1114.
[17] A. Arecchi, M. Scampicchio, S. Drusch, S. Mannino, *Analytica Chimica Acta* **659** (2010) 133-136.
[18] Y. Wang, L. Liu, M. Li, S. Xu, F. Gao, *Biosensors & Bioelectronics* **30** (2011) 107-111.
[19] A. Seehuber, R. Dahint, *The Journal of Physical Chemistry B* **117** (2013) 6980-6989.
[20] S. Huang, Y. Ding, Y. Liu, L. Su, R. Filosa, Y. Lei, *Electroanalysis* **23** (2011) 1912-1920.
[21] G. Pankratova, K. Hasan, D. Leech, L. Hederstedt, L. Gorton, *Electrochemistry Communications* **75** (2017) 56-59.
[22] M. Grattieri, *ChemElectroChem*, **3** (2016) 1884-1889.
[23] Y. Nakabayashi, A. Omayu, S. Yagi, K. Nakamura, J. Motonaka, *Analytical Sciences* **17** (2001) 945-950.
[24] M. Kirthiga, *Electrochimica Acta* **230** (2017) 89-97.
[25] A. Mugweru, B. Wang, J. Rusling, *Analytical Chemistry* **76** (2004) 5557-5563.
[26] M. Amos, *Analytical Sciences* **24** (2008) 1105-1110.
[27] B. A. Gregg, A. Heller, *The Journal of Physical Chemistry* **95** (1991) 5970-5975.
[28] V. Soukharev, N. Mano, A. Heller, *Journal of the American Chemical Society* **126** (2004) 8368-8369.
[29] F. Mao, N. Mano, A. Heller, *Journal of the American Chemical Society* **125** (2003) 4951-4957.
[30] P. Denisevich, H.D. Abruna, C.R. Leidner, T.J. Meyer, R.W. Murray, *Inorganic Chemistry* **21** (1982) 2153-2161.
[31] A. Mugweru, *Electroanalysis* **19** (2007) 453-458.
[32] A. Mugweru, *Journal of Diabetes Science and Technology* **1** (2007) 366.
[33] D. Xu, *Analytical Biochemistry* **489** (2015) 38.
[34] T. Y. Tekbasoglu, T. Soganci, M. Ak, A. Koca, M. K. Sener, *Biosensors & Bioelectronics* **87** (2017) 81-88.

[35] H. Wang, *Sensors and Actuators: B, Chemical* **216** (2015) 298-306.
[36] H. J. Hecht, H. M. Kalisz, J. Hendle, R. D. Schmid, D. Schomburg, *Journal of Molecular Biology* **229** (1993)153-172.
[37] L. Wang, J. Yu, Y. Zhang, H. Yang, L. Miao, Y. Song, *ACS Applied Materials & Interfaces* **9** (2017) 9089-9095.
[38] J. Chen, *Journal of the Electrochemical Society* **164** (2017) B66-B73.
[39] M. Altikatoglu, Y. Basaran, C. Arioz, A. Ogan, H. Kuzu, *Applied Biochemistry and Biotechnology* **160** (2010) 2187-2197.
[40] V. Buk, *Materials Science & Engineering: C, Materials for Biological Application* **74** (2017) 307-314.
[41] X. Kang, Z. Mai, X. Zou, P. Cai, J. Mo, *Analytical Biochemistry* **369** (2007) 71-79.
[42] Sanaeifar, M. Rabiee, M. Abdolrahim, M. Tahriri, D. Vashaee, L. Tayebi, *Analytical Biochemistry* **519** (2017) 19-26.

J. Electrochem. Sci. Eng. **7(4)** (2017) 193-200; DOI: http://dx.doi.org/10.5599/jese.471

Open Access : : ISSN 1847-9286

www.jESE-online.org

Original scientific paper

Optical and electrochemical detection of a verotoxigenic *E. coli* gene using DNAzyme-labeled stem-loops

Gloria Longinotti[1], Gabriel Ybarra[1,✉], Javier Montserrat[2,3]

[1]*U.T. Nanomateriales, INTI-Procesos Superficiales, Instituto Nacional de Tecnología Industrial (INTI), Av. Gral. Paz 5445, B1650WAB San Martín, Argentina*

[2]*Universidad Nacional de General Sarmiento, J. M. Gutiérrez 1150, B1613GSX, Los Polvorines, Argentina*

[3]*Consejo Nacional de Investigaciones Científicas y Técnicas (CONICET), Argentina*

Corresponding authors E-mail: ✉E-mail: gabriel@inti.gov.ar; Tel./Fax: +51-11-4724-6333

Received: November 1, 2017; Revised: November 28, 2017; Accepted: November 30, 2017

Abstract

The activity of a peroxidase-mimicking DNAzyme was optimized to be used as a catalytic label in a stem-loop genosensor construction for quantifying the gene sequence Shiga-like toxin I of verotoxigenic E. coli. Experimental conditions such as pH, buffer composition, potassium ion concentration, and hemin-to-oligonucleotides ratio, were analyzed to maximize optical and electrochemical responses using microvolumes. Different stem-loop constructions were evaluated to obtain the optimum response against the target concentration. Linear ranges of 0.05-0.5 µM and limits of detection of 174 nM and 144 nM were estimated for the optical and electrochemical measurements, respectively. Selectivity was proved by assaying other verotoxigenic, enterotoxigenic and enteroinvasive sequences. The results show that, if a combination of small-volume electrochemical cells and low-cost untreated screen-printed electrodes with a relatively high geometric area is used, electrochemical measurements present similar sensitivity and limits of detection to the more usual optical ones, allowing the development of low-cost electrochemical biosensors based on the use of soluble DNAzymes as labels.

Keywords

Biosensors; Genosensors; DNAzyme Peroxidase; Verotoxigenic *E. coli*

Introduction

Peroxidase-mimicking DNAzymes are complexes formed by oligonucleotides containing guanine quadruplexes and hemin as prosthetic group, which catalyze the decomposition of hydrogen peroxide with the consequent oxidation of a substrate. Since their first reports by Breaker [1] and Joyce [2] in the late 1990s, the possibility of using DNAzymes as artificial enzymatic labels in

bioassays and biosensors has become apparent. DNAzymes have some advantages when compared to enzymes. DNAzymes are usually smaller than the corresponding enzymes, have a higher chemical stability, can be easily prepared using solid phase synthesis and can also be chemically modified. Moreover, their structures can be modulated for the adoption of active or inactive states. These versatile characteristics allow the combination, in a single DNA molecule, of both a recognition element and a catalytic label, as is the case of a peroxidase DNAzyme [3] combined with another DNA strand which acts as a biorecognition element [4]. Although this analytical strategy is attractive for the development of biosensors, its practical use can be hampered by a low sensitivity due to the lower catalytic activity of peroxidase DNAzymes when compared to peroxidase proteins.

The use of biorecognition-activated peroxidase-mimicking DNAzymes can be an especially attractive choice for the detection of complementary DNA sequences; for instance, those associated to bacterial toxins. In this regard, a considerable amount of work has been carried out for the detection of specific sequences of verotoxigenic *E. coli* (VTEC) or Shiga-toxigenic *E. coli*, including O157:H7 and other non-O157 serogroups, which produce verotoxins (verocytotoxins) that result in human diseases [5]. These toxins produce profound cytopathic effects in vero cells. Clinical symptoms may include bloody diarrhea and hemorrhagic colitis, along with complications associated with hemolytic-uremic syndrome (HUS), acute and chronic kidney disease, thrombotic thrombocytopenic purpura (TTP), neurological sequelae and death.

Optical detection has been the preferred means of transduction for the development of DNAzyme-based biosensors, usually with the use of ABTS, a reducing agent which becomes green-blue upon oxidation [4,6-9]. On the other hand, electrochemical transduction has been chosen when DNA strands were immobilized onto electroactive surfaces [10-12]. From the biosensors construction viewpoint, electrochemical detection shows a higher degree of electronic integration and a simplified design resulting from the fact that an electric signal is the natural result of electrochemical transduction [13]. Therefore, much effort has been devoted to developing optimized interactions between DNA strands and the electrode surface [14,15]. Although the use of soluble DNA structures avoids this issue, very few works have been published involving biosensors in which the catalytic activity of soluble DNAzymes is detected electrochemically [16].

Based on strategies similar to those reported previously [4-11,17], the aim of the present work was to prove the hypothesis that, by employing small-volume electrochemical cells in combination with inexpensive untreated printed electrodes, a sensitive detection of specific sequences of verotoxigenic *E. coli* could be carried out using DNAzymes as soluble electrochemical labels, yielding similar results to those obtained with the more usual optical detection. To that end, the conditions for the optimum response of a peroxidase DNAzyme were firstly optimized (pH, buffer composition, potassium ion concentration and hemin-to-oligonucleotides ratio) for electrochemical response. Secondly, different stem-loop oligonucleotides structures (recognition element and peroxidase DNAzyme) were designed and assayed for verotoxigenic *E. coli* sequences in order determine the best construction. Finally, response ranges, limits of detection and selectivity were studied for a stem-loop structure.

Experimental

Reagents and preparations

The sequences of DNA oligomers used are shown in Tables 1 and 2. The sequence showed in italic forms the DNAzyme known as $DZ5T_3$ upon combination with hemin. In order to prepare the oligomer-hemin complex, the DNA oligomer stock solution was heated at 95 °C for 5 minutes and

then diluted to a final concentration of 10 µM with TKT buffer. The hemin stock solution in DMSO was diluted to a final concentration of 20 µM with the same buffer. Finally, hemin was added to the oligomer solution with a hemin-to-DNA oligonucleotide ratio of 2:1. The mixture was allowed to stay at room temperature for 30 minutes.

Table 1. *DNA oligomers used in the construction of the DZ5T$_3$ DNAzyme and stem-loop sequences against Shiga-like toxin I genes of verotoxigenic. Underlined: complementary sequences that form the stem.* ***Bold****: DZ5T$_3$ sequence. Italic: target recognition element against Shiga-like toxin I genes of verotoxigenic* E. coli

	Sequence (5'→ 3')
DZ5T$_3$	TTTGGGTAGGGCGGGTTGGG
Stem loop I	**TTTGGGTAGGGCGGGTTGGG**TTTTT*TAGAACGCCCACTGAGATCATCCAGTGTTGT*CCCAACCC
Stem loop II	TACCCAAA*AGAACGCCCACTGAGATCATCCAGTGTTGTT***TTTGGGTAGGGCGGGTTGGG**
Stem loop III	CCCAACCC*AGAACGCCCACTGAGATCATCCAGTGTTGTT***TTTGGGTAGGGCGGGTTGGG**
Stem loop IV	CCGCCCTA*AGAACGCCCACTGAGATCATCCAGTGTTGTT***TTTGGGTAGGGCGGGTTGGG**

For the binding assay between the stem-loop and the target, the stock solutions of the DNA sequences were heated at 95 °C for 5 min and then diluted to a final concentration of 5 µM with TKT buffer. Subsequently, different volumes of target sequence solutions were mixed with a volume of stem-loop solution in different tubes and brought to the final volume with TKT buffer. The mixture was heated at 57 °C for 30 minutes. Finally, hemin was added and allowed to complex with DNA with stirring for 30 minutes at room temperature with a hemin-to-DNA ratio of 2:1. For the specificity assay, a similar procedure was followed employing the STXI sequence and five different oligonucleotides of others pathogenic *E. coli* (Table 2).

Table 2. *Pathogenic* E. coli *sequences [18]*

	Sequence (5'→ 3')
Shiga-like toxin I genes of verotoxigenic (STXI)	ACAACACTGGATGATCTCAGTGGGCGTTCT
Shiga-like toxin II genes of verotoxigenic (STXII)	GCGTTCTGTTCGCGCCGTGAATGAAG
Heat-labile toxin genes of enterotoxigenic (IT)	AGCGGCGCAACATTTCAGGTCGAAGTCC
Heat-stable toxin genes of enterotoxigenic (ST)	ATCAGAAAATATGAACAACACATTTTACTGCTGTGAAC
Adherence factor gene of enteropathogenic (EAF)	CGGCGCTGGTGATTTCGGGTTCGTCA
Invasiveness plasmid of enteroinvasive (IAL)	CTTATGTTCAAGGAAATAATTGTTGGCCTCCTTCTC

Optical and electrochemical measurements

UV-vis spectra were acquired with a Nanodrop 2000 Thermo Scientific spectrophotometer. Disposable acrylic cartridges with eight electrochemical cells were used for the electrochemical measurements [19,20]. Each cell with a volume of 40 µL contained three screen printed electrodes: a carbon working electrode with an area of 1.6 mm^2, a carbon counter electrode of approx. 10 mm^2, and one Ag|AgCl reference electrode. A Teq4 potentiostat was used.

Results and discussion

3.1 Optical and electrochemical determination of the catalytic activity of DZ5T$_3$-hemin DNAzyme

Peroxidase-mimicking DNAzymes catalyze the reduction of hydrogen peroxide by ABTS, which is in turn oxidized to ABTS$^{+\bullet}$. The rate of this reaction can be followed by measuring the absorbance at 420 nm, the absorbance maximum of ABTS$^{+\bullet}$ [21]. However, from the viewpoint of biosensors

design, it is more convenient to perform a single measurement at a given time rather than to determine the reaction rate as a series of measurements. A higher sensitivity and a lower limit of detection could be obtained if the accumulated concentration of formed $ABTS^{+\bullet}$ was determined after 3 minutes of reaction.

As reported earlier, the catalytic activity of peroxidase-mimicking DNAzyme depends on several factors, such as the concentration of potassium ions, buffer composition, pH, and the ratio between the concentration of hemin and oligonucleotides [3]. In order to obtain a high sensitivity when DNAzymes are used as labels, the optimum conditions for the catalysis with DNAzymes must be established. Under the experimental conditions used, the concentration of potassium ions did not show a significant influence on the kinetics, although a minimum concentration of 1.3 mM was found to be necessary. However, the hemin-to-oligonucleotide concentrations ratio and, especially, pH and buffer composition showed a strong influence on the reaction kinetics. The optimum values for the highest catalytic activity were found to be a pH of around 7.5 (Fig. 1a) and a ratio of hemin and oligonucleotides was found to be between 1.5 and 2.5 (Fig. 1b).

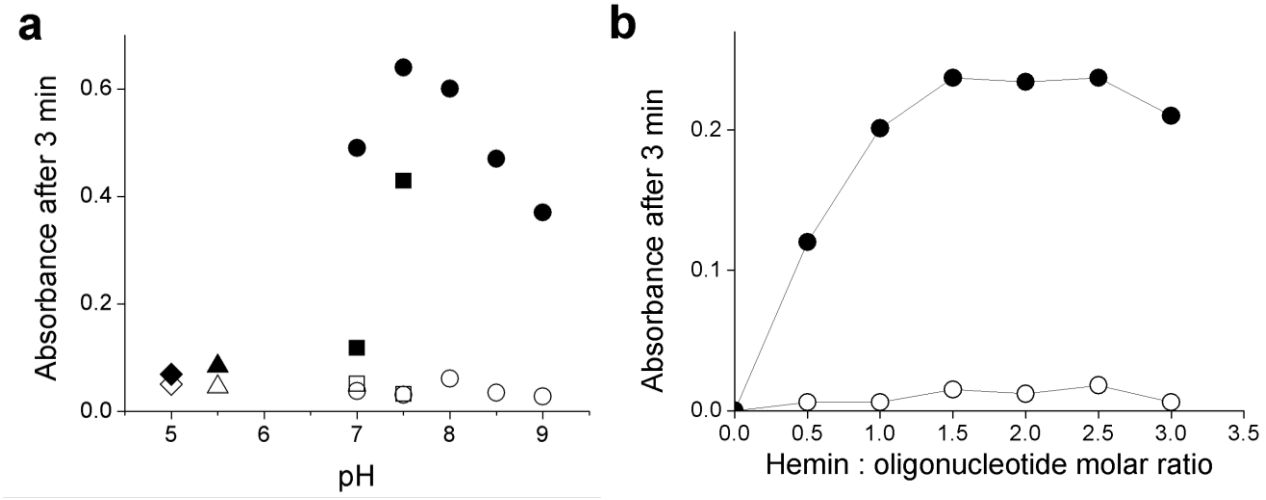

Fig. 1. (a) *Dependence of the catalytic activity of 1 µM DNAzyme (full) and 2 µM hemin (empty) on pH, determined by the absorbance measured at 420 nm developed by the oxidation of 50 µM ABTS after 3 min of reaction with 1 mM H_2O_2, oligonucleotide 0.31 µM, hemin 0.62 µM, ABTS 50 µM in buffer 25 mM: phthalate (♦), acetate (▲), phosphate (■), and tris-HCl (●);* ***(b)*** *Dependence of the catalytic activity with hemin:oligonucleotide ratio, with 1 µM DNAzyme, 0.5-3 µM hemin, determined by the absorbance measured at 420 nm developed by the oxidation of 50 µM ABTS after 3 min of reaction with 0.5 mM H_2O_2.*

Electrochemical methods can also be used to determine the concentration of $ABTS^{+\bullet}$. If a potential step is applied in conditions so that the limit current for the reduction of $ABTS^{+\bullet}$ is attained, the limit current follows the well-known Cottrell equation [25]. Current transients (shown in Fig. 2a) followed a linear relationship between the limit current and the inverse of the square root of time, as expected from the Cottrell equation (inset in Fig. 2a). As can be seen in Fig. 2b, after a period of catalytic decomposition of hydrogen peroxide (in this case, 3 min), the current measured at a given time after applying a potential step (20 s) was also directly proportional to the concentration of $DZ5T_3$ DNAzyme. Therefore, soluble DNAzymes can also be used as labels whose activity can be determined by chronoamperometry.

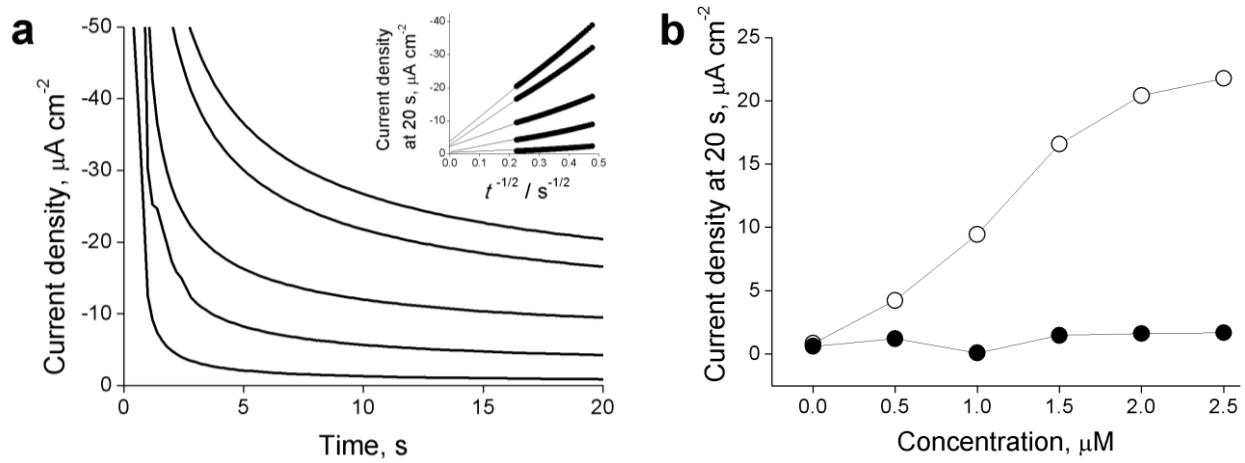

Fig. 2. (a) *Current transients for different concentrations of DNAzyme, from bottom to top: 0-2.5 μM. Inset: plots of* i vs. $t_m^{-1/2}$*;* ***(b)*** *Current measured at 20 s with a potentiostatic step after 5 min of reaction for different concentrations of DNAzyme (●) and hemin (○).*

Optical and electrochemical determination of E. coli O157 verotoxigenic gene using DNAzyme-labelled stem-loops

Four different DNA sequences (Table 1) differing in their complementary sequences were designed in order to analytically determine the presence of an *E. coli* O157 gene. These constructions included the $DZ5T_3$ sequence, a fragment which is complementary to a specific region of an *E. coli* verotoxigenic gen [18] and another moiety that allows the complete DNA sequence to be folded into a stem-loop structure. Fig. 3 shows the schematic representation for the detection of a target DNA strand with a stem-loop containing a complementary sequence and a $DZ5T_3$ sequence which adopts an active DNAzyme conformation after hybridization with the target.

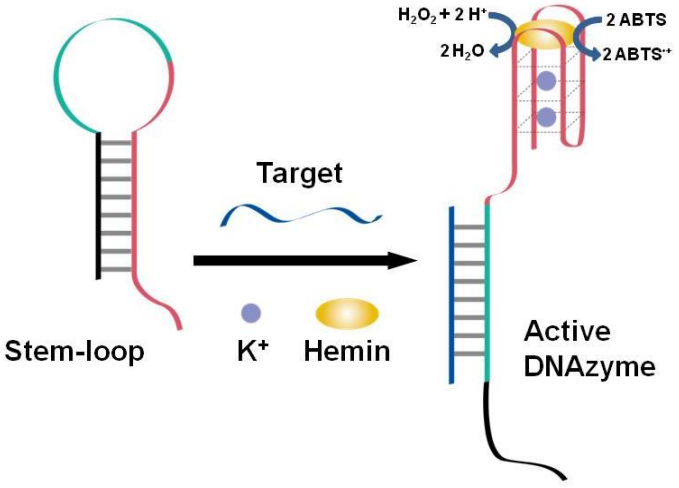

Fig. 3. *Schematic representation of bioanalysis with a stem-loop for the recognition of a target DNA sequence upon activation of a DNAzyme. Black: complementary sequences to part of $DZ5T_3$ sequence. Green: complementary sequences to Shiga-like toxin I genes of verotoxigenic. Pink: $DZ5T_3$ sequence. Blue: Shiga-like toxin I genes of verotoxigenic sequences*

The activity of the four DNA stem-loops designed were spectrophotometrically tested (Fig. 4). In all cases, the sequence complementary to the target was located in the loop region and the stem length was 8 mer. The first construction (stem-loop I, Table 1) was designed with the $DZ5T_3$ sequence located in the 5' end, while the other constructions were prepared using the $DZ5T_3$ located in the 3' end of the stem-loop. Another difference between the designs of the stem-loops was the

moiety that blocked the $DZ5T_3$ avoiding the active conformation. In the case of stem-loop I, the last 8 bases of the 3' end of $DZ5T_3$ were blocked. In all other three cases (stem-loops II-IV), different zones of the $DZ5T_3$ sequence were explored.

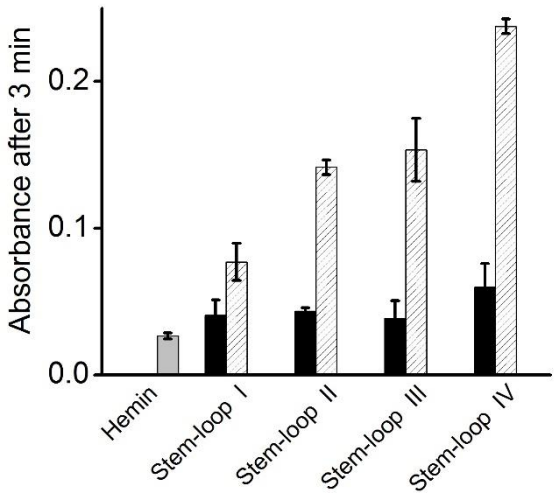

Fig. 4. *Absorbance at 420 nm after 3 min of reaction for 1 µM hemin (grey) and stem-loops I, II, III and IV 0.5 µM + 1 µM hemin, in the absence (black) and the presence of 0.5 µM target (strips).*

A poor signal-to-noise ratio was obtained for stem-loop I. This low response could be related to an inappropriate stem-loop design. Zhang et al. [22] have reported that modifications at the 3' end of sequence corresponding to the peroxidase DNAzyme produced a decrease in the catalytic activity. It was assumed that, by adding bases at the 3' end of the $DZ5T_3$ oligonucleotide, the ability of the oligonucleotide to bind hemin decreases.

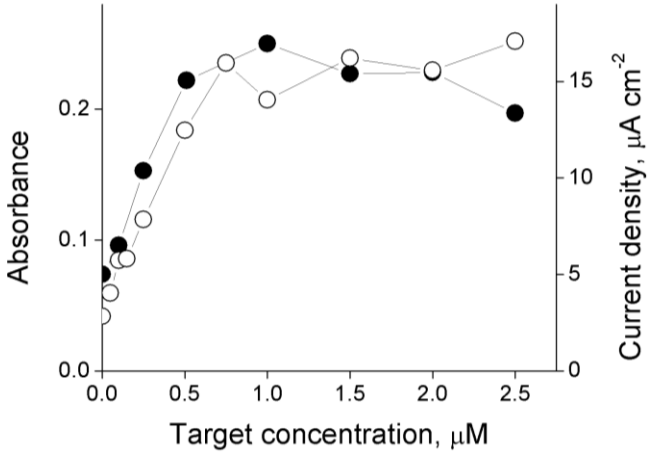

Fig. 5. *Variation of absorbance (●) and limit current density at 20 s (o) after 3 min of reaction for a stem-loop concentration of 0.5 µM, 1 µM hemine, 20 mM KCl, 0.2 M NaCl, 0.05 % triton x-100, 3.4 mM ABTS 0.5 mM H_2O_2.*

For stem-loops II-IV, a significant increase in the absorbance with the concentration of the target was observed. These three constructions differ in the region where the $DZ5T_3$ sequence was blocked (near the 5’ end, the intermediate region, or near the 3’ end). No significant differences in the results were obtained with designs II and III. The results for stem-loop IV showed a higher sensitivity, and a maximum value of absorbance was obtained when stem-loop and target were used in a one-to-one ratio. Due to these results, stem-loop IV was chosen for successive measurements.

Fig. 5 shows the absorbance at 420 nm and the density current obtained at a fixed time (20 s) produced by $ABTS^{+\bullet}$ as a function of different concentrations of the target complementary sequence.

It can be seen that the concentration of $ABTS^{+\bullet}$ increases almost linearly for low values of target concentration and reaches a plateau for values higher than 1 µM. It can also be noted that even in the absence of the target sequence, a certain amount of $ABTS^{+\bullet}$ is formed, which can be assumed to be the consequence of the formation of a certain amount of DNAzyme. From the data shown in Fig. 5, it can be concluded that approximately 13 % of the total possible concentration of available DNAzyme structure was formed in the absence of the target sequence. On the other hand, when an excess of target was used, the formation of the DNAzyme structure reached about 80 % of the expected maximum value. For stem-loop IV, limits of detection of 174 nM and 144 nM were estimated for the optical and electrochemical measurements, respectively.

Selectivity against Shiga-like toxin I verotoxigenic gene

In order to evaluate the stem-loop IV selectivity for Shiga-like toxin I verotoxigenic gene (STXI, Table 2), an activity assay employing different sequences for other *E. coli* toxins was carried out. Fig. 6 shows the density current response for stem-loop IV (1 µM) in the presence of different targets at the same concentration. Target sequences different from STXI showed responses similar to stem-loop IV in the absence of the STXI target, thus indicating the selectivity of the construction.

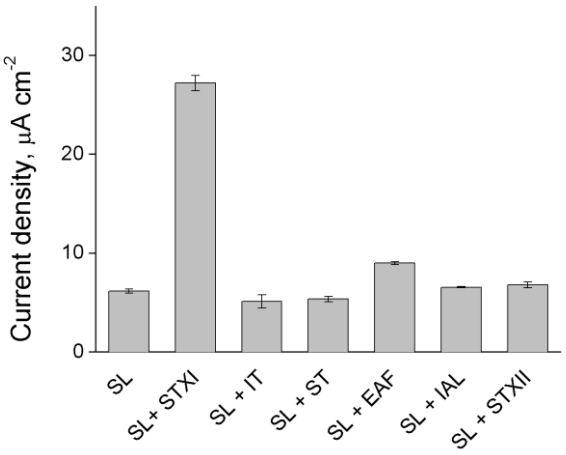

Fig. 6. *Current density measured for the different E. coli pathogenic sequences (see Table 2) employing stem-loop IV.*

Conclusions

The catalytic activity of a peroxidase-mimicking DNAzyme depends on factors such as pH, buffer composition, potassium ions concentration, and the hemin-to-oligonucleotides ratio. For the $DZ5T_3$ DNAzyme, it was found that the buffer composition is as important as pH itself, and the highest catalytic activity was obtained when a TRIS buffer of pH 7.5 was used. Additionally, a minimum amount of potassium ions of 1.3 mM and a minimum hemin-to-oligonucleotides ratio of 2:1 were found to be necessary to achieve a high catalytic activity. $DZ5T_3$ DNAzyme was used as a label, combined in a stem-loop with a DNA sequence which recognizes a specific sequence of Shiga-like toxin I of verotoxigenic *E. coli*. It was demonstrated that the catalytic activity obtained was specific and proportional to the amount of the target concentration. The $DZ5T_3$ DNAzyme catalytic activity was followed optically and electrochemically. It is worth noting that soluble DNA species were used throughout this work, avoiding problems usually found with immobilized DNA strands, related to undesired DNA-surface interactions. The combination of electrochemical cells with relatively small volume and low-cost screen printed working electrodes with a relatively high geometric area allowed obtaining amperometric measurements with sensitivities and limits of detection

comparable to optical methods. To our knowledge, this is the first report of a DNAzyme-based electrochemical bioanalysis with these features, which opens the way to the development of cost-effective portable devices for the diagnosis of a verotoxigenic *E. coli* infection using of DNAzymes as labels.

References

[1] R. R. Breaker, *Nature Biotechnology* **16** (1997) 427–431.
[2] R. R. Breaker, G. F. Joyce, *Chemical Biology* **1** (1994) 223–229.
[3] P. Travascio, Y. Li, D. Sen, *Chemical Biology* **5** (1998) 505–517.
[4] Y. Xiao, V. Pavlov, T. Niazov, A. Dishon, M. Kotler, I. Willner, *Journal of American Chemical Society* **126** (2004) 7430–7431.
[5] D. L. Woodward, C. G. Clark, R. A. Caldeira, R. Ahmed, F. G. Rodgers, *Canadian Journal of Infectious Diseases and Medical Microbiology* **13** (2202) 321–330.
[6] P. Travascio, a J. Bennet, D. Y. Wang, D. Sen, *Chemistry & Biology* **6** (1999) 779–787.
[7] D. Li, B. Shlyahovsky, J. Elbaz, I. Willner, *Journal of American Chemical Society* **129** (2007) 5804–5805.
[8] C. Teller, S. Shimron, I. Willner, *Analitycal Chemistry* **54** (2009) 9114–9119.
[9] J. Kosman, B. Juskowiak. *Analytica Chimica Acta* **707** (2011) 7-17.
[10] Q. Guo, Y. Bao, X. Yang, K. Wang, Q. Wang, Y. Tan, *Talanta* **83** (2010) 500–504.
[11] G. Pelossof, R. Tel-Vered, J. Elbaz, I. Willner, *Analitycal Chemistry* **82** (2010) 4396–4402.
[12] F. Li, L. Yang, M. Chen, Y. Qian, B. Tang, *Biosensors & Bioelectronics* **41** (2013) 903–906.
[13] C. Moina, G. Ybarra, *Advances in Immunoassay Technology*, Norman H. L. Chiu, Ed. Zagreb, Croatia, 2012, pp. 65–80.
[14] F. Ricci, N. Zari, F. Caprio, S. Recine, A. Amine, D. Moscone, G. Palleschi, K. W. Plaxco, *Bioelectrochemistry* **76** (2009) 208–213.
[15] K. J. Cash, F. Ricci, K. W. Plaxco, *Journal of American Chemical Society* **131** (2009) 6955–6957.
[16] D. Zhang, J. Nie, F.-T. Zhang, L. Xu, Y.-L. Zhou, X.-X. Zhang, *Analitycal Chemistry* **85** (2013) 9378–9382.
[17] J. Kosman, Y. T. Wu, A. Gluszynska, B. Juskowiak, *Analytical and Bioanalytical Chemistry* **406** (2014) 7049–7057.
[18] L. Watterworth, E. Topp, H. Schraft, K. T. Leung, *Journal of Microbiological Methods* **60** (2005) 93–105.
[19] M. E. Cortina, L. J. Melli, M. Roberti, M. Mass, G. Longinotti, S. Tropea, P. Lloret, D. A. R. Serantes, F. Salomon, M. Lloret, A. J. Caillava, S. Restuccia, J. Altcheh, C. A. Buscaglia, L. Malatto, J. E. Ugalde, L. Fraigi, C. Moina, G. Ybarra, A. E. Ciocchini, D. J. Comerci, *Biosensensors & Bioelectronics* **80** (2016) 24–33.
[20] J. Molinari, C. Moina, G. Ybarra, *Journal of Electrochemical Science and Engineering* **5** (2015) 9–16.
[21] R. E. Childs, W. G. Bardsley, *Biochemical Journal* **145** (1975) 93–103.
[22] X. Zhou, M. Zhang, H. Li, M. Deng, X. Weng, H. Ma, S. Feng, Y. Zhou, *Chemistry &. Biodiversity* **9** (2012) 170–180.
[23] F. Violante-Mota, E. Tellechea, J. F. Moran, G. Sarath, R. Arredondo-Peter, *Phytochemistry* **71** (2010) 21–26.
[24] A. J. Bard, L. R. Faulkner, *Electrochemical Methods, Fundamentals and Applications*, John Wiley & Sons, U.S.A., 2001.

J. Electrochem. Sci. Eng. **7(4)** (2017) 201-212; DOI: http://dx.doi.org/10.5599/jese.458

Open Access : : ISSN 1847-9286

www.jESE-online.org

Original scientific paper

Graphene-modified nickel foam electrode for cathodic degradation of nitrofuranzone: Kinetics, transformation products and toxicity

Ya Ma[1,2], Yanhong Tang[1,✉], Kai Yin[2], Shenglian Luo[2], Chengbin Liu[2], Tian Liu[2], Liming Yang[2,3]

[1]*College of Materials Science and Engineering, Hunan University, Changsha 410082, P. R. China*
[2]*State Key Laboratory of Chemo/Biosensing and Chemometrics, Hunan University, Changsha 410082, P. R. China*
[3]*Key Laboratory of Jiangxi Province for Persistent Pollutants Control and Resources Recycle, Nanchang Hangkong University, Nanchang 330063, P. R. China*

Corresponding authors E-mail: ✉tangyh@hnu.edu.cn

Received: October 10, 2017; Revised: November 7, 2017; Accepted: November 27, 2017

Abstract

Simple, efficient, and durable electrodes are highly demanded for practical electrochemical process. In this study, a reduced graphene oxide modified nickel foam electrode (GR-Ni foam) was facilely prepared via one-step cyclic voltammetry electrodeposition of graphene oxide suspension onto the Ni foam. The electrochemical degradation of nitrofuranzone (NFZ, a kind of typical antibiotics) was studied on the GR-Ni foam cathode. The cyclic voltammetry and electrochemical impedance spectra analysis confirmed that presence of GR loading accelerated the electron transfer from the cathode surface to NFZ. With the applied cathode potential of −1.25 V (vs. Ag/AgCl), the removal efficiency of NFZ (C_0 = 20 mg L^{-1}) at the GR-Ni foam electrode reached up to 99 % within 30 min, showing a higher reaction rate constant (0.1297 min^{-1}) than 0.0870 min^{-1} at the Pd-Ni foam and 0.0186 min^{-1} at the Ni foam electrode. It was also found that the pH, dissolved oxygen and NFZ initial concentration have slight effect on NFZ degradation at the GR-Ni foam electrode. The reactions first occurred at nitro groups (-NO_2), unsaturated C=N bonds and N-N bonds to generate furan ring-containing products, and then these products were transformed into linear diamine products. The direct reduction by electrons was mainly responsible for NFZ reduction at the GR-Ni foam electrode. Even after 18 cycles, the removal efficiency of NFZ still reached up to 98 % within 1 h. In addition, the cathodic degradation process could eliminate the antibacterial activity of NFZ. The GR-Ni foam electrode would have a great potential in electrochemical process for treating wastewater containing furan antibiotics.

Keywords

Graphene; Nickel foam; Nitrofuranzone; Electrochemical degradation

Introduction

Antibiotics discharged into the environments (*e.g.*, soil and aquatic ecosystems) could increase antibiotic resistance of ecosystems [1-5], bringing about potential threats to aquatic life and even human health. Nitrofuranzone (NFZ) as a low-cost and high-efficiency broad spectrum of antimicrobial agents of nitrofurans is widely used for the treatment of gastrointestinal and dermatological infections in animal husbandry and aquaculture [6]. However, the overuse and misuse of them have led to adverse environmental effects and antibiotics resistance transfer to human pathogenic microbes [7-12]. Because of the microbial resistance of antibiotics, it is very difficult to efficiently remove them using conventional methods (*e. g.*, activated sludge) in waste-water treatment plants. As a result, the water containing nitrofuran antibiotics is discharged frequently into the environment [13-16]. Thus, wastewater containing antibiotics contaminants must be decontaminated before it is discharged into the environment.

A variety of methods including photolysis [17,18], adsorption [19-21], and advanced oxidation process [22, 23] have been developed to remove antibiotics. However, photolysis process greatly relies on adequate illumination or involve addition of catalysts, adsorption process is limited due to poor adsorption capacity towards low-concentration antibiotics, and advanced oxidation process involves catalysts or a great deal of reagents that lead to the secondary pollution. Compared to these methods, electrochemical method has been regarded as one of the most effective technology due to its environmental-friendly and high-efficiency properties [24-26]. It is believed that electrochemical reduction process is governed and affected by atomic H* mediation produced on noble metal catalysts [27,28]. However, the limited mining capability and prohibitive cost of noble metals hinder their field application. Furthermore, noble metal catalysts are easily poisoned in the presence of organics and electrochemical process [29,30]. To move the practical application of electrochemical process forward, avoidance of noble metal catalysts is necessary. As a result, developing high-performance electrode materials is crucial for electroreductive reactions in practice.

In this work, we developed a graphene-modified Ni foam electrode (GR-Ni foam), which was facilely synthesized *via* one-step cyclic voltammetry electrodeposition technique. The as-prepared electrode has the following merits: (i) Ni foam has the advantages including low cost, high stability and porous structure and (ii) graphene has excellent conductivity for fast electron transfer and good adsorption properties towards organic molecules. Ability of this electrode to decompose NFZ was tested using cathodic degradation process. The fate of NFZ during the degradation process was investigated to uncover its destruction pathway. The toxicity of NFZ and the degradation products was evaluated by antimicrobial property. An electrochemical system based on a simple and effective GR-Ni foam electrode could potentially serve for treatment of wastewater containing antibiotics.

Experimental

Nitrofuranzone (NFZ), citric acid, sodium citrate, palladium chloride ($PdCl_2$), sodium sulfate (Na_2SO_4), sulfuric acid (H_2SO_4) and tertiary butanol (*t*-BuOH) were used as received from Aladdin (Shanghai, China). Natural flake graphite with an average particle size of about 50 μm was purchased from Shanghai Carbon Co., Ltd. (Shanghai, China), Ni foam (pore density 100 ppi, thickness 1.5 mm) was purchased from Shenzhen Lifetion Environmental Protection Equipment Co., Ltd (Shenzhen China), and Nafion 117 solution (5 wt%) was purchased from Hesen Co., Ltd (Shanghai, China). Ultrapure water was used throughout all the experiments.

Ni foam was first ultrasonically cleaned in acetone, HCl solution and ultrapure water, respectively. Graphite oxide (GO) suspension was synthesized from the flake graphite using modified Hummers method [31]. The graphene modified Ni foam (GR-Ni foam) electrode was fabricated by cyclic voltammetric electrolysis of GO suspension (0.3 g L^{-1}) using an electrochemical workstation (CHI 660C, Chenhua Co., Ltd., Shanghai, China) with a three-electrode system. Ni foam was applied as the working electrode, Pt foil as the counter electrode, and a saturated calomel electrode (SCE) as the reference electrode, respectively. The potential scan was performed between −1.5 and 0.6 V at a rate of 50 mV s^{-1} for 80 cycles. As a control, the Pd-loading Ni foam (Pd loading amount of 0.135 mg cm^{-2}) was prepared through one-step electrodeposition of a mixture solution of $PdCl_2$ (1 mM) and H_2SO_4 (5 mM) under magnetic stirring at −1.0 V for 60 s. Finally, all the working electrodes were thoroughly washed with ultrapure water and dried at room temperature.

The morphology and composition of as-prepared materials were characterized by field emission scanning electron microscope (SEM, Hitachi S-4800). The crystal structure was characterized using X-ray diffraction equipment (XRD, Cu Kα radiation, λ=1.54056 Å). Raman spectra were measured using a Labram-010 Raman spectrometer with a 632.8 nm laser. The Pd content in Pd-Ni foam was determined by inductively coupled plasma-optical emission spectrometry (ICP-OES, 5110ICP, Agilent). The cyclic voltammetry (CV), electrochemical impedance spectra (EIS) and electric double-layer capacitor (EDLC) characterization were performed in a dual chamber equipped with CHI 660C electrochemical workstation using a Pt foil as the counter electrode and SCE as the reference electrode. CV curves were recorded in the scan range between −1.2 and 0 V. The EIS was recorded by applying an alternating current (AC) voltage with 5 mV amplitude in a frequency range 100000-0.01 Hz at the open circuit voltage. The EDLC characterization was performed between −0.15 and −0.05 V. All the experiments were performed at room temperature.

A dual-chamber reactor was used for the electroreduction of NFZ, which was separated into a cathode cell (20 mL) and anode (20 mL) cell by a cation exchange membrane. The working area of the prepared electrode was 1×1 cm^2. A platinum plate (1×1 cm^2) was used as the counter electrode, and a silver chloride electrode (Ag/AgCl) was employed as the reference electrode. The counter electrode was put into the anode chamber, and the working electrode and reference electrode were inserted into the cathode chamber. A constant potential on the cathode was controlled using the amperometric *i-t* technique by setting up initial *E* with the electrochemical workstation (CHI660C). The cathode chamber was magnetically stirred at a rate of 1000 rpm. Before triggering reaction, the dissolved oxygen in the reactor was removed by bubbling N_2 gas.

The concentrations and the decomposed products of NFZ were quantified using a high-performance liquid chromatography (HPLC, Hitachi L-2130, Japan) with an L-2420 UV-vis detector. The mobile phase contained 50 % methanol and 50 % water at a rate of 1 mL min^{-1}, the wavelength was 250 nm, and the column temperature was 30 °C. NFZ transformation products were analyzed by a triple quad HPLC-ESI-tqMS (Aglient 1290/6460) and LTQ-Orbitrap Velos Pro (Thermo Fisher Scientific). The positive mode was employed in electrospray ionization. To avoid the possible contamination of equipment, all samples were filtered through 0.22 μm filters before the detection.

Luminescent bacteria such as *Escherichia coli* DH5*α* [24] (a typical Gram-negative bacterium) was used to evaluate toxicity of substances. The cells of the strains were harvested at the end of their exponential growth phase. The separated cells were washed with a sterile phosphate buffer solution (PBS) (50 mM) and then inoculated into 24 mL of 3-fold-diluted Luria−Bertani (LB) medium. To evaluate this non-specific toxicity, the levels of bacteria bioluminescence (0.3 mL bacteria source) were measured in 6 mL solution of PBS blank, 20 mg L^{-1} NFZ and degradation products, respectively.

This system was loaded into a 50 mL conical flask and shaken in a shaking incubator with a shaking rate of 180 rpm at 30 °C. The absorbance of optical density at 600 nm (OD_{600}) could reflect the concentration of the living bacteria.

Results and discussion

Characterizations

The SEM images of Ni foam and GR-Ni foam are shown in Figure 1(a-b). The surface of bare Ni foam was smooth (Figure 1a), while the surface became rough after depositing graphene sheets (Figure 1b). On the basis of the analysis of Raman spectroscopy (Figure 1c), the two prominent bands observed in GR-Ni foam around 1327 and 1586 cm^{-1} were assigned to the D and G bands of carbon, respectively, indicating that GR sheets were successfully deposited onto the Ni foam substrate. The EIS was applied to investigate the electrical properties of the GR-Ni foam and Ni foam cathodes. The typical Nyquist plots are shown in Figure 1d. The GR-Ni foam had a smaller semicircle diameter than bare Ni foam, indicating that the introduction of GR increased conductivity and promoted electron transfer [32,33]. Additionally, cyclic voltammetry (CV) can determine the double layer capacitance (C_{dl}) which is linearly proportional to effective active surface area [34,35]. The CV current responses for the Ni foam and GR-Ni foam electrodes in the region from –0.15 to –0.05 V *vs.* SCE should be mostly due to the charging of the double layer (Figure S1a and b).

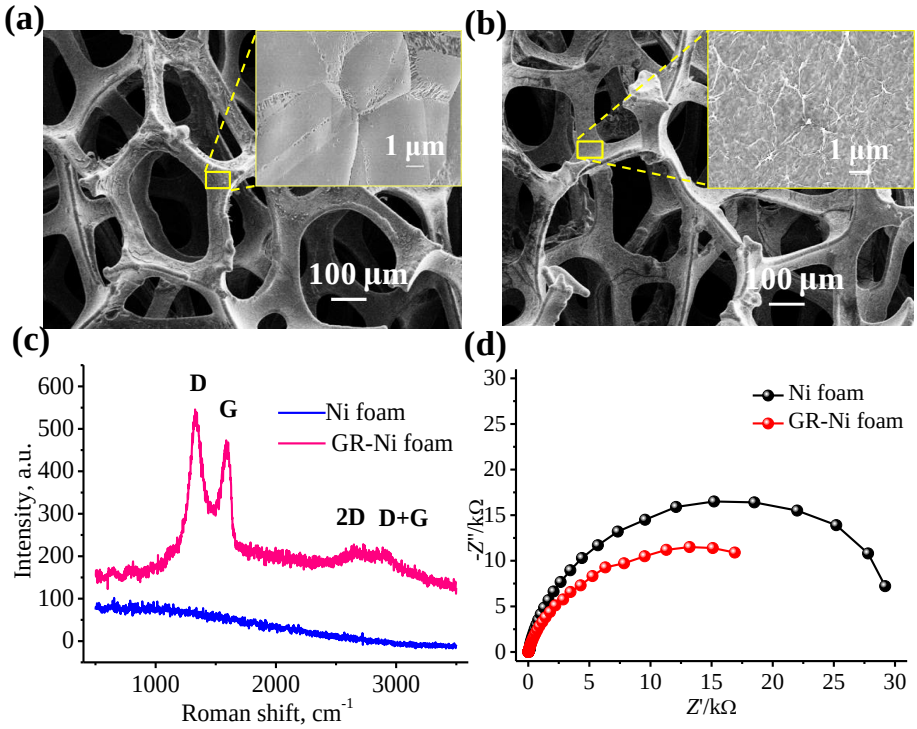

Figure 1. *SEM images of* ***(a)*** *Ni foam and* ***(b)*** *GR-Ni foam,* ***(c)*** *Raman spectra of Ni foam and GR-Ni foam electrodes, and* ***(d)*** *Nyquist plots of Ni foam and GR-Ni foam electrodes in 0.1 M Na_2SO_4.*

The double layer capacitance was estimated by plotting the Δj (j_a-j_c) at –0.10 V against the scan rate (Figure S1c), and the GR-Ni foam had a much larger double-layer capacitance than Ni foam. The results strongly indicated that the loaded GR could increase the density of catalytically active sites.

As a control, the Pd-Ni foam electrode was prepared through one-step electrodeposition of a $PdCl_2$ solution using Ni foam as the working electrode. The SEM image showed that dendritic Pd

particles lay on the surface of Ni foam (Figure S2). The XRD result confirmed the existence of metallic Pd (Figure S3). The content of Pd in Pd-Ni foam was 9.4 mg/g determined by ICP-OES analysis.

NFZ degradation on the prepared electrodes

The characteristic shape of cyclic voltammograms (CV) is a result of the potential which is dependent on the changes in surface concentrations of redox system and simultaneous diffusion processes [36]. The CV tests were applied for the reduction of NFZ at different electrodes (Figure 2a). In the presence of NFZ, both, the Ni foam and the GR-Ni foam showed characteristic reduction peak of NFZ at –0.95 V (peaks c_1 and a_2) [24,26,37]. In addition, there appeared another reduction peak of NFZ at –0.60 V (peak a_1) for the GR-Ni foam. This result indicated that NFZ reduction occurred on the GR-Ni foam at a smaller potential than on the Ni foam, which could probably be attributed to the reduction of overpotential due to introduction of GR. Additionally, there was an oxidation peak at about –0.50 V. Similar CV behaviors were observed during the reduction of nitroaromatics nitrobenzene and chloramphenicol [38-40] and attributed to the reversible reactions of nitroso and hydroxylamino intermediates. In contrast, the GR-Ni foam did not show any current peak in the absence of NFZ.

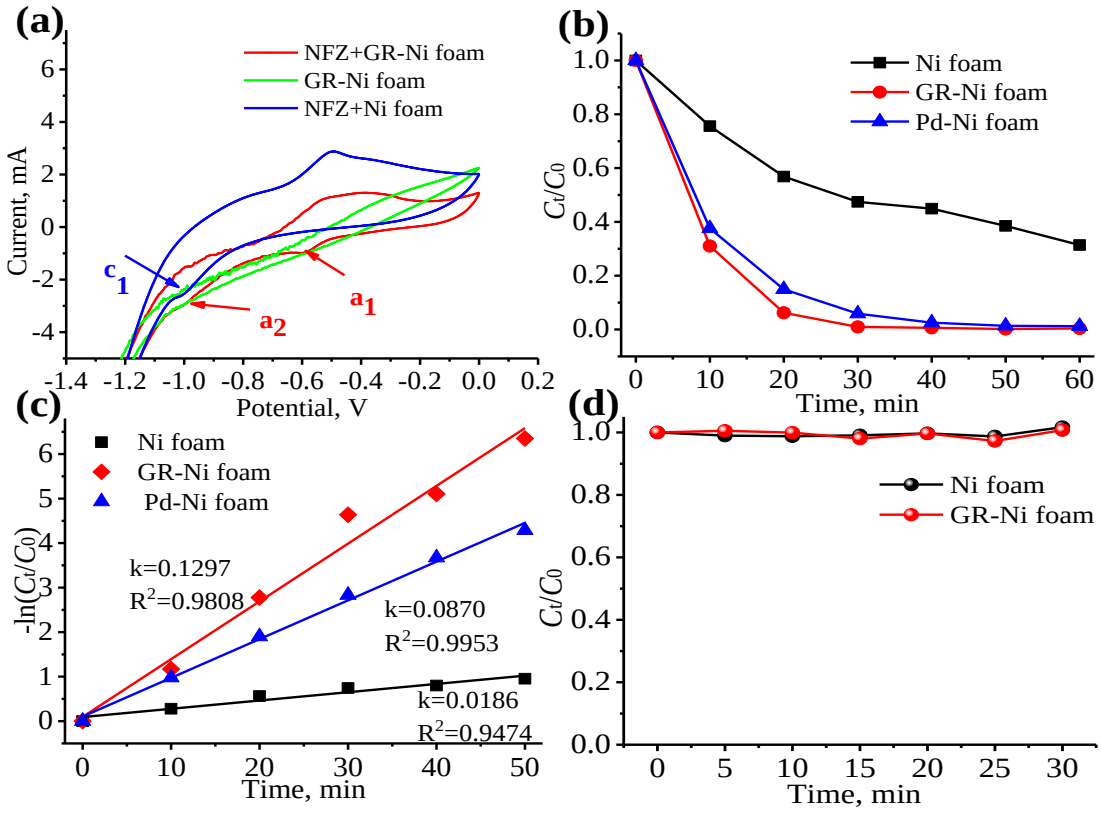

Figure 2. (a) *Cyclic voltammograms (vs. Ag/AgCl, 0.1 M Na_2SO_4, 20 mg L^{-1} NFZ, pH = 4.28),* ***(b)*** *degradation efficiency,* ***(c)*** *degradation kinetics of NFZ at −1.25 V vs. Ag/AgCl, and* ***(d)*** *adsorption of NFZ without bias potential.*

The performances of different (Ni foam, GR-Ni foam, and Pd-Ni foam) electrodes for removal of NFZ were determined under the same experimental condition (0.1 M Na_2SO_4 solution, pH 4.28, initial NFZ concentration of 20 mg L^{-1}, and applied potential of –1.25 V *vs.* Ag/AgCl) (Figure 2b). Only 53 % NFZ was degraded on the bare Ni foam electrode within 30 min, while the removal efficiency of NFZ on the GR-Ni foam reached up to 99 % what was higher than on the Pd-Ni foam (94 %) within 30 min. The results indicate that the GR-Ni foam would seriously compete with noble metals (e.g.

Pd)–based electrocatalysts for electrocatalytic degradation of nitrofuran antibiotics. The degradation of NFZ followed a pseudo-first order kinetic model, $-\ln(C_t/C_0) = kt + b$, where t is the reaction time (min), k is the reaction rate constant (min^{-1}), b is a constant, and C_t and C_0 are the NFZ concentrations (μM) at times of $t = t$ and $t = 0$, respectively. The reaction rate constants (k) of NFZ were 0.1297 min^{-1} (coefficient $R^2 = 0.9808$) for the GR-Ni foam and 0.087 min^{-1} ($R^2 = 0.9953$) for the Pd-Ni foam, which were 6.97 and 4.68 times higher than 0.0186 min^{-1} ($R^2 = 0.9474$) for the Ni foam, respectively (Figure 2c). Figure 2d showed that the adsorption basically did not contribute to the removal of NFZ.

Effect of different parameters

The influence of different experimental parameters such as cathode potential, initial concentration, solution pH and dissolved oxygen on electrochemical removal efficiency of NFZ on the GR-Ni foam was also investigated (Figure 3). The degradation rate markedly increased with cathode potential from –0.35 to –1.25 V (*vs.* Ag/AgCl) (Figure 3a).

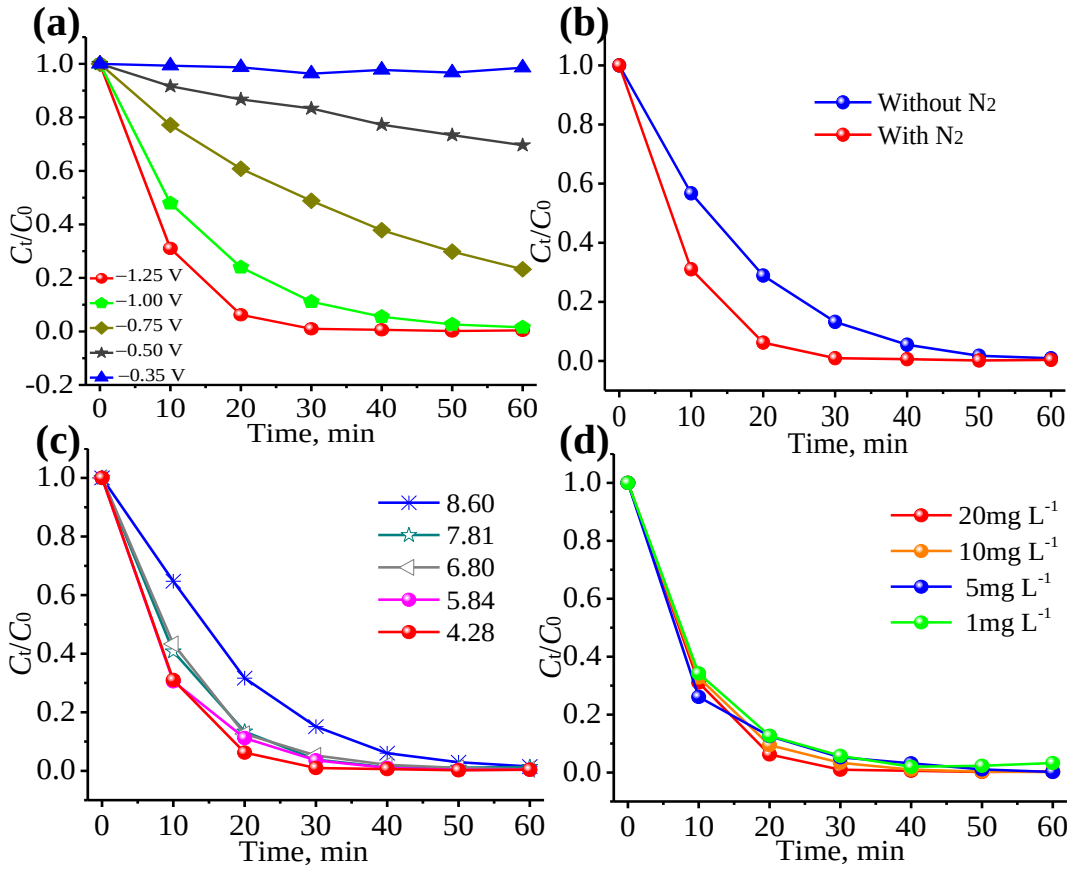

Figure 3. *Effect of different experimental parameters on reduction of NFZ on GR-Ni foam cathode:* ***(a)*** *potential (0.1M Na_2SO_4, 20 mg L^{-1} NFZ, pH 4.28),* ***(b)*** *dissolved oxygen (−1.25 V* vs. *Ag/AgCl, 0.1 M Na_2SO_4, 20 mg L^{-1} NFZ, pH 4.28),* ***(c)*** *solution pH (−1.25 V* vs. *Ag/AgCl, 0.1 M Na_2SO_4, 20 mg L^{-1} NFZ), and* ***(d)*** *initial NFZ concentration (−1.25 V* vs. *Ag/AgCl, 0.1 M Na_2SO_4, pH 4.28).*

More negative cathode potential could produce more available electrons leading to higher efficiency in NFZ reduction. NFZ was nearly completely degraded at the applied potential of –1.25 V within 30 min. The NFZ degradations were fitted to the pseudo-first reaction kinetics with rate constant k of 0.0060 min^{-1} ($R^2 = 0.9904$), 0.0240 min^{-1} ($R^2 = 0.9996$), 0.0728 min^{-1} ($R^2 = 0.9999$) and 0.1297 min^{-1} ($R^2 = 0.9808$) at –0.5, –0.75, –1.0 and –1.25 V, respectively (Figure S4).

It has already been reported that dissolved oxygen could compete with the contaminant for both the electrons and atomic H* on the cathode surface, suppressing thus the target contaminant reduction [27,41]. By purging the solution with N_2, the dissolved oxygen was removed. The degradation of NFZ on the GR-Ni foam electrode was studied with and without N_2 sparging (Figure 3b). It was observed that the dissolved oxygen had slight effect on NFZ degradation. In addition, NFZ degradation was promoted by decreasing pH from 8.60 to 4.28 (Figure 3c). The generation of atomic H* is favored in acid solutions, therefore acidic solution facilitates the reduction process by consuming H*[41-43]. Even so, NFZ degradation efficiency reached up to 83 % at pH 8.60 within 30 min, suggesting that the GR-Ni foam electrode could be used in a wide range of pH for NFZ degradation. Also, the NFZ degradation slightly increased with increasing initial concentration of NFZ and the degradation efficiency still reached approximately 90 % within 30 min when the initial concentration of NFZ was as low as 1 mg L^{-1} (Figure 3d).

It is clearly seen that the GR-Ni foam electrode is feasible to work in practical wastewater with different pH, dissolved oxygen and NFZ concentration.

Transformation pathway and proposed degradation mechanism of NFZ

The degradation products of NFZ on different (Ni foam, GR-Ni foam and Pd-Ni foam) electrodes were measured using LC/MS. The extraction ion chromatogram (EIC) for the detection of these products is shown in Figure S5-S7. Three furan ring-containing products and two linear chain terminal products were detected in the three electrode systems. The furan ring-containing products were (5-nitro-2-furyl) methanamine (NFM), (5-amino-2-furyl)methylene-hydrazinecarboxamide (AMH) and (5-hydroxyamino-2-furyl)methyl-hydrazinecarboxamide (HMH), corresponding to m/z $[M+Na]^+$ of 165, 191 and 209, respectively. The linear chain terminal products were 5-amino-pentanamide (APA) and 5-hydroxycadaverine (HOC), corresponding to m/z $[M+Na]^+$ of 139 and 141, respectively. The Na^+ was from Na_2SO_4 electrolyte. The transformation pathway of degradation products was illustrated in Scheme 1. The reactions first occurred at nitro groups ($-NO_2$), unsaturated C=N bonds and N-N bonds to obtain HMA, NFM and AMH products, and then these products were transformed into linear APA products which were finally reduced to HOC.

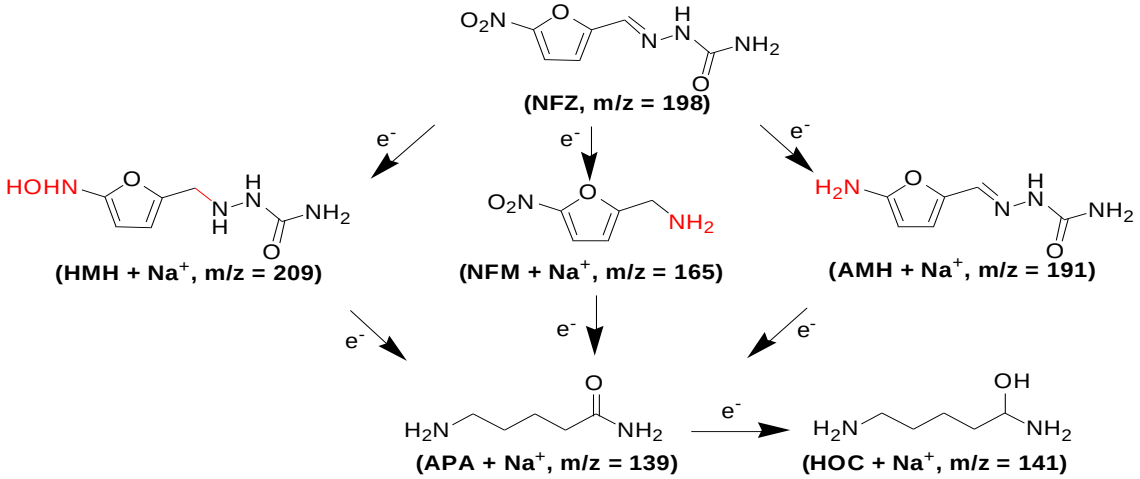

Scheme 1. *Transformation pathway of degradation products*

It is believed that electrocatalytic reduction of organic pollutants involves direct electron transfer reduction and atomic H*-mediated reduction [41-43]. Tertiary butanol (*t*-BuOH) as a scavenger of H* [44] was used to study NFZ degradation. The *t*-BuOH addition (0, 2 and 5.0 mM) did not show effect on NFZ reduction over bare Ni foam, indicating a direct electron transfer reduction

(Figure 4a). In contrast, only at a high t-BuOH concentration of 5.0 mM, the NFZ reduction on GR-Ni foam electrode was influenced (Figure 4b). Even so, the removal efficiency of NFZ still achieved 88.7 % within 30 min at 5.0 mM *t*-BuOH. It was reported that hydrogen produced in electrochemical process could be adsorbed on GR and subsequently activated to atomic H*[45-47]. It can be inferred that the produced atomic H* may be in part responsible for NFZ reduction. The results indicated that direct electron transfer reduction played a crucial role in NFZ reduction on the GR-Ni foam. Expectedly, a significant inhibition of NFZ reduction was observed at the Pd-Ni foam in the presence of *t*-BuOH (Figure 4c). Pd is well-known to have the unique property of activating protons to atomic H* and subsequently adsorbing atomic H*[48,49]. Therefore, the reduction of NFZ at the Pd-Ni foam mainly proceeded via H* mediation.

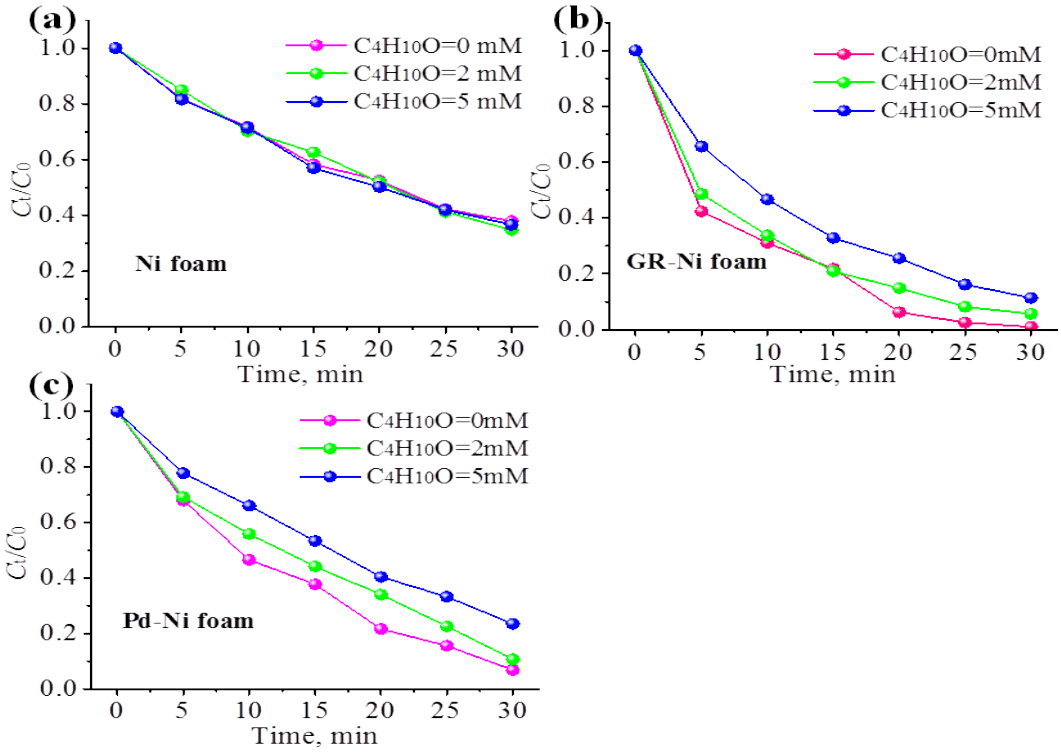

Figure 4. *Effect of t-BuOH (0, 2 and 5 mM) on NFZ reduction on* ***(a)*** *Ni foam,* ***(b)*** *GR-Ni foam, and* ***(c)*** *Pd-Ni foam electrodes (−1.25 V vs. Ag/AgCl, 0.1 M* Na_2SO_4*, 20 mg* L^{-1} *NFZ, pH=4.28).*

The furan ring-containing products at different electrodes were further quantified using HPLC with UV-vis detector (Figure S8). The linear APA and HOC products could not be quantified using HPLC due to lack of UV-vis absorption. The results are shown in Figure 5. It was found that the transformation products were generated rapidly from the start on the GR-Ni foam electrode, indicating fast reaction kinetics. After approximately 50 min, the concentrations of these products decreased, what is indicative of the further reduction to linear APA and HOC products. In addition, concentrations of the products increased monotonically on the Ni foam electrode, suggesting a limited deep degradation to linear APA and HOC products. It was also seen that after 60 min, although the removal efficiency of NFZ on the Pd-Ni foam electrode reached almost 100 % (Figure 2b), the concentrations of the transformation products were lower than those for the Ni foam and GR-Ni foam electrodes. The results indicated that the furan ring-containing transformation products were more easily reduced to linear APA and HOC products using the Pd-Ni foam electrode with the aid of atomic H*. 4

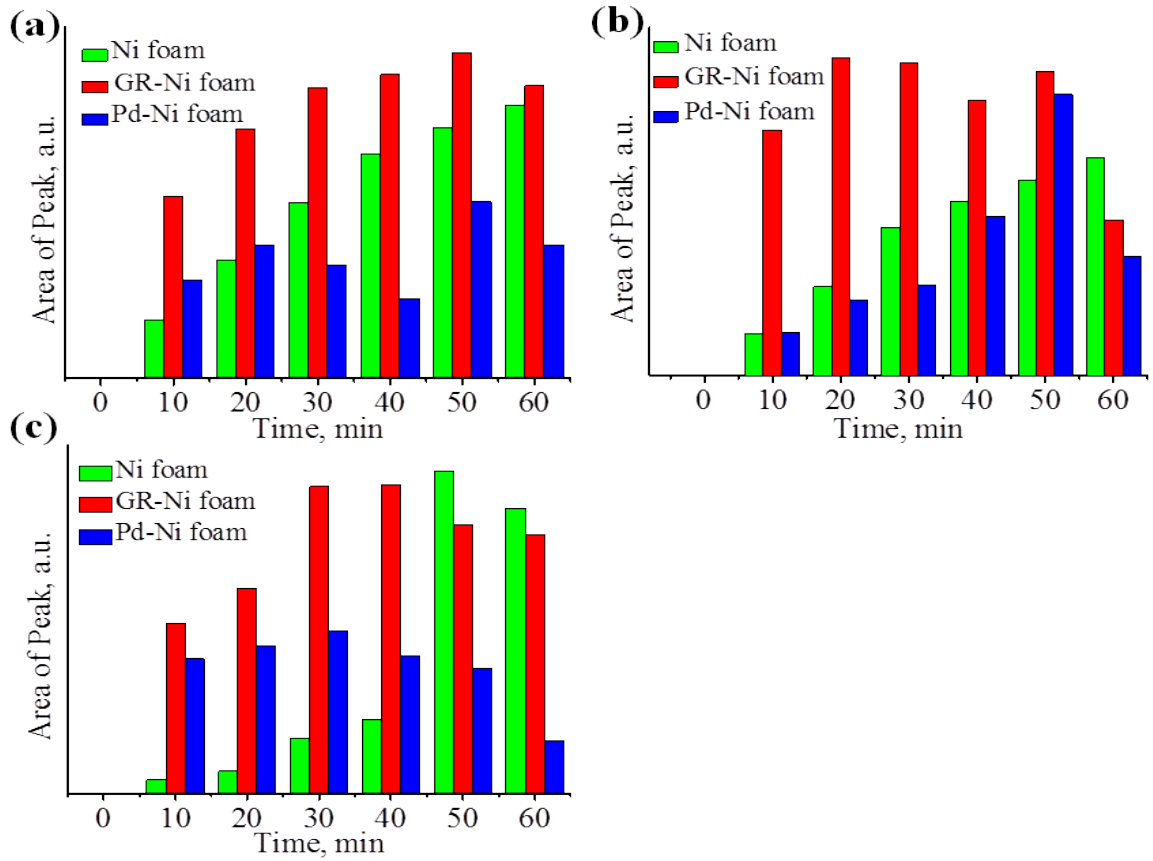

Figure 5. *NFZ degradation product concentrations of* ***(a)*** *NFM,* ***(b)*** *AMH,* ***(c)*** *HMH on Ni foam, GR-Ni foam and Pd-Ni foam electrodes (−1.25 V* vs. *Ag/AgCl, 0.1 M Na_2SO_4, 20 mg L^{-1} NFZ, pH 4.28).*

Toxicity assessment of degradation products

E. coli DH5α (a typical Gram-negative bacterium) luminescent bacteria is commonly used to evaluate the toxicity of substances. The antibacterial activity assay was performed using *E. coli* DH5α (Figure 6a), which was reflected by the optical density of the bacterial strains at 600 nm (OD_{600}). The growth of *E. coli* DH5α was nearly completely inhibited in the presence of 20 mg L^{-1} NFZ. In contrast, in the presence of terminal degradation products, the growth of *E. coli* DH5α was slightly inhibited and then returned to normalization after 10 h. Generally, after the nitro group reduction, heterocyclic amine products were less toxic and considerably easier to be mineralized by aerobic bacteria than the nitro group containing antibiotics [50]. So, it can be stated that the electrochemical treatment of wastewater containing NFZ using the GR-Ni foam electrode is efficient to reduce the risk of adverse environmental effect.

Electrode durability

The durability of electrodes is crucial for practical application of electrochemical process. To evaluate the durability of the GR-Ni foam electrode, electrocatalytic reduction of NFZ was performed after 18 cycles (each cycle time was 1 h) (Figure 6b). Significantly, in the 18th cycle, the removal efficiency of NFZ still reached up to 98 %, being nearly the same as in the first cycle. The results indicated that the GR-Ni foam electrode was very stable, showing a great potential of practical application.

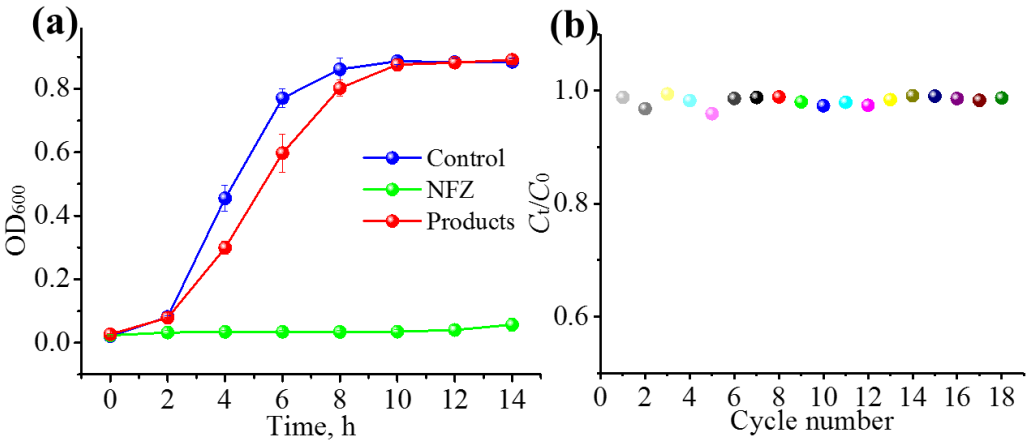

Figure 6. (a) *Toxicity assessment of control, NFZ (20 mg L^{-1}) and degradation products (−1.25 V* vs. *Ag/AgCl, 0.1 M Na_2SO_4, 20 mg L^{-1} NFZ,* t *= 1 h, pH 4.28).* ***(b)*** *durability of GR-Ni foam electrode (−1.25 V* vs. *Ag/AgCl, 0.1 M Na_2SO_4, 20 mg L^{-1} NFZ).*

Conclusions

An efficient GR-Ni foam electrode was facilely prepared using one-step electrodeposition of GO suspension onto the Ni foam. By application of the GR-Ni foam electrode as cathode, the efficient and rapid degradation of NFZ was achieved in the electrochemical reduction process without using an expensive noble metal catalyst. The degradation rate of NFZ on the GR-Ni foam electrode was higher than that on the Pd-Ni foam electrode, and the degradation products showed much lower antibacterial activity than the NFZ parent compound. Because of its high effectiveness and stability, low cost, and environmental friendliness, the GR-Ni foam electrode could play a beneficial role as a promising cathode in electrochemical process for efficient removal of nitrofuran antibiotics in water.

Acknowledgements*: This work was supported by the National Natural Science Foundation of China (51778218 and 51478171).*

References

[1] J. Davies, D. Davies, *Microbiology and Molecular Biology Reviews* **74(3)** (2010) 417-433.
[2] S. Jechalke, H. Heuer, J. Siemens, W. Amelung, K. Smalla, *Trends in Microbiology* **22(9)** (2014) 536-545.
[3] C. Q. Gnamba, F. T. A. Appia, E. M. H. Loba, I. Sanogo, L. Ouattara, *Journal of Electrochemical Science and Technology* **5(2)** (2015) 129-143.
[4] C. P. Andam, G. P. Fournier, J. P. Gogarten, *FEMS Microbiology Reviews* **35(5)** (2011) 756-767.
[5] E. Marti, E. Variatza, J.L. Balcazar, *Trends in Microbiology* **22(1)** (2014) 36-41.
[6] P. Thongsrisomboon, B. Liawruangrath, S. Liawruangrath, S. Satienperakul, *Food Chemistry* **123(3)** (2010) 834-839.
[7] [7] A. Auro, H. Sumano, L. Ocampo, A. Barragan, *The Pharmacogenomics Journal* **4(1)** (2004) 24-28.
[8] N. Shrivastav, B. I. Fedeles, D. Li, J. C. Delaney, L. E. Frick, J. J. Foti, G. C. Walker, J. M. Essigmann, *Plos One* **9(4)** (2014) e94716.
[9] Y. Ni, P. Wang, S. Kokot, *Biosensors and Bioelectronics* **38(1)** (2012) 245-251.
[10] Y. Hiraku, A. Sekine, H. Nabeshi, K. Midorikawa, M. Murata, Y. Kumagai, S. Kawanishi, *Cancer Letters* **215(2)** (2004) 141-150.
[11] Y. Hong, X. Lin, X. Cui, L. Zhou, K. A. S. Al-Rasheid, J. Li, *Ecological Indicators* **54** (2015) 153-160.
[12] Y. Hong, S. Liu, X. Lin, J. Li, Z. Yi, K. A. Al-Rasheid, *Environmental Science and Pollution Research International* **22(12)** (2015) 9544-9553.

[13] I. Michael, L. Rizzo, C. S. McArdell, C. M. Manaia, C. Merlin, T. Schwartz, C. Dagot, D. Fatta-Kassinos, *Water Research* **47(3)** (2013) 957-995.
[14] X. Tian, Y. Xu, X. Song, X. Gong, Y. Liu, Q. Zhou, Z. Wang, C. Xia, *Marine Pollution Bulletin* **112(1-2)** (2016) 393-398.
[15] W.-H. Yu, T.-S. Chin, H.-T. Lai, *International Biodeterioration and Biodegradation* **85** (2013) 517-526.
[16] C. Ardsoongnearn, O. Boonbanlu, S. Kittijaruwattana, L. Suntornsuk, *Journal of Chromatography. B* **945-946** (2014) 31-38.
[17] M. De Luca, S. Mas, G. Ioele, F. Oliverio, G. Ragno, R. Tauler, *International Journal of Pharmaceutics* **386(1-2)** (2010) 99-107.
[18] B. L. Edhlund, W. A. Arnold, K. McNeill, *Environmental Science and Technology* **40(17)** (2006) 5422-5427.
[19] B. Wang, X. L. Lv, D. Feng, L. H. Xie, J. Zhang, M. Li, Y. Xie, J. R. Li, H. C. Zhou, *Journal of the American Chemical Society* **138(19)** (2016) 6204-6216.
[20] W. Y. Ying, X. Z. Hu, *Journal of Dispersion Science and Technology* **37(5)** (2015) 613-624.
[21] Z. Z. Yuan, X. Z. Hu, Fullerenes, *Nanotubes and Carbon Nanostructures* **23(7)** (2014) 640-648.
[22] H. Mestankova, A. M. Parker, N. Bramaz, S. Canonica, K. Schirmer, U. von Gunten, K. G. Linden, *Water Research* **93** (2016) 110-120.
[23] P. Liu, H. Zhang, Y. Feng, F. Yang, J. Zhang, *Chemical Engineering Journal* **240** (2014) 211-220.
[24] D. Kong, B. Liang, H. Yun, H. Cheng, J. Ma, M. Cui, A. Wang, N. Ren, *Water Research* **72** (2015) 281-292.
[25] A. Rahi, N. Sattarahmady, R. Dehdari Vais, H. Heli, *Sensors and Actuators B: Chemical* **210** (2015) 96-102.
[26] C. d. L. Brito, G. H. G. Trossini, E. I. Ferreira, M. A. La-Scalea, *Journal of the Brazilian Chemical Society* **24**(2013) 1964-1973.
[27] W. Xie, S. Yuan, X. Mao, W. Hu, P. Liao, M. Tong, A. N. Alshawabkeh, *Water Research* **47(11)** (2013) 3573-3582.
[28] J. Y. Lee, J. G. Lee, S. H. Lee, M. Seo, L. Piao, J. H. Bae, S. Y. Lim, Y. J. Park, T. D. Chung, *Nature Communications* **4** (2013) 2766.
[29] X. Zhao, M. Yin, L. Ma, L. Liang, C. Liu, J. Liao, T. Lu, W. Xing, *Energy and Environmental Science* **4(8)** (2011) 2736.
[30] P.J. Ferreira, Y. Shao-Horn, D. Morgan, R. Makharia, S. Koch, H.A. Gasteiger, Journal of the Electrochemical Society **152(11)** (2005) 65-78.
[31] L. Yang, Y. Tang, D. Yan, T. Liu, C. Liu, S. Luo, ACS Applied Materials and Interfaces **8(1)** (2016) 169-176.
[32] D. Li, Z. Mao, Y. Zhong, W. Huang, Y. Wu, P. Peng, *Water Research* **103** (2016) 1-9.
[33] D. Turcio-Ortega, D. Fan, P. G. Tratnyek, E. J. Kim, Y. S. Chang, *Environmental Science and Technology* **46(22)** (2012) 12484-92.
[34] M. Liu, L. Yang, T. Liu, Y. Tang, S. Luo, C. Liu, Y. Zeng, *Journal of Materials Chemistry A* **5(18)** (2017) 8608-8615.
[35] M. A. Lukowski, A. S. Daniel, F. Meng, A. Forticaux, L. Li, S. Jin, *Journal of the American Chemical Society* **135(28)** (2013) 10274-10277.
[36] J. Heinze, *Angewandte Chemie International Edition* **23(11)** (1984) 831-847.
[37] C. S. Reday, S. J. Reddy, *Electroanalysis* **4(5**) (1992) 595-599.
[38] B. Liang, H. Y. Cheng, D. Y. Kong, S. H. Gao, F. Sun, D. Cui, F. Y. Kong, A. J. Zhou, W. Z. Liu, N. Q. Ren, W. M. Wu, A. J. Wang, D. J. Lee, *Environmental Science and Technology* **47(10)** (2013) 5353-5361.
[39] A. J. Wang, H. Y. Cheng, B. Liang, N. Q. Ren, D. Cui, N. Lin, B. H. Kim, K. Rabaey, *Environmental Science and Technology* **45(23)** (2011) 10186-10193.
[40] A. Ait Sidi Mou, A. Ouarzane, M. El Rhazi, *Journal of Electrochemical Science and Engineering* **7(3)** (2017) 111.
[41] R. Mao, N. Li, H. Lan, X. Zhao, H. Liu, J. Qu, M. Sun, *Environmental Science and Technology* **50(7)** (2016) 3829-37.
[42] H. Lan, R. Mao, Y. Tong, Y. Liu, H. Liu, X. An, R. Liu, *Environmental Science and Technology* **50(21)** (2016) 11872-11878.
[43] A. Li, X. Zhao, Y. Hou, H. Liu, L. Wu, J. Qu, *Applied Catalysis B: Environmental* **111-112** (2012) 628-635.

[44] S. P. Mezyk, W. J. Cooper, K. P. Madden, D. M. Bartels, *Environmental Science and Technology* **38(11)** (2004) 3161-3167.
[45] M. Pumera, *Energy and Environmental Science* **4(3)** (2011) 668-674.
[46] N. Park, S. Hong, G. Kim, S. H. Jhi, *Journal of the American Chemical Society* **129(29)** (2007) 8999-9003.
[47] G. K. Dimitrakakis, E. Tylianakis, G. E. Froudakis, *Nano Letters* **8(10)** (2008) 3166.
[48] W. C. Conner, J. L. Falconer, *Chemical Reviews* **95(3)** (1995) 759-788.
[49] B. P. Chaplin, M. Reinhard, W. F. Schneider, C. Schuth, J. R. Shapley, T. J. Strathmann, C. J. Werth, *Environmental Science and Technology* **46(7)** (2012) 3655-3670.
[50] B. A. Donlon, E. Razo-Flores, G. Lettinga, J. A. Field, *Biotechnology and Bioengineering* **51(4)** (1996) 439-449.

J. Electrochem. Sci. Eng. **7(4)** (2017) S1-S6

Open Access : : ISSN 1847-9286

www.jESE-online.org

Supplementary material to

Graphene-modified nickel foam electrode for cathodic degradation of nitrofuranzone: Kinetics, transformation products and toxicity

Ya Ma[1,2], Yanhong Tang[1,✉], Kai Yin[2], Shenglian Luo[2], Chengbin Liu[2], Tian Liu[2], Liming Yang[2,3]

[1]*College of Materials Science and Engineering, Hunan University, Changsha 410082, P. R. China*
[2]*State Key Laboratory of Chemo/Biosensing and Chemometrics, Hunan University, Changsha 410082, P. R. China*
[3]*Key Laboratory of Jiangxi Province for Persistent Pollutants Control and Resources Recycle, Nanchang Hangkong University, Nanchang 330063, P. R. China*

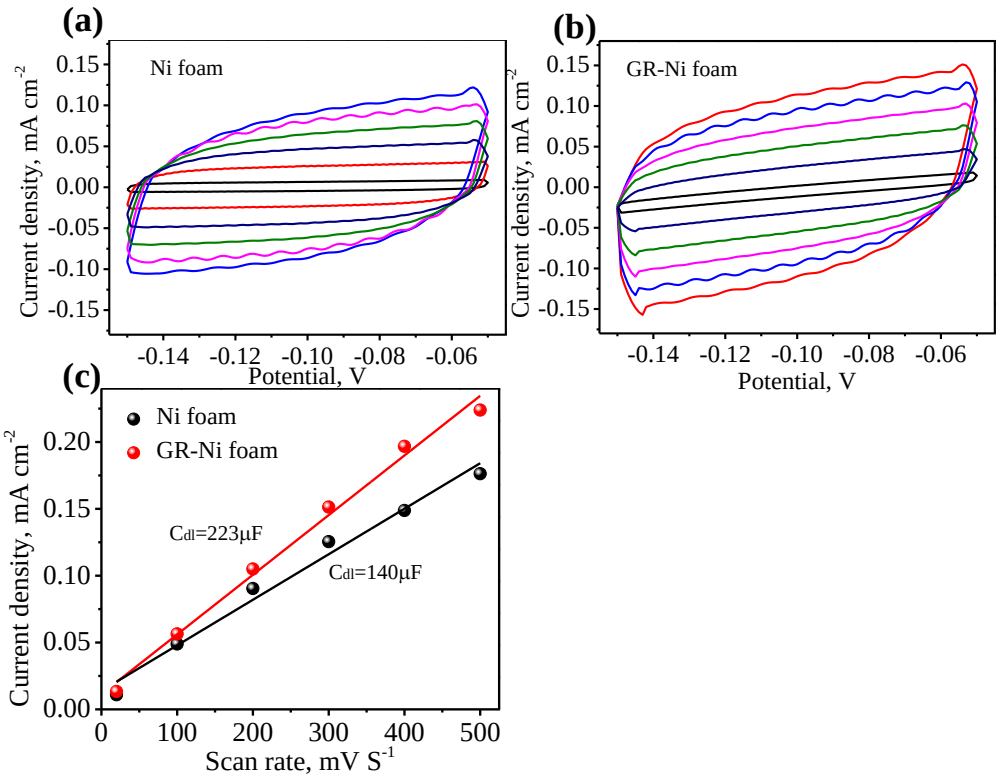

Figure S1. *Cyclic voltammograms in the region between –0.15 and –0.05 V* vs. *SCE at* ***(a)*** *Ni foam and* ***(b)*** *GR-Ni foam;* ***(c)*** *Current density at -0.10V plotted against scan rate fitted to a linear regression for the estimation of* C_{dl}.

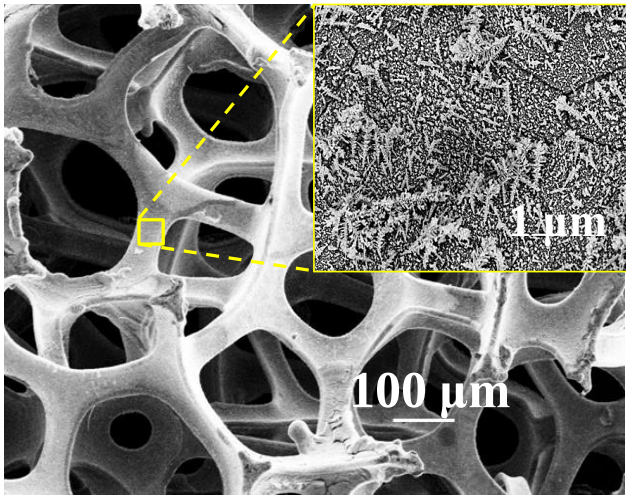

Figure S2. *SEM image of Pd-Ni foam*

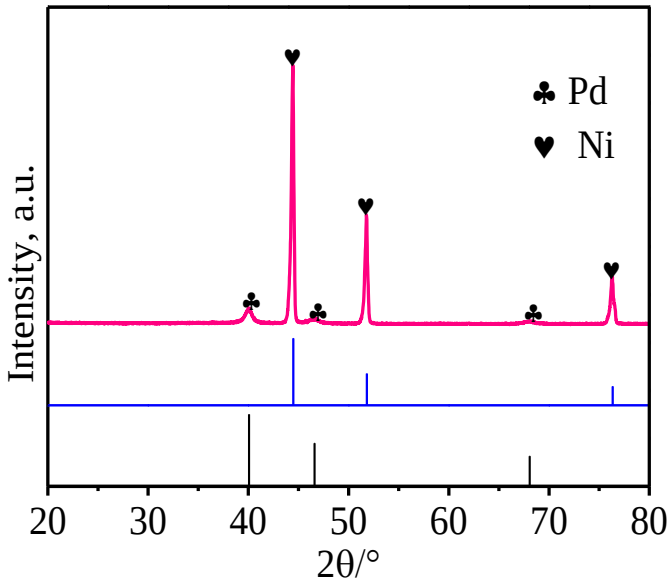

Figure S3. *XRD pattern of Pd foam*

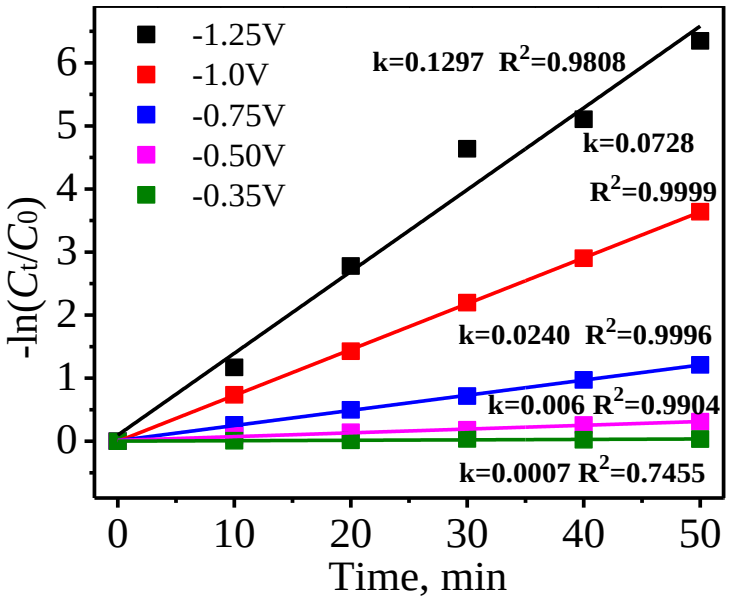

Figure S4. *Reaction kinetics at different cathode potential for NFZ degradation at GR-Ni foam electrode (0.1 M Na_2SO_4, 20 mg L^{-1} NFZ and pH 4.28)*

NFM+Na$^+$ (m/z 165)

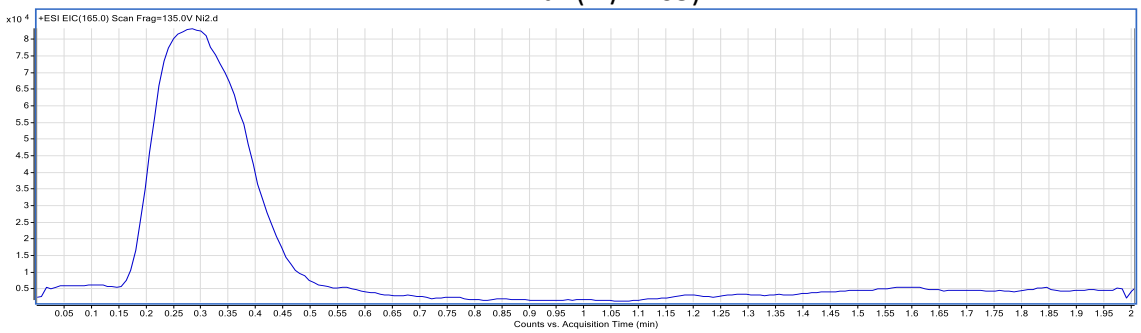

AMH+Na$^+$ (m/z 191)

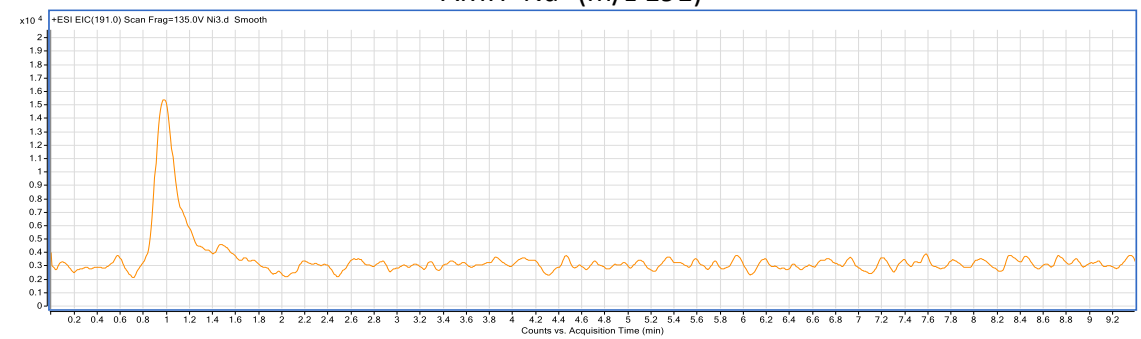

HMH+Na$^+$ (m/z 209)

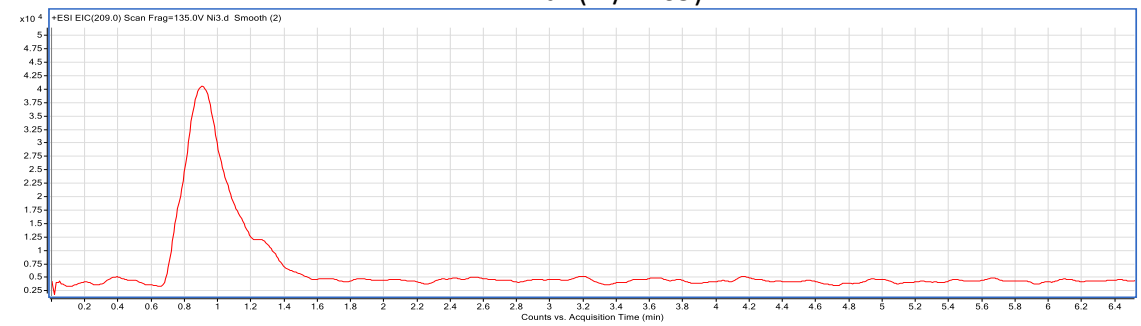

APA+Na$^+$ (m/z 139)

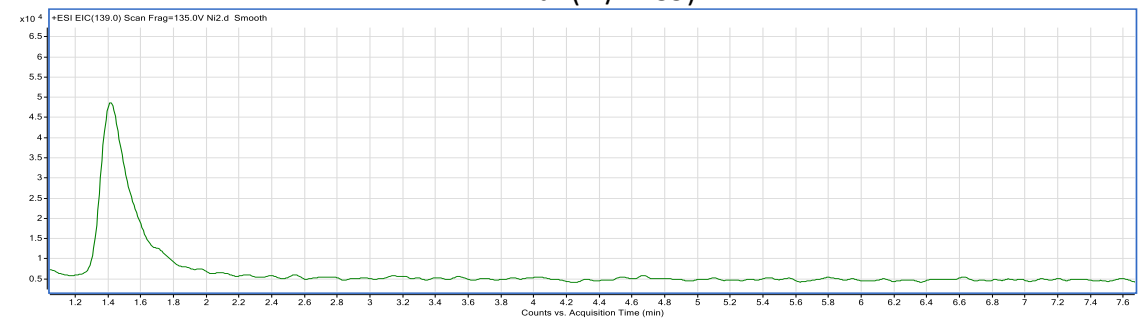

HOC+Na$^+$ (m/z 141)

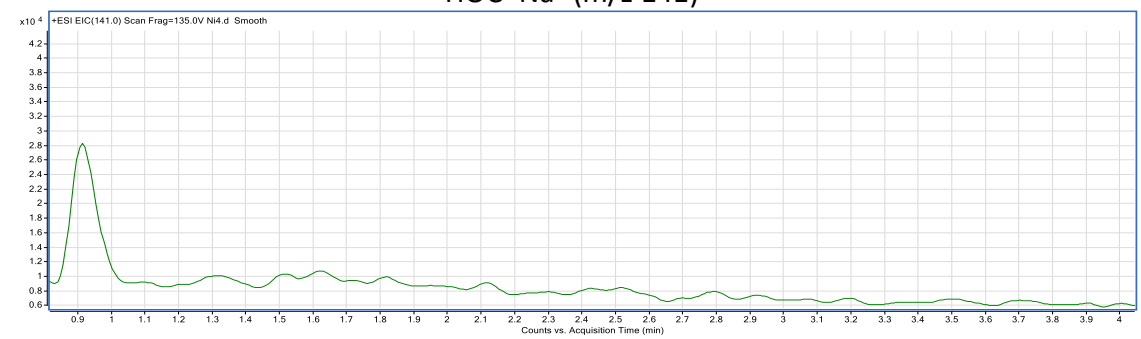

Figure S5*. MS identification of NFZ degradation products at Ni foam electrode*

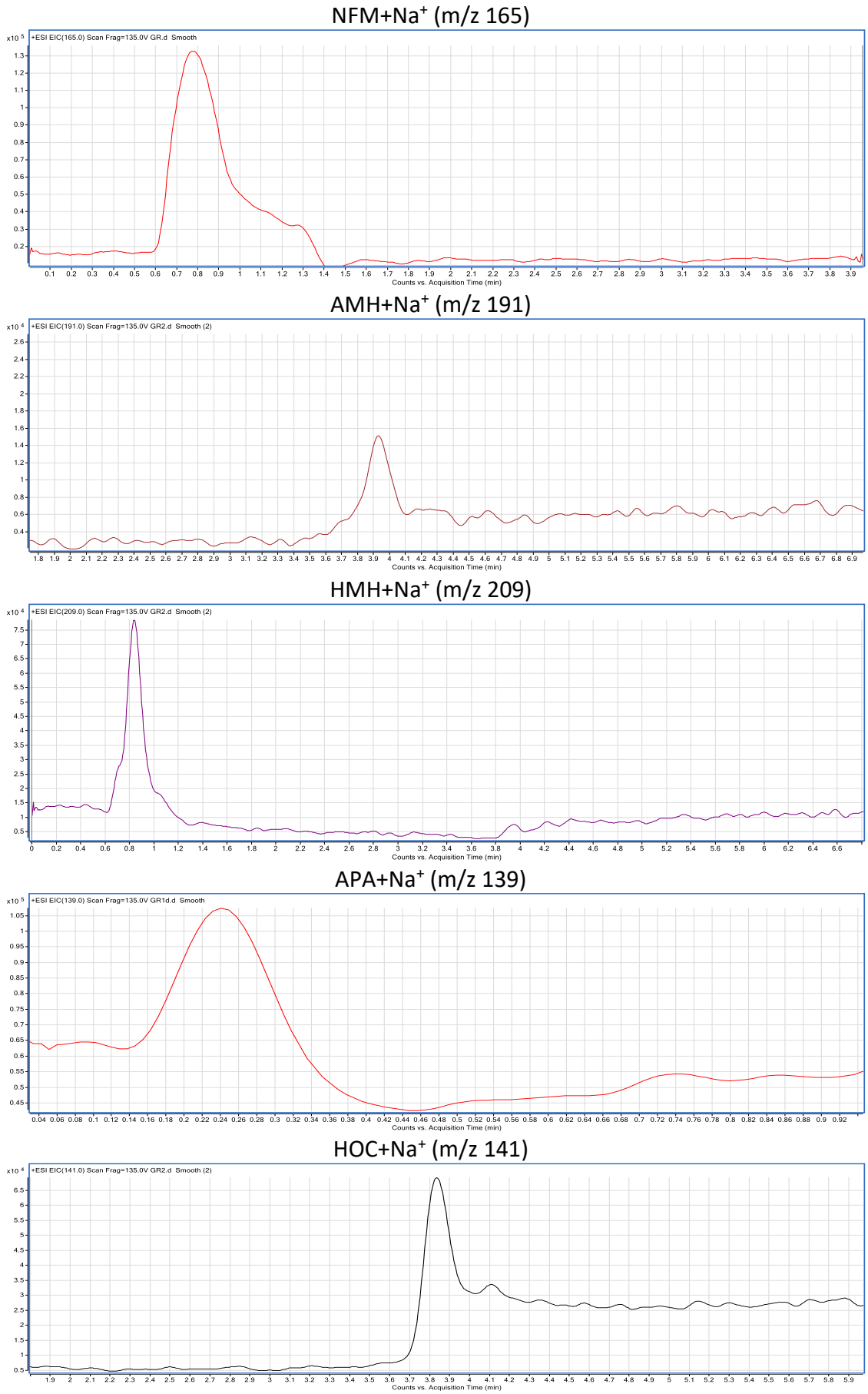

***Figure S6**. MS identification of NFZ degradation products at GR-Ni foam electrode*

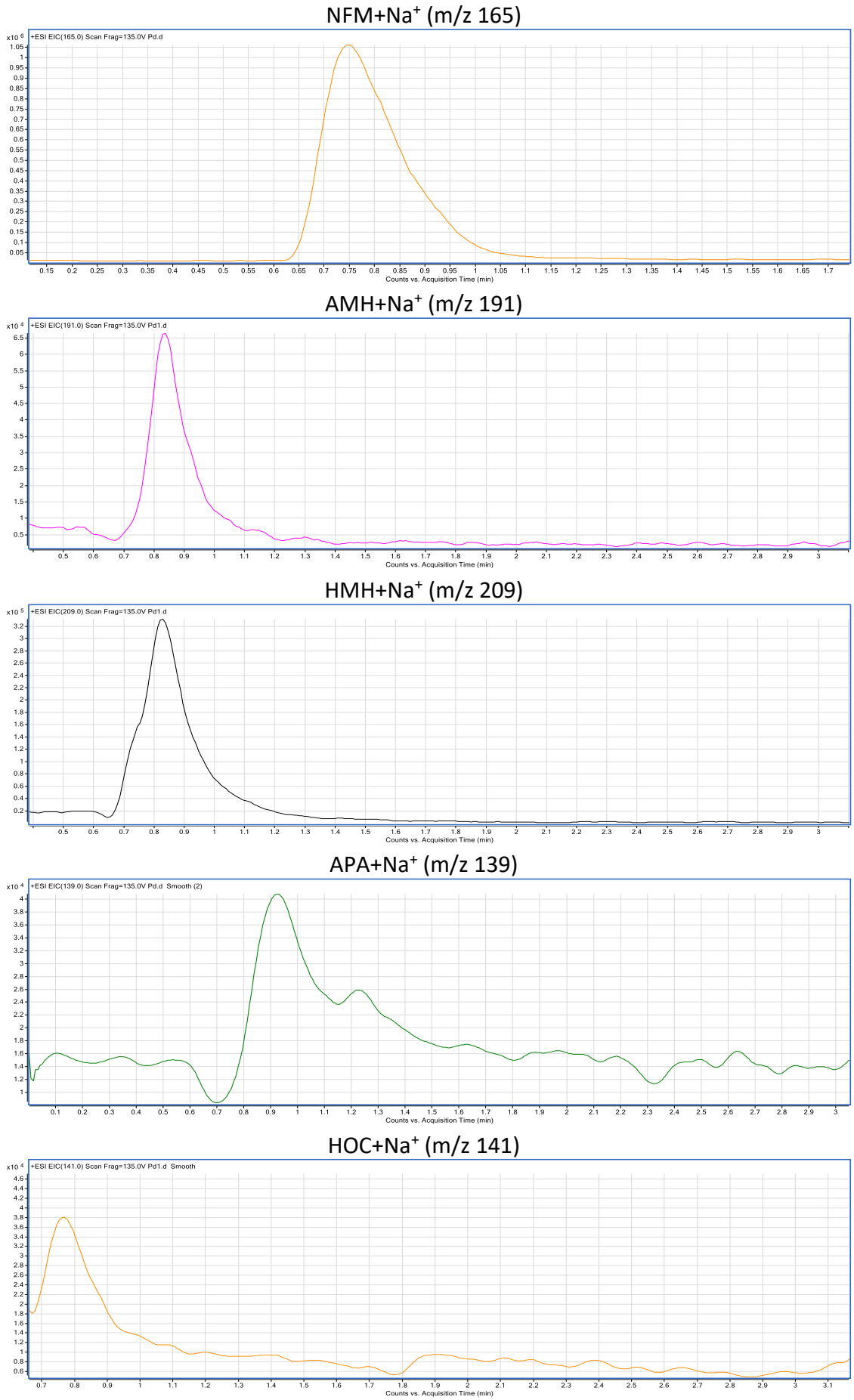

Figure S7 MS identification of NFZ degradation products at Pd-Ni foam electrode.

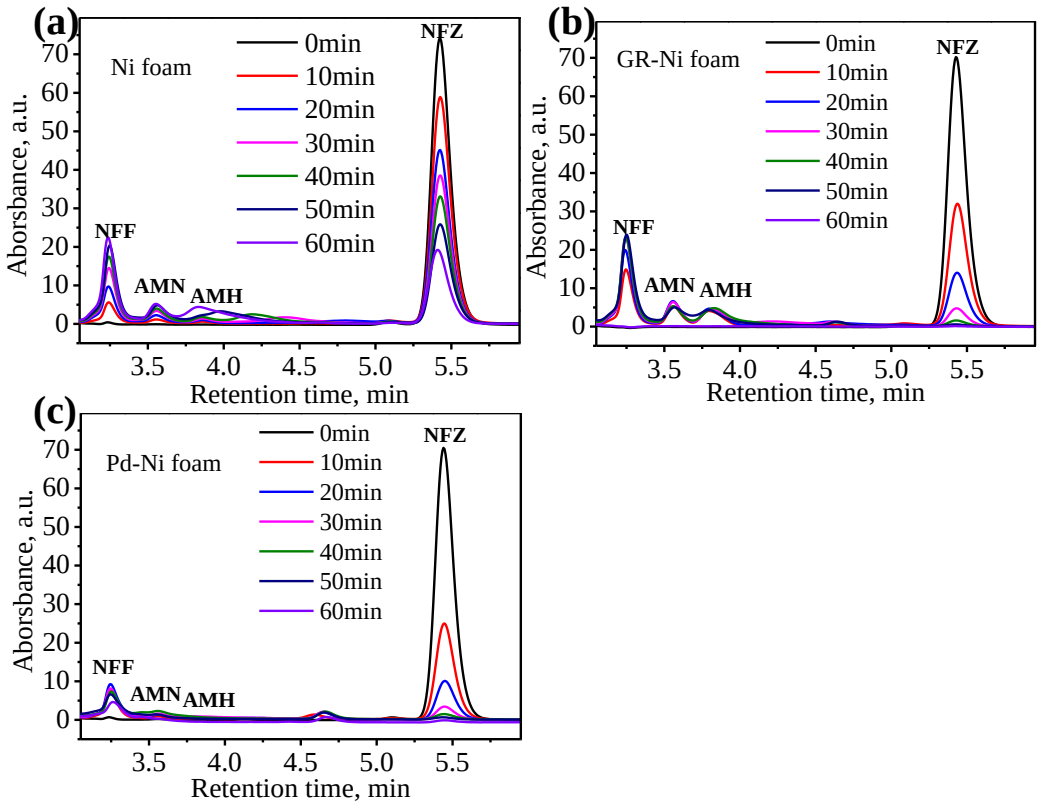

Figure S8. *(A) UV-vis absorbance of electroreductive products of NFZ after different reaction times on* ***(a)*** *Ni foam,* ***(b)*** *GR-Ni foam and* ***(c)*** *Pd-Ni foam*

J. Electrochem. Sci. Eng. **7(4)** (2017) 213-221; DOI: http://dx.doi.org/10.5599/jese.408

Open Access : : ISSN 1847-9286

www.jESE-online.org

Original scientific paper

Benchmarking of electrolyte mass transport in next generation lithium batteries

Jonas Lindberg✉, Henrik Lundgren, Göran Lindbergh, Mårten Behm

Applied Electrochemistry, Department of Chemical Engineering and Technology, School of Chemical Science and Engineering, KTH Royal Institute of Technology, SE-100 44 Stockholm, Sweden

Corresponding authors E-mail: ✉jonasl3@kth.se; Tel.: +46-8-7908171

Received: July 14, 2017; Revised: August 15, 2017; Accepted: August 15, 2017

Abstract

Beyond conductivity and viscosity, little is often known about the mass transport properties of next generation lithium battery electrolytes, thus, making performance estimation uncertain when concentration gradients are present, as conductivity only describes performance in the absence of these gradients. This study experimentally measured the diffusion resistivity, originating from voltage loss due to a concentration gradient, together with the ohmic resistivity, obtained from ionic conductivity measurements, hence, evaluating electrolytes both with and without the presence of concentration gradients. Under galvanostatic conditions, the concentration gradients, of all electrolytes examined, developed quickly and the diffusion resistivity rapidly dominated the ohmic resistivity. The electrolytes investigated consisted of lithium salt in: room temperature ionic liquids (RTIL), RTIL mixed organic carbonates, dimethyl sulfoxide (DMSO), and a conventional Li-ion battery electrolyte. At steady state the RTIL electrolytes displayed a diffusion resistivity ~ 20 times greater than the ohmic resistivity. The DMSO-based electrolyte showed mass transport properties similar to the conventional Li-ion battery electrolyte. In conclusion, the results presented in this study show that the diffusion polarization must be considered in applications where high energy and power density are desired.

Keywords

Li-ion battery; Li-O_2 battery; Room temperature ionic liquid; Diffusion resistivity; Electrolyte mass transport resistivity

Introduction

Lithium-ion batteries are found in nearly all portable electronics, and in technologies still to reach a wider commercial breakthrough such as hybrid, plug-in hybrid, and electric vehicles [1, 2]. In order to reach that breakthrough, batteries that can supply higher power densities are needed.

The maximum power density a battery can deliver is limited by its electrolyte mass transport properties that describe the voltage losses associated with ion transport. These voltage losses (polarizations) cause the battery cell voltage to deviate from its equilibrium, *i.e.* the observed cell voltage is lower than the theoretical value during discharge and higher at charging, resulting in lowered energy efficiency, energy density, and power density of the battery.

Instantly, when a current is applied to the battery, a polarization directly proportional to the current appears, it follows Ohm's law and is thus referred to as ohmic polarization. In the electrolyte, the ohmic polarization is characterized by the ionic conductivity, κ, that measures the conductance in an electrolyte when no concentration gradients are present. Gradually, as current passes, concentration gradients develop in the battery due to the diffusion and migration of the ions (convection, being the third way of ion transport, can be neglected in a battery using a porous separator). Migration is the transport of ions in an electric field. It is described by the transport number, t_+ and t_- for a cation and anion, respectively, describing the relative amount of current carried by each ion. Since cations and anions will have opposing directions of migration, there will be a resistance to mass transport, as electroneutrality cannot be violated, resulting in a polarization. Diffusion is the transport of species against a concentration gradient. It is characterized by the diffusion coefficient, $\tilde{D}$.

As Li-ion and post Li-ion batteries keep developing there is an increase in the number of electrolytes used. The conventional Li-ion battery electrolyte is typically composed of a Li salt, such as lithium bis(trifluoromethulsulfonyl)imide (Li-TFSI) or lithium hexafluorophosphate (Li-PF_6) , and an organic carbonate solvent mixture of for example ethylene carbonate (EC), propylene carbonate (PC), or diethyl carbonate (DEC). These electrolytes are thermodynamically unstable against the negative electrodes and rely on their ability to form stable passivating films (solid electrolyte interfaces) in order to be used [3]. Electrolytes based on room temperature ionic liquids (RTIL) have a wide electrochemical stability window making them stable against a larger number of electrodes compared with conventional Li-ion electrolytes [4]. RTILs are also praised for their high conductivity and safety [5]. These properties also make RTIL-based electrolytes possible candidates for lithium-oxygen (Li-O_2) batteries [6]. More frequently, electrolytes based on dimethyl sulfoxide (DMSO) have been used in Li-O_2 batteries as conventional Li-ion electrolytes have been proven unstable in the presence of O_2 [7].

The distribution of the total polarization of a battery during a hybrid pulse power characterization test on a conventional Li-ion battery with an organic carbonate electrolyte has been investigated [8]. It was found that the electrolyte polarization due to concentration gradients and the electrolyte ohmic polarization contributed to 15 % and 28 % of the total polarization, respectively. This means that 43 % of the total polarization was directly attributed to the electrolyte (remaining sources of polarization was attributed to contract resistance, diffusion in solid phase, ohmic resistance in solid phase, and activation overpotential). Furthermore, when enough time had passed for the concentration gradient in the electrolyte to reach a steady state its contribution to the polarization was larger than that of the ohmic polarization [9]. To fully describe the time-dependent mass transport, and its associated polarizations, in a non-dilute and non-ideal electrolyte a model based on concentrated electrolyte theory needs to be set up, and the parameters therein, such as diffusion

coefficients, transport numbers, and thermodynamic factors need to be determined, in addition to the conductivity. The full set of those mass transport parameters has been determined for some electrolytes [9-14], but since the methods for such comprehensive characterizations are still quite complex and time consuming there is also a need for quick benchmarking methods that yield relevant performance metrics.

Little is known about the mass transport in DMSO-based electrolytes. For RTILs the most common electrolyte performance parameter found in the literature today is conductivity [15], although transport numbers have been determined [16], as well as self-diffusion coefficients obtained by NMR [17]. A problem with using parameters such as the above-mentioned ones for benchmarking is that they are intimately linked to the model that was used to define them. One consequence of this is that it makes it difficult to compare parameters for different types of electrolytes, for example a binary liquid electrolyte, a polymer gel electrolyte and an RTIL. A further problem is that the parameters do not give direct information about the magnitude of electrolyte polarization for a certain current density, *i.e.* the translation of diffusion coefficients and transport numbers into overpotential is not straightforward. A way of benchmarking electrolytes that meet these requirements was suggested by Nyman *et al.* [9] by introducing the concept of electrolyte mass transport resistivity (EMTR)[1]

Aim

The purpose of this study is twofold: (I) to demonstrate the usefulness of electrolyte mass transport resistivity (EMTR) as a method for benchmarking electrolyte mass transport limitations and (II) to highlight the essential lithium battery electrolyte properties by a direct comparison of a set of candidate electrolytes for the next generation of Li batteries. This is done by measuring the EMTR of electrolytes based on RTILs, organic carbonates, a mixture of RTIL and organic carbonates, and DMSO. Little is known about the diffusive mass transport in RTIL and DMSO based electrolytes beyond conductivity, thus, making the use of conductivity as the sole figure of merit potentially misleading. Therefore, the use of a method including concentration gradient polarization is well motivated. For all electrolytes, the time dependence of the electrolyte polarization was also examined.

Theory - electrolyte mass transport resistivity

Electrolyte mass transport resistivity (EMTR) was initially used as a figure of merit, to quantify polarizations with and without concentration gradients, for interpretation of results from full mass transport characterizations based on concentrated electrolyte theory [9,13,18]. It has been experimentally used alongside other techniques to evaluate the influence of flame retardants in Li-ion battery electrolytes [19].

The definition of the EMTR is shown in Eq. 1, where it is expressed in terms of the parameters in the concentrated electrolyte model [9]. However, it was also suggested that it could be determined experimentally in a relatively simple way, by rewriting Eq. 1 in the form of Eq. 2, where the variables only depend on the experimentally measurable quantities conductivity and diffusion potential at steady state.

$$-\frac{\left(\partial \Phi / \partial x\right)}{i} = \frac{1}{\kappa} + \frac{2RT}{F^2 c_{\text{salt}}} \frac{c_{\text{solvent}}}{c_{\text{tot}}} \frac{\left(1 - t_+^{\text{solvent}}\right)^2}{} \tag{1}$$

[1] In Nyman *et al.* it was called normalized potential gradient.

$$-\frac{\left(\partial \Phi / \partial x\right)_{s.s}}{i} = \frac{1}{\kappa} + \frac{\Delta \Phi_{diff,s.s.} \epsilon^{\beta}}{F^2 c_{salt}} \frac{1}{i} \quad (2)$$

In these equations Φ is the electrolyte potential[2], i the current density, κ the conductivity, t_+ the cationic transport number with respect to the solvent and $\tilde{D}$ the diffusion coefficient with respect to the thermodynamic driving force. $\Delta\Phi_{\text{diff,s.s.}}$ is the potential drop caused by concentration gradients at steady state in a cell of length *l*. The influence of the porosity and tortuosity of the separator is taken into account by multiplying with the porosity, ϵ, raised to the power of the Bruggeman constant β. The first term on the right hand side of Eq. 2 is the ohmic resistivity, the second term is called the diffusion resistivity[3]. Note that when Eq. 1 is rewritten as Eq. 2 there is no longer a model dependence and Eq. 2 can therefore be used to describe any electrolyte. Further, the method is not limited to dilute and/or binary electrolytes.

The diffusion polarization can be obtained in a relatively simple galvanostatic polarization experiment, and the conductivity is easily obtained by standard methods. By measuring both ohmic and diffusion resistivities the relative contribution of these two sources to the full steady-state electrolyte polarization is obtained. Another way of understanding the EMTR is that multiplied with a given current density it represents the corresponding electrolyte polarization in the electrolyte at steady state.

Experimental

Materials

The salt used was Li-bis(trifluoromethanesulfonyl)imide (Li-TFSI, Sigma-Aldrich 99.95 % purity). The solvents used were dimethyl sulfoxide (DMSO, SigmaAldrich, Anhydrous), N-ethyl-N-methyl-imidazoleum-TFSI (EMI-TFSI, Solvionic, 99.9 % purity), N-propyl-N-methyl-pyrrolidinium-TFSI (Pyr13-TFSI, Solvionic, 99.9 % purity) and N-propyl-N-methyl-piperidinium-TFSI (Pip13-TFSI, Solvionic, 99.9 % purity). The organic carbonate electrolyte consisted of Li-TFSI salt in ethylene carbonate:diethyl carbonate (EC:DEC) with a 1:1 weight ratio (Novolyte, battery grade). All chemicals were used as received. All RTIL electrolytes contained 1.0 M Li-TFSI, for the DMSO and EC:DEC electrolytes the Li-TFSI content was also varied. The experiments were conducted at 25° C in an argon-filled glove box.

Ohmic resistivity experiment

The conductivities were measured using a Consort K912 conductometer with a SK21T micro-electrode probe. The conductometer was calibrated outside of the glove box using potassium chloride standard solutions. The ohmic resistivity was then calculated by using the first term on the right-hand side of eq. 2.

Diffusion resistivity experiment

In order to determine the diffusion resistivity a symmetrical test cell with two Li-metal electrodes was assembled. To ensure a constant inter-electrode distance the electrodes were separated by a Teflon spacer-ring with a thickness of 500 μm and an inner diameter of 6 mm. The electrolyte was

[2] The electrolyte potential is defined and measured with a metal reference electrode of the same kind as the cation. The EMTR is therefore also defined for that species.

[3] Note that this term describes both migration and diffusion, it contains both t_+ and $\tilde{D}$, and both these modes of transport will give rise to concentration gradients. The term "diffusion resistivity" is simply chosen to agree with previously used terminology.

soaked into a Whatman GF/A glass micro fiber filter, placed inside the spacer-ring. The filter has a porosity of 0.9, and the Bruggeman coefficient has previously been determined to 3.44 [9].

The diffusion potential ($\Delta\Phi_{\text{diff}}$ in Eq. 2) was measured in the test cell directly after a galvanostatic polarization. A schematic of the experimental raw data is seen in Figure 1. The evolution of the diffusion potential with polarization time could be followed by measuring the potential during current interrupts which were very short in relation to the time scale of the total polarization. Typically, a galvanostatic current was applied for several minutes followed by a two seconds interrupt. When the measured diffusion potential no longer showed any change with polarization time the electrolyte concentration gradients was assumed to be at steady state. The steady state diffusion potential was inserted into the second term on the right-hand side of Equation 2 in order to calculate the diffusion resistivity. The magnitude of the polarization current was chosen so that the potential directly after current switch-off was between 5 and 50 mV. The lower potential limit was chosen to give low noise contribution, and the upper limit was set to avoid dendrite formation. Each electrolyte composition was tested in at least four test cells and each cell was polarized with at least four different currents giving potential drops at steady state spanning over 5 to 50 mV.

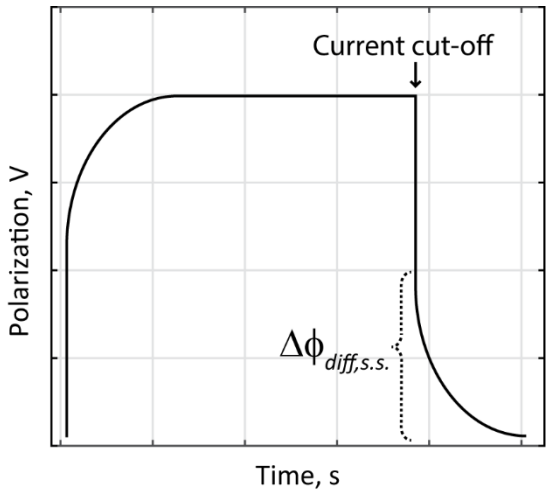

Figure 1. *Schematic of the galvanostatic polarization experiment raw data. At the start of the experiment a constant current is applied. When steady state is reached the current is turned off, the potential remaining at this point is caused by the concentration gradients in the electrolyte and corresponds to the diffusion potential, . $\Delta\Phi_{diff}$ This value is used in Equation 2 in order to calculate the diffusion resistivity*

The measurements turned out to be sensitive to the surface of the Li foil, giving less spread in results when pristine Li foil was used. Due to thermodynamic instability between the electrolyte and the Li-metal electrodes, there might be mixed potential between the solvent reduction and the lithium oxidation, thus affecting the measured potential. Since the mixed potential would be solvent dependent its influence would differ from solvent to solvent. However, if the concentration gradients was allowed to fully relax after the galvanostatic polarization the potential difference between the two Li electrodes were in the order of μV for all electrolytes in this study, thus, indicating that the there was no significant influence of a mixed potential in this study.

Results and discussion

By measuring the diffusion polarization at steady state, $\Delta\Phi_{\text{diff}}$ in a galvanostatic current-interrupt experiment and the conductivity, κ, using a conductivity meter, the diffusion and ohmic resistivity

was calculated for each electrolyte according to Equation 2. The calculated resistivities for the electrolytes examined at concentrations of 1 M Li-TFSI are seen in Table 1.

***Table 1**. The mean ohmic and diffusion resistivity of the various electrolytes tested containing 1 M Li-TFSI. The diffusion resistivities are reported with their standard deviations that show that there was a variation of the measured diffusion resistivity between cells (variation between consecutive experiments in the same cell was smaller)*

	Ohmic resistivity, Ω m	Diffusion resistivity, Ω m
EC:DEC	1.5	3.0±0.8
DMSO	1.0	4.6±1.6
EMI-TFSI	3	91±9
Pyr13-TFSI	10	220±10
Pip13-TFSI	31	590±50

All electrolytes show a clear difference in the magnitude between ohmic and diffusion resistivity with diffusion resistivity being larger in all cases. Specifically, in the electrolytes based on RTILs the total polarization was dominated by the diffusion resistivity, whereas for EC:DEC and DMSO both ohmic and diffusion resistivity contributed more equally. For example, comparing EMI-TFSI with EC:DEC the ohmic resistivity was twice as high and the diffusion resistivity was ≈30 times as high for EMI-TFSI, thus stressing the importance of evaluating the diffusion resistivity alongside with ohmic resistivity. Organic solvents and RTILs are miscible; it is therefore possible to create RTIL-organic mixed electrolytes that combine the RTIL safety features with the lower viscosity of carbonate solvents. Figure 2 displays the two right-hand side terms of Eq. 2 separately for electrolytes consisting of 1 M Li-TFSI with varying amount of EMI-TFSI and EC:DEC in the solvent. Both the ohmic and the diffusion resistivity increased with EMI-TFSI content, with the diffusion resistivity being far greater in magnitude at high EMI-TFSI content.

Electrolytes based on EC:DEC and DMSO showed similar ohmic and diffusion resistivity. This shows that DMSO is a suitable electrolyte for Li-O_2 batteries from a mass transport perspective, however, how suitable DMSO is regarding other factors is still debatable.

Both EC:DEC and DMSO electrolytes were tested at several Li-TFSI concentrations, see Figure 3. The lowest EMTR was observed at concentrations above 0.5 M Li-TFSI. Lower concentrations resulted in higher ohmic and diffusion resistivities. The spread in measurements was also larger at lower concentration. A resistivity vs. concentration graph was produced by Nyman et al. from a full characterization of $LiPF_6$ in 3:7 EC:EMC [9] displaying similar results, although the diffusion resistivity is higher in the present study, which might be due to a larger anion inhibiting mass transport. This confirms that the method applied here provides results equivalent to those obtained from complex full characterizations based on physical models.

A reason that the RTILs showed large EMTR may be found by looking at the constituents of the RTIL electrolytes. In the RTILs in this study there are three ionic species present: Li^+, TFSI and a bulky cation (EMI, Pyr13 or Pip13). For 1 M Li-TFSI in EMI-TFSI the coordination number is a little bit lower than two [20] suggesting that the predominant coordination complex is $[Li(TFSI)_2]^-$.

This would change the effective charge of the current-carrying specie from positive to negative *i.e.* changing the migration direction of Li, thus making diffusion the only means of transport carrying Li to the cathode. As the RTIL content increases in a mixed electrolyte, so does the viscosity [5].

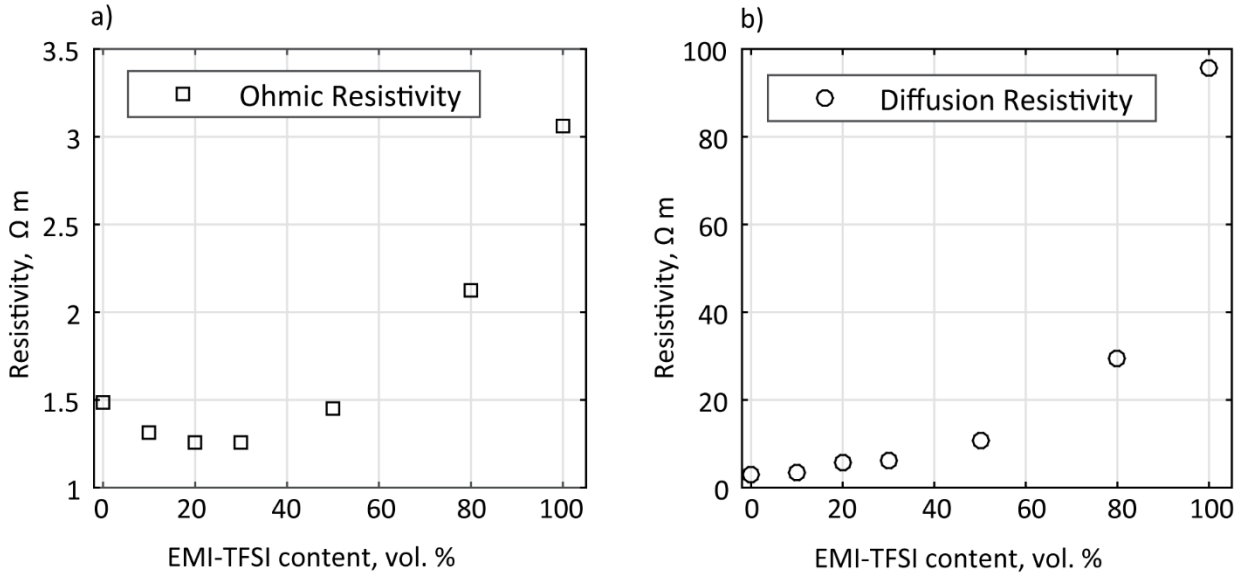

***Figure 2**. The effect on ohmic* (□) *and diffusion* (∘) *resistivity when EMI-TFSI was added to EC:DEC are shown in **(a)** and **(b)**, respectively. All electrolytes contained 1 M Li-TFSI*

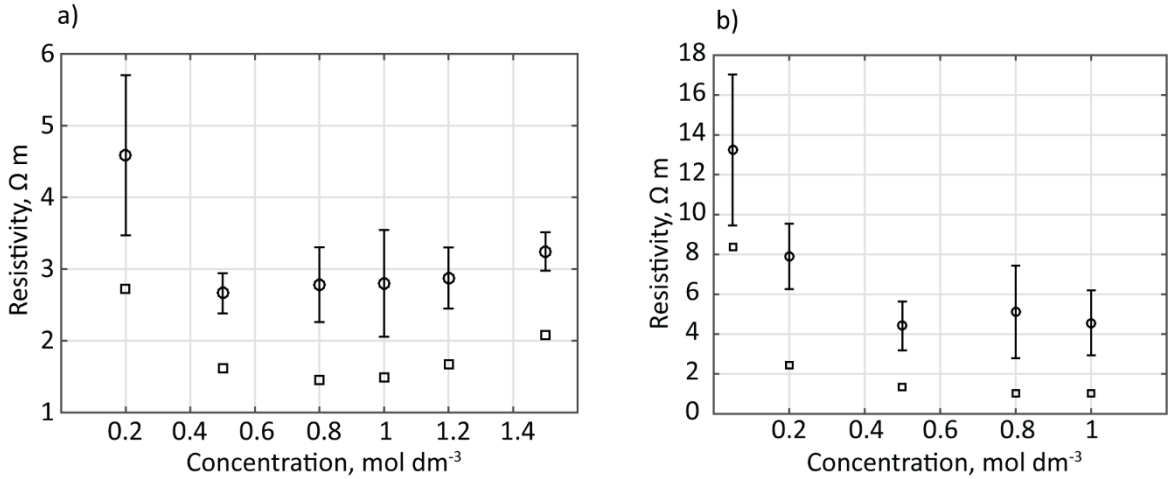

***Figure 3.** The diffusion* (∘) *and ohmic* (□) *resistivity at different LiTFSI concentrations in **(a)** EC:DEC and **(b)** DMSO measured at steady-state. The error bars show standard deviations*

However, explaining the variation in mass transport properties in terms of change in viscosity is not suitable since viscosity should affect the ohmic and diffusion resistivities equally and the results do not show this (see Figure 2). An alternative explanation could be found if looking at the system in a molecular perspective. When DEC is the only solvent present the Li ion coordinates to DEC in a $[Li(DEC)_3]^+$ complex [21]. In a mixed EC:EMI-TFSI solvent the predominant solvation complex of Li^+ is $[Li(EC)_4]^+$ down to a Li:EC molar ratio of 1:4 [22,23]. At an EMI-TFSI content higher than 50 vol.% in EC:DEC there is not enough EC and DEC to fully solvate all Li ions. When the EMI-TFSI content is increased there is a steep rise in diffusion resistivity suggesting that the solvation of the Li ions is of key importance, see Figure 2. RTILs have promising safety features and addition of RTILs to organic solvents increases safety. An addition of 40 - 60 vol.% EMI-TFSI to 1 M $LiPF_6$ in EC:DEC has been suggested as an optimal composition with no flammability, high conductivity and low viscosity [5]. However, this study shows that at 50 vol.% EMI-TFSI there is a fourfold increase in diffusion resistivity compared to when no RTIL was present.

The time needed for the diffusion polarization to reach a steady state depends on the inter-electrode distance, electrolyte, and the polarization current. In the galvanostatic polarization

experiment, currents varying by one order of magnitude was needed in order to get diffusion polarizations within the desired range of 5 to 50 mV. Therefore, the time needed to reach steady state also varied by one order of magnitude with larger currents needing more time. The diffusion polarization for the electrolytes based on EC:DEC and DMSO typically reached steady state within 10 to 20 minutes for polarizations of 10 mV, see Figure 4a. For the RTILs this time was typically 4 to 20 hours, see Figure 4b. Keep in mind that the test cell had an electrode distance of 500 µm and that if the electrode distance were to be reduced one order of magnitude, to better agree with a real battery, then the time would be reduced by two orders of magnitude (according to Fick's second law). This would correspond to 2-12 min for the electrolytes based on the RTILs and 6-12 seconds for those based on EC:DEC and DMSO. Further, the time needed for the diffusion resistivity to equal the ohmic resistivity would be typically five seconds for the RTIL based electrolytes and 1-2 seconds for the electrolytes based on EC:DEC and DMSO. This indicates that losses due to concentration gradients in a Li battery must be considered in most usage scenarios where energy efficiency and power density is important.

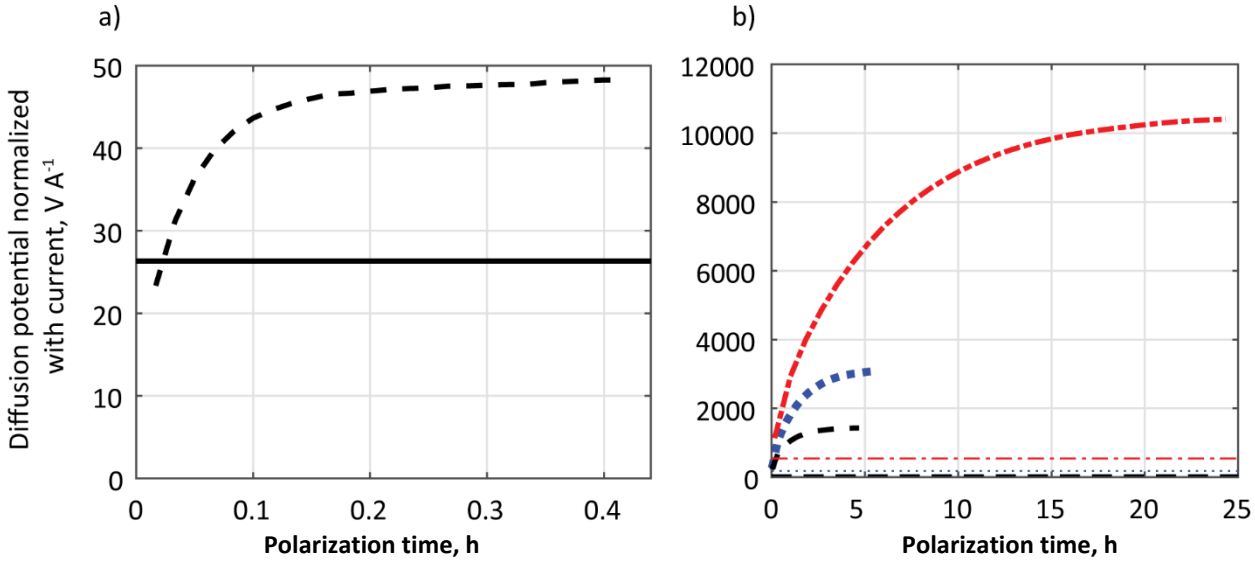

Figure 4. (a) *The diffusion potential (-) for 1 M LiTFSI in EC:DEC shown as a function of time. The current normalized ohmic potential is shown as a time-independent horizontal line.*
(b) *The current-normalized diffusion potentials of EMI-TFSI (–, black), Pyr13-TFSI (·, blue) and Pip13-TFSI (·–, red). The current-normalized ohmic potentials are shown as time-independent horizontal lines, EMI-TFSI (–, black), Pyr13-TFSI (·, blue) and Pip13-TFSI (·–, red). All electrolytes contained 1 M Li-TFSI*

Conclusions

In this study, both ohmic and diffusion voltage losses, presented as resistivities, were measured in a quick and convenient way to examine the mass transport in next generation Li-battery electrolytes. The results highlight the importance of quantifying the diffusion together with the ohmic polarization when trying to estimate the total electrolyte polarization.

When a conventional Li-ion battery electrolyte was examined the results showed good agreement with ohmic and diffusion resistivities from a full characterization based on a physical model, thus, validating the method used in this study. Electrolytes based on dimethyl sulfoxide (DMSO) showed mass transport resistivities similar to those of the conventional Li-ion electrolyte, making the DMSO based electrolytes suitable for use in Li-O_2 batteries from a mass transport perspective. When examining electrolytes based on room temperature ionic liquids (RTIL) the mass transport resistivities were 25-130. The diffusion resistivity at steady-state was ~ 20 times greater

than the ohmic resistivity for 1 M Li-TFSI in the RTILs tested. This ratio was only about two for conventional Li-ion battery electrolytes. For all the electrolytes examined, the concentration gradients developed quickly enough for the diffusion resistivity to become larger than the ohmic resistivity in short time. When a mixture of RTIL and organic carbonates was used as solvent the diffusion resistivity was larger than when pure organic carbonates were used. Adding more than 50 vol.% RTIL drastically increased the diffusion resistivity.

As concluding remarks, it can be said that the method employed here, measuring both the ohmic and diffusion resistivity, offers insight to the mass transport of a group of compounds where previously little has been known beyond conductivity and viscosity.

***Acknowledgements**: Financial support from The Swedish Foundation for Strategic Research (SSF) and The Swedish Electromobility Centre is gratefully acknowledged.*

References

[1] E. J. Cairns, P. Albertus, *Annual Review of Chemical and Biomolecular Engineering* **1** (2010) 299-320
[2] I. A. Fulton, Renewable *and Sustainable Energy Reviews* **68** (2017) 685-692
[3] P. Verma, P. Maire, P. Novák, *Electrochimica Acta* **55** (2010) 6332-6341
[4] M. Galinski, A. Lewandowski, I. Stepniak, *Electrochimica Acta* **51** (2006) 5567-5580
[5] A. Guerfi, M. Dontigny, P. Charest, M. Petitclerc, M. Lagace, A. Vijh, K. Zaghib, *Journal of Power Sources* **195** (2010) 845-852
[6] C. J. Allen, S Mukerjee, E. J. Plichta, M. A. Hendrickson, K. M. Abraham, *Journal of Physical Chemistry Letters* **2** (2011) 2420-2424
[7] S. A. Freunberger, Y. Chen, Z. Peng, J. M. Gri, L. J. Hardwick, F. Barde, P. Novak, P. G. Bruce, *Journal of the American Chemical Society* **133** (2011) 8040-8047
[8] A. Nyman, T. G. Zavalis, R. Elger, M. Behm, G. Lindbergh, *Journal of the Electrochemical Society* **157** (2010) A1236-A1246
[9] A. Nyman, M. Behm, G. Lindbergh, *Electrochimica Acta* **53** (2008) 6356-6365
[10] L. O. Valoen, J. N. Reimers, *Journal of the Electrochemical Society* **152** (2005) A882-A891
[11] Y. P. Ma, M. Doyle, T. F. Fuller, M. M. Doeff, L. C. Dejonghe, J. Newman, *Journal of the Electrochemical Society* **142** (1995) 1859-1868
[12] P. Georen, G. Lindbergh, *Electrochimica Acta* **47** (2001) 577-587
[13] H. Lundgren, J. Scheers, M. Behm, G. Lindbergh, *Journal of The Electrochemical Society* **162** (2015) A1334-A1340
[14] A. Ehrl, J. Landesfeind, W. A. Wall, H. A. Gasteiger, *Journal of The Electrochemical Society* **154** (2017) A826-A836
[15] B. Garcia, S. Lavallee, G. Perron, C. Michot, M. Armand, *Electrochimica Acta* **49** (2004) 4583-4588
[16] J. K. Kim, L. Niedzicki, J. Scheers, C. R. Shin, D. H. Lim, W. Wieczorek, P. Johansson, J. H. Ahn, A. Matic, P. Jacobsson, *Journal of Power Sources* **224** (2013) 93-98
[17] A. Noda, K. Hayamizu, M. Watanabe, *Journal of Physical Chemistry B* **105** (2001) 4603-4610
[18] H. Lundgren, M. Behm, G. Lindbergh, *Journal of The Electrochemical Society* **162** (2015) A413-A420
[19] K. Ciosek Hogstrom, H. Lundgren, S. Wilken, T. G. Zavalis, M. Behm, K. Edstrom, P. Jacobsson, P. Johansson, G. Lindbergh, *Journal of Power Sources* **256** (2014) 430-439
[20] J. C. Lassegues, J. Grondin, C. Aupetit, P. Johansson, *Journal of Physical Chemistry A* **113** (2009) 305-314
[21] M. Datt Bhatt, M. Cho, K. Cho, *Canadian Journal of Chemistry-Revue Canadienne De Chimie* **89** (2011) 1525-1532
[22] J. C. Lassegues, J. Grondin, D. Talaga, *Physical Chemistry Chemical Physics* **8** (2006) 5629-5632
[23] L. J. Hardwick, M. Holzapfel, A. Wokaun, P. Novak, *Journal of Raman Spectroscopy* **38** (2007) 110-112

J. Electrochem. Sci. Eng. **7(4)** (2017) 223-235; DOI: http://dx.doi.org/10.5599/jese.413

Open Access : : ISSN 1847-9286

www.jESE-online.org

Original scientific paper

Large scale model predictions on the effect of GDL thermal conductivity and porosity on PEM fuel cell performance

Obaid Ur Rehman[1,✉], Amber Fishan Zafar[2]

[1]*Chemical Engineering Department, University of Karachi, Karachi, Pakistan*
[2]*Automotive and Marine Engineering Department, NED University of Engineering & Technology, Karachi, Pakistan*

Corresponding authors E-mail: ✉orehman@uok.edu.pk; Tel. +92-321-2536798

Received: July 25, 2017; Revised: September 24, 2017; Accepted: September 25, 2017

Abstract

The performance of proton exchange membrane (PEM) fuel cell majorly relies on properties of gas diffusion layer (GDL) which supports heat and mass transfer across the membrane electrode assembly. A novel approach is adopted in this work to analyze the activity of GDL during fuel cell operation on a large-scale model. The model with mesh size of 1.3 million computational cells for 50 cm^2 active area was simulated by parallel computing technique via computer cluster. Grid independence study showed less than 5% deviation in criterion parameter as mesh size was increased to 1.8 million cells. Good approximation was achieved as model was validated with the experimental data for Pt loading of 1 mg cm^{-2}. The results showed that GDL with higher thermal conductivity prevented PEM from drying and led to improved protonic conduction. GDL with higher porosity enhanced the reaction but resulted in low output voltage which demonstrated the effect of contact resistance. In addition, reduced porosity under the rib regions was significant which resulted in lower gas diffusion and heat and water accumulation.

Keywords

Computational fluid dynamics; Parallel computing; Experimental validation

Introduction

The impact of immense utilization of fossil fuels in the automotive and power generation sector has drawn enormous damage on environment. The development of renewable and clean energy resources has been a key topic of researchers in past few decades. Among other energy conversion devices fuel cells have been widely recognized as a promising clean energy resource due to their high energy density and conversion efficiency [1,2]. PEMFC has emerged as a substitute for internal combustion engines in automotive sector as it requires low operating temperatures and offers quick

startup. Though yet the fuel cells have not been fully commercialized due to high manufacturing cost and lack of infrastructure for hydrogen storage and its utilization, but still it has a great potential to replace conventional energy conversion systems.

The main components of PEMFC are represented in Figure 1. Air is injected from cathode side of the cell while hydrogen gas from anode. At the surface of anode side catalyst layer (CL), hydrogen oxidation reaction (HOR) occurs as shown in the reactions below. Simultaneously, the oxygen reduction reaction (ORR) occurs at the cathode side CL. The hydrogen ions (protons) from anode travel through the PEM and reach the cathode catalyst where they react with oxygen to produce water. Product heat is released as the reaction is exothermic.

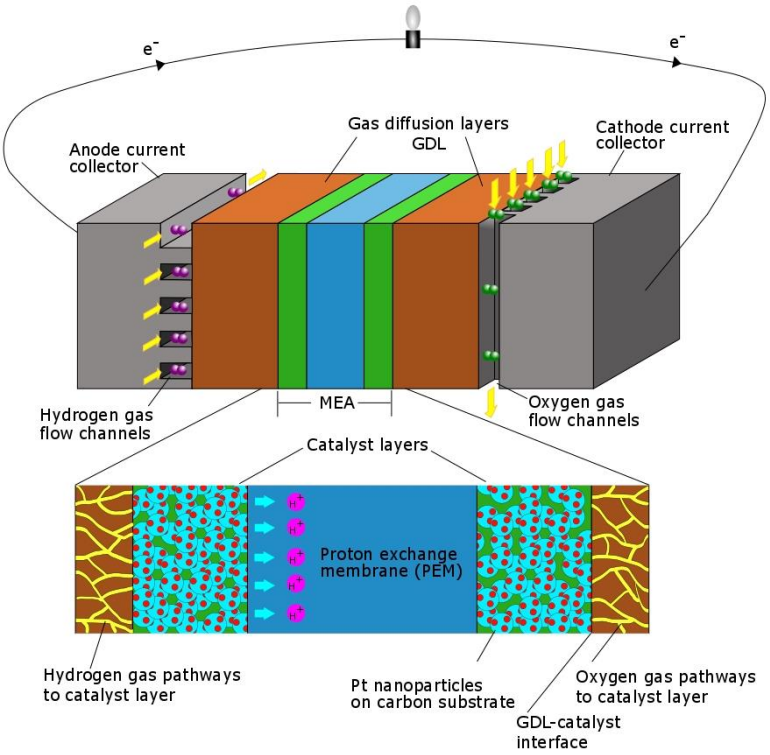

Figure 1. *Schematic of PEM fuel cell*

The performance of PEMFC is highly dependent upon the thermal and transport characteristics of the porous CL and GDL [3]. GDLs are employed for distribution of reactant gases to the reaction sites of the catalysts which increase the diffusion capacity and enhance reaction rate. They also provide the pathway for removal of water and heat from CL to gas flow channels which in turn limit the concentration overpotential. To achieve high current densities, the GDL must be porous and allow for the flow of both water and reactant gases. It must also be thermally and electrically conductive for the flow of product heat and electric current in both in-plane and through plane directions[4]. Water droplets form at low operating temperature in fuel cell which block pores of GDL and reduce gas diffusivity and number of reaction sites at CL [5]. On the other hand, high water content (H_2O/SO^{-3} ratio or λ) in PEM promotes proton conductivity [6]. This trade-off between water content and reaction rate should be taken into consideration for an efficient operation of PEMFC. Favorable characteristics of GDL and CL are required for improved gas diffusivity and thermal management in the cell. Various studies have been done experimentally to analyze the physical and thermal effects of GDLs on PEMFC performance [7-10].

When compared with the experimental procedures numerical simulation provides relatively agile methods to design and analyze complex systems and it also offers access to diversified results. Currently various numerical models of PEMFC are available in the published literature covering the

transport phenomena and electrochemical kinetics [11-21]. To analyze the performance of PEMFC at different operating conditions and design configurations various simulations have been produced but very few provide analysis of full GDL on large-scale model.

Zhang *et al.* [22] investigated the effect of porosity of cathode side GDL on catalyst potential distribution and pressure drop along flow channels. They noticed that at porosity of 0.6 the potential was maximal but as the value of porosity was increased potential dropped, which indicated that the contact resistance impeded the transfer of current through GDL.

Inamuddin *et al.* [23] studied a single channel, three dimensional model of PEMFC to evaluate its performance at different GDL porosities and thickness. They noticed a gradual increase in current density with GDL porosity. However, performance at porosity greater than 0.7 was not estimated which may indicate its limiting value.

Khazaee *et al.* [24] developed a three dimensional model to investigate the effect GDL and membrane characteristics on performance of annular PEMFC. Their results suggested that high GDL porosity was not favorable at high current densities as it led to increased contact resistance. They also suggested high thermal conductivity of GDL to prevent PEM from drying.

Alhazmi *et al.* [25] developed a 11-channel, three dimensional model to estimate the performance of PEMFC at different in-plane and through plane GDL thermal conductivities. Improved power density was observed for high GDL thermal conductivities which corresponded to low PEM temperature. Low temperature operations were favorable for low electrical and protonic resistance in GDL and PEM respectively.

Fadzillah, Nee and Rosli [26] simulated a two dimensional model to investigate the distribution of oxygen on cathode side GDLs with different porosities and thicknesses. It was observed that porosity of GDL played a key role to facilitate the reactant to reach more reaction sites which resulted in improved PEMFC performance.

Maslan *et al.* [27] developed a three dimensional single channel model to predict the performance of PEMFC with respect to GDL properties. Effect of porosity and PTFE content of GDL was analyzed. Their results showed that at low porosity the concentration overpotential dominated the PEMFC performance because the water droplets were trapped in GDL pores which resulted in reduced reaction sites.

In this paper a simulation work is presented for a full cell model using commercial code of ANSYS FLUENT® with parallel computing technique. Effects of GDL thermal conductivity and porosity on PEMFC performance were investigated. Cell performance was analyzed with relation to water content and temperature across PEM. Oxygen concentration and reaction heat production at GDL-catalyst interface was also examined to observe the impact of GDL porosity.

Model description

The governing transport phenomena and reaction kinetics of PEMFC has been modelled in numerous works. Some good reviews on the model of PEMFC can be found in [28] and [29]. The geometrical and mathematical models are described in subsequent paragraphs.

Geometric model

The full cell geometry with 50 cm^2 of active area and 45-channel serpentine flow design was developed using GAMBIT pre-processor. The model consists of seven layers as shown by the schematic in Figure 1. The geometry was meshed by hexahedral scheme as shown in Figure 2. The whole geometry comprised approximately 1.3 million computational cells. The photograph of the flow channels is presented in Figure 3. The geometrical dimensions are presented in Table 1.

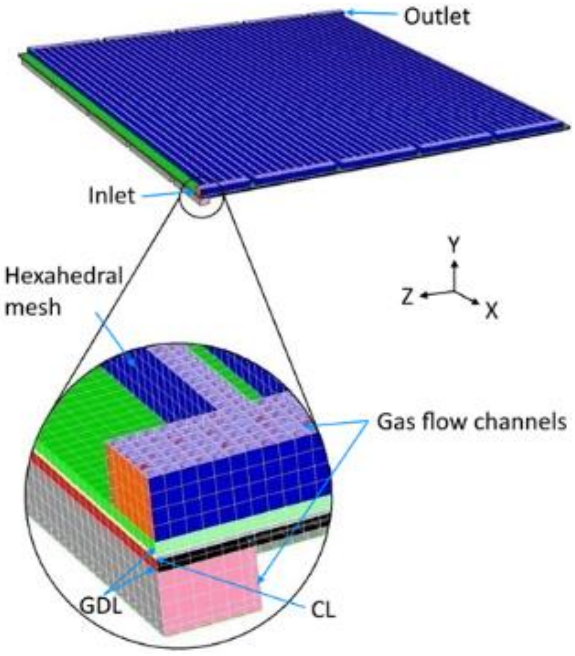

Figure 2. *Meshed geometry of PEMFC*

Figure 3. *Engraved serpentine gas flow channels in bipolar plate*

Table 1. *Model physical properties*

Dimension	Length, mm
Channel height	1
Channel length	70
Channel width	0.75
Rib width	0.82
GDL thickness	0.19
Catalyst layer thickness	0.01
Membrane thickness	0.0508
Current collector thickness	0.25

Mathematical model - governing equations

A multiphase mathematical model was employed in present work. The main reaction at cathode side takes place at triple phase boundary. Hydrogen ions formed at anode CL travel to cathode CL through PEM where they are combined with oxygen gas to form water.

Conservation equations

In a finite volume method the basic equation for a conservation of a general property φ over a control volume in a steady state problem is given as [30].

$$\int_A n(\rho\varphi u)\mathrm{d}A = \int_A n(\Gamma\nabla\varphi)\mathrm{d}A + \int_{CV} S_V \mathrm{d}V \quad (1)$$

where n represents the vector normal to a differential surface dA and Γ is a diffusion coefficient. The left-hand side gives the convective flux and right-hand side gives the diffusive flux plus the generation or consumption of the property.

The continuity equation for the model is given as

$$\frac{\partial(\rho\varepsilon)}{\partial t} + \nabla\cdot(\varepsilon\rho\vec{u}) = S_\mathrm{m} \quad (2)$$

where ρ is the density, ε is the porosity, $\vec{u}$ is the fluid velocity vector and S_m denotes the mass production term.

The momentum conservation equation is given as follows

$$\frac{\partial(\rho\varepsilon\vec{u})}{\partial t}+\nabla\cdot(\varepsilon\rho\vec{u}\vec{u})=-\varepsilon\nabla p+\nabla\cdot(\varepsilon\mu\nabla\vec{u})+S_{\mathrm{u}} \tag{3}$$

where p represents the pressure, and S_{u} is the force per unit volume.

For the species conservation following equation is employed

$$\frac{\partial(\varepsilon C_{\mathrm{k}})}{\partial t}+\nabla\cdot(\varepsilon\rho\vec{u}C_{\mathrm{k}})=\nabla\cdot(D_{\mathrm{k}}^{\mathrm{eff}}\nabla C_{\mathrm{k}})+S_{\mathrm{k}} \tag{4}$$

where C_{k} is the concentration of species and $D_{\mathrm{k}}^{\mathrm{eff}}$ represents the diffusivity, which is given for porous material by Bruggeman equation as follows

$$D_{\mathrm{k}}^{\mathrm{eff}}=\varepsilon_{\mathrm{m}}^{1.5}D_{\mathrm{k}} \tag{5}$$

The species production term S_{k} is related to electrochemical reaction in the fuel cell which is given in the following form

$$S_{\mathrm{k}}=-\frac{M_{\mathrm{w,k}}}{nF}R_{\mathrm{j}} \tag{6}$$

where k shows the specie, n is the electron transfer number, and subscript j used for anode or cathode.

Energy conservation equation is given as follows

$$\frac{\partial(\rho\varepsilon h)}{\partial t}+\nabla(\varepsilon\rho\vec{u}h)=\nabla(k^{\mathrm{eff}}\nabla T)+S_{\mathrm{h}} \tag{7}$$

k^{eff} is the effective thermal conductivity of porous material. The energy source (S_{h}) is a sum of different source terms such as heat of reaction, ohmic loss and electric work and latent heat of evaporation for water, and can be given as

$$S_{\mathrm{h}}=h_{\mathrm{react}}-R_{\mathrm{an,cat}}\eta_{\mathrm{an,cat}}+I^2R_{\mathrm{ohm}}+h_{\mathrm{L}} \tag{8}$$

The equation for conservation of charge is given as

$$\nabla\cdot(\sigma_{\mathrm{e}}^{\mathrm{eff}}\nabla\Phi_{\mathrm{e}})+S_{\Phi}=0 \tag{9}$$

where Φ_{e} is the charge potential for membrane or solid phase, $\sigma_{\mathrm{e}}^{\mathrm{eff}}$ is the ionic conductivity, S_{Φ} is the source term which depends on exchange current density (A/cm^2). The dependence of exchange current density on reactant concentration can be expressed by Butler-Volmer's [13] equation. Simplified form of which known as Tafel equation is given below

$$S_{\Phi}=\begin{cases} I_{\mathrm{an}}=I_{\mathrm{an}}^{\mathrm{ref}}\left(\dfrac{[\mathrm{H_2}]}{[\mathrm{H_2}]_{\mathrm{ref}}}\right)^{\gamma_{\mathrm{an}}}\left(e^{\alpha_{\mathrm{an}}F\eta_{\mathrm{an}}/RT}\right) \\ I_{\mathrm{cat}}=I_{\mathrm{cat}}^{\mathrm{ref}}\left(\dfrac{[\mathrm{O_2}]}{[\mathrm{O_2}]_{\mathrm{ref}}}\right)^{\gamma_{\mathrm{cat}}}\left(e^{-\alpha_{\mathrm{cat}}F\eta_{\mathrm{cat}}/RT}\right) \end{cases} \tag{10,11}$$

where I^{ref} is the reference exchange current density, γ is the concentration dependence factor, α is the transfer coefficient, F is Faraday constant, and η is the overpotential.

PEM properties

PEM proton conductivity (σ_{mem}) is related to membrane water content (λ) and temperature by following equation

$$\sigma_{\mathrm{mem}}=(0.514\lambda-0.326)\ e^{1268\left(\frac{1}{303}-\frac{1}{T}\right)} \tag{12}$$

The membrane water transport by osmotic drag is given by the following relation [11]

$$J_W^{\text{drag}} = \alpha_{\text{d}} \cdot (2I) \tag{13}$$

The osmotic drag coefficient (α_{d}) for proton conductivity of membrane also depends upon λ and is related by following equation

$$\alpha_d = 2.5\frac{\lambda}{22} \tag{14}$$

The back diffusion flux of water molecules through membrane can be related to λ as

$$J_W^{\text{diff}} = -\frac{\rho_{\text{m}}}{M_{\text{m}}} M_{\text{H}_2\text{O}} D_{\text{l}} \nabla\lambda \tag{15}$$

where ρ_{m} and M_{m} are density and equivalent weight of dry membrane. The diffusion coefficient, D_{l}, is represented by the following equation

$$D_{\text{l}} = e^{2416\left(\frac{1}{303}-\frac{1}{T}\right)}(2.563 - 0.33\lambda + 0.0264\lambda^2 - 0.000671\lambda^3)\times 10^{-6} \tag{16}$$

Water content of membrane was estimated using equation [11] as follows

$$\lambda = \begin{cases} 0.043 + 17.18a - 39.85a^2 + 36a^3 & \text{for} \quad a < 1 \\ 14 + 1.4(a-1) & \text{for} \quad a > 1 \end{cases} \tag{17}$$

where *a* is water activity and is defined mathematically as:

$$a = \frac{P_{\text{WV}}}{P_{\text{sat}}} \tag{18}$$

The vapor pressure can be related to molar fraction and total pressure as follows:

$$P_{\text{WV}} = \text{x}_{\text{H}_2\text{O}} P \tag{19}$$

Model parameters and boundary conditions

The simulations were carried out at steady state and non-isothermal conditions. The reaction parameters were set at 1 atm and 353 K (80°C). Output voltages were calculated at a fixed current density of 0.6 A/cm^2. Flow rate for hydrogen gas was set at 0.4 SLPM (9.477×10^{-7} kg/s) and for air at 1.26 SLPM (2.82×10^{-5} kg/s). Both streams were entered with 100 % relative humidity. The model was calibrated in order to generate comparable solutions with the experimental results by tuning the reference exchange current density. The model parameters are presented in Table 2.

Table 2. *Model parameters*

Quantity	Value
Anode reference current density [31]	100 A m^{-2}
Anode reference molar concentration [31]	0.04 kmol m^{-3}
Anode concentration exponent [17]	0.5
Anode exchange coefficient [32]	0.5
Cathode reference exchange current density	0.00035 A m^{-2}
Cathode reference molar concentration [31]	0.04 kmol m^{-3}
Cathode concentration exponent [17]	1
Cathode exchange coefficient	0.6
Open circuit voltage	1.05 V
Hydrogen reference diffusivity [31]	1.1028×10^{-4} m^2 s^{-1}
Oxygen reference diffusivity [31]	3.2348×10^{-5} m^2 s^{-1}
Water reference diffusivity [31]	7.65×10^{-5} m^2 /s s^{-1}
Nitrogen reference diffusivity [31]	3×10^{-5} m^2 s^{-1}

Material properties

In order to solely recognize the effect of thermal conductivity and porosity of GDL its other properties were taken identical in all solutions. Isotropic model was adopted for specifying the values of viscous and electrical resistances. The properties of materials used in this model are given in Table 3.

Table 3. *Material properties*

Material	Property	Value
Nafion	Density	1968 kg m^{-3}
	Specific heat capacity	4188 J kg^{-1} K^{-1}
	Thermal conductivity, dry at 65°C	0.12 W m^{-1} K^{-1}
	Equivalent weight	1100 kg $kmol^{-1}$
Toray Carbon	Bulk density	440 kg m^{-3}
	Specific heat capacity	685 J kg^{-1} K^{-1}
	Electrical conductivity	1250 Ω^{-1} m^{-1}
	Viscous resistance	1.02×10^{11} m^{-2}
Platinum, Pt	Thermal conductivity at 60°C	73 W m^{-1} K^{-1}
Carbon support (Vulcan XC 72)	Bulk density	264 kg m^{-3}
	Specific heat capacity	685 J kg^{-1} K^{-1}
	Thermal conductivity	7.63 W m^{-1} K^{-1}
	Electrical conductivity	400 $\Omega^{-1}m^{-1}$
Graphite Plate	Density	1990 kg m^{-3}
	Specific heat capacity	710 J kg^{-1} K^{-1}
	Thermal conductivity	117 W m^{-1} K^{-1}
	Electrical conductivity	92600 $\Omega^{-1}m^{-1}$

Solver specification

A finite volume based FLUENT® solver was implemented to solve the governing equations. The large scale computational domain was handled by parallel processing technique. The URFs are employed to control the solution of highly coupled equations. To achieve convergence the URFs were tuned to an optimum value in order to lower the residuals for each variable without large oscillations. About 700 iterations were performed to achieve converged solutions. Stopping criteria was set at a residual value of 1×10^{-6} for the equation of continuity and 1×10^{-5} for other variables (*i.e.* potential fields, water content, species outlet mole fractions etc.) which took more time to converge than the scaled residuals.

Results and discussion

Grid independence study

To make sure that the large-scale model is independent of the meshing criteria the model was meshed with three different sizes as sown in Table 4. The current densities were calculated for each mesh size at a fixed potential of 0.67 V. About 8.5 % deviation in the criterion parameter was found when mesh size was increased from 1 to 1.3 million cells. The deviation reduced to about 4.4% when mesh size was further increased to 1.8 million cells. The study showed that the deviation diminished as the mesh became finer. Due to high computational load the grid size with 1.3 million computational cells was selected for all the calculations.

Table 4. *Average current* densities *for different mesh sizes at 0.67 V*

Mesh	Cells	Average CD, A cm^{-2}
Fine	1858725	0.425
Medium	1352475	0.408
Coarse	1099350	0.375

Experimental validation

The simulation results were validated with experimental data by comparing the polarization curves, as shown in Figure 4. In-house experiments were carried out to generate a polarization curve. A standard test PEM fuel cell with 50 cm^2 active area, developed by Electro Chem Inc. was used for experiments at 50°C temperature and atmospheric pressure. Toray carbon (TP 60) material was used as GDL and the catalyst layer was made with Pt nanoparticles on carbon substrate (0.2 mg Pt/mg Vulcan XC 72) with loading of 1 mg cm^{-2}. The measurement of current density was carried out by galvanostatic control. Fuel cell testing system (FCTS) was employed for data acquisition. Constant gas flow rates were chosen throughout the experiments to achieve a minimum stoichiometry of 1.5 and 2 for hydrogen and oxygen at 0.8 A cm^{-2}.

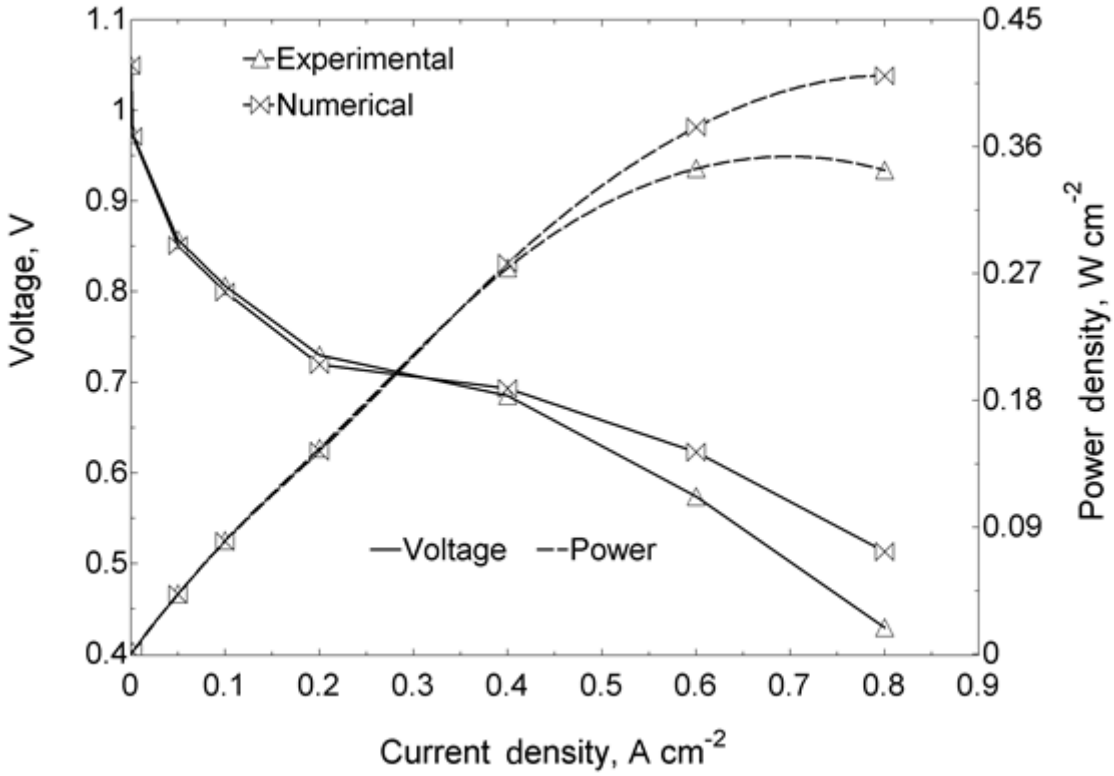

Figure 4*. Polarization and power density curves at 50 °C and 1 atm*

A good agreement was achieved as the numerical results followed the experimental curve as shown in Figure 4. However, at high current densities above 0.4 A cm^{-2} the curve for numerical solution deviated due to inadequacy of the model to reproduce the actual behavior of PEMFC. At high current density, the concentration overpotential dominate the cell performance as water droplets blocks the diffusion pathways for reactants to reach reaction sites as depicted by the experimental curve. However, the discrepancies at high current density could be minimized by decreasing the URFs for saturation source term and membrane water content but the number of iterations would be very high and would result in stalling of convergence.

Effect of GDL thermal conductivity

Commercially available data [32] for four types of carbon fiber paper used as GDL was incorporated namely Toray carbon, E-Tek, Spectracarb and Sigarcet. The effect of thermal conductivity of GDL on the water content and temperature of PEM is illustrated by contours shown in Figure 5 and 6 which represent the iso-surface at the middle of PEM. Figure 5 shows the overall decrease in water content (λ) of PEM with thermal conductivity of GDL.

The gradual increase of water content (Figure 5) along the channel clearly shows the saturation of the reactant gas with product water generated by ORR which is removed through GDL. PEM drying is evident in Figure 5 as GDL thermal conductivity is decreased from 1.7 to 0.16 W / m K. The drying phenomenon is related to high temperature operation as shown in Figure 6.

The effect of GDL thermal conductivity on PEM temperature is distinctively revealed in Figure 6. PEM temperature increased as GDL thermal conductivity is reduced from 1.7 to 0.16 W / m K. Moreover, a low temperature profile is eminent in both Figures making an interdigitated pattern in the regions under the rib where water accumulates due to low gas flow. The temperature of membrane plays a significant role in the PEMFC performance. High temperature causes drying and consequently lowers the proton conductivity (σ_{mem}).

Moreover, enhanced proton conductivity of PEM effectively reduced the ohmic overpotential which resulted in high output voltages as depicted in Figurer 7 which shows the calculated output voltages for each GDL at fixed current density of 0.6 A cm^{-2}.

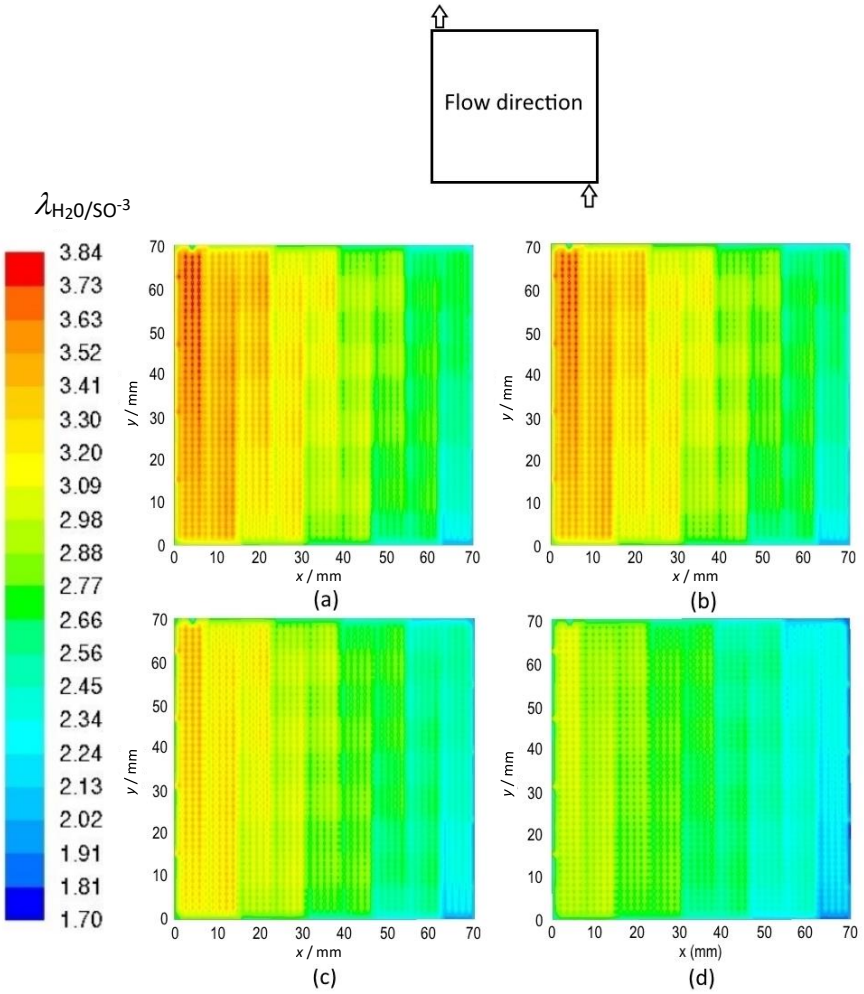

Figure 5. *Contours of PEM water content (λ) at GDL thermal conductivity of* ***(a)*** *1.7 W/m K;* ***(b)*** *1.4 W / m K;* ***(c)*** *0.6 W / m K;* ***(d)*** *0.16 W / m K*

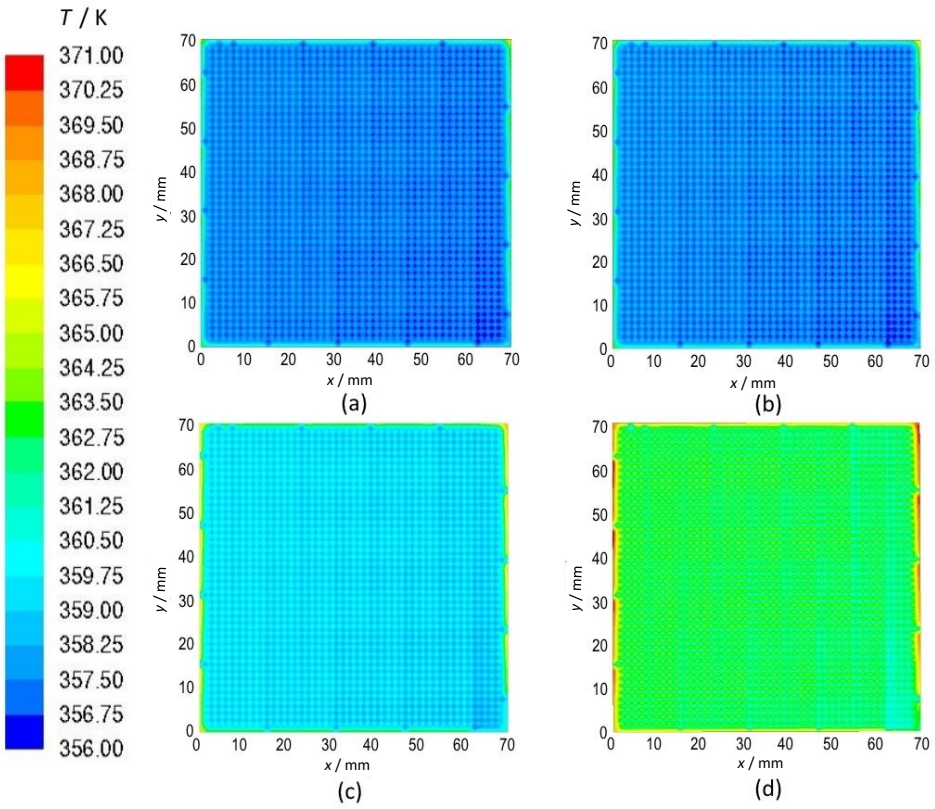

Figure 6. *Temperature, K contours of PEM at GDL thermal conductivity of* ***(a)*** *1.7 W / m K;* ***(b)*** *1.4 W / m K;* ***(c)*** *0.6 W / m K;* ***(d)*** *0.16 W / m K*

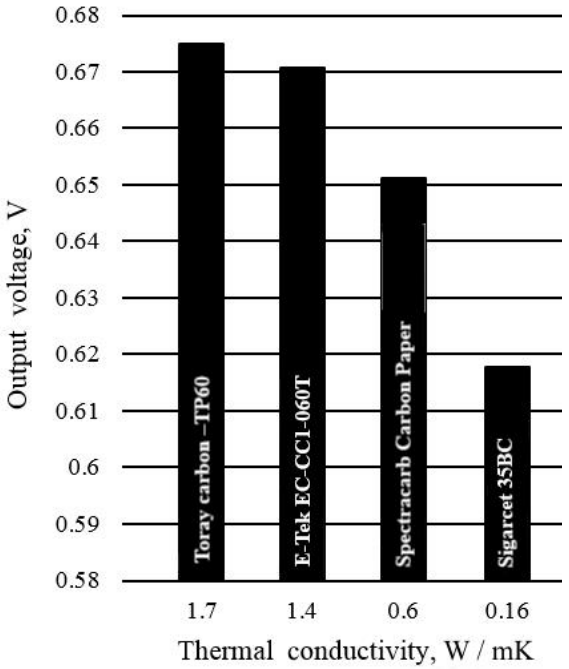

Figure 7. *Output voltages at different GDL thermal* conductivities

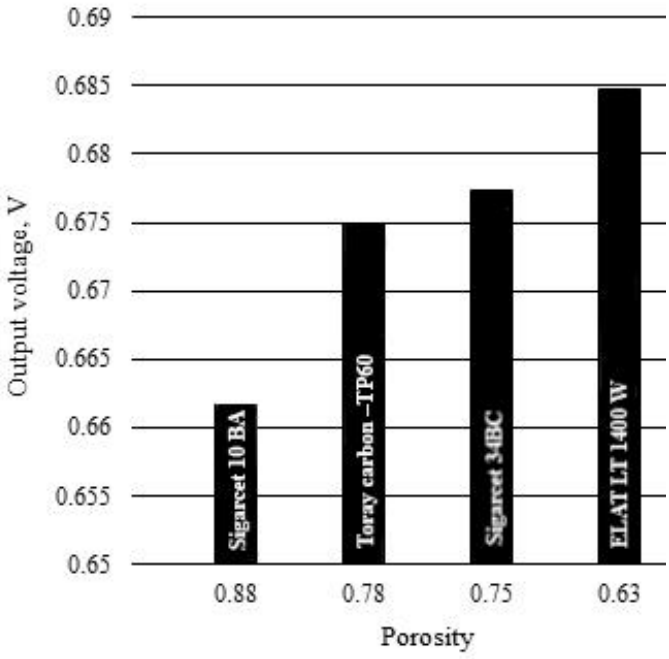

Figure 8. *Output voltages at different GDL porosities*

Effect of GDL porosity

Among other functions of GDL the distribution of reactant gases to the active surface area of CL is very critical. The diffusivity of gases highly depends upon the porosity of material as shown in Equation 5. A highly porous GDL will lead to better transport of reactant gases. On the other hand, high porosity promotes contact resistance between GDL and bipolar plate which reduces electrical

conductivity [33]. Therefore, an optimum porosity is desired for efficient process. Figure 8 shows the output voltages that are generated by the simulations at different GDL porosities obtained from commercially available data. The results depict that the output voltage was increased as the porosity of GDL was lowered from 0.88 to 0.63 due to improved electrical conductivity which indicate reduced contact resistance.

The effect of GDL porosity on reaction rate at GDL-catalyst interface on cathode side of PEMFC is shown in Figures 9 and 10. The GDL was treated as a single domain with uniform porosity. A subtle change is noticeable in both contours of Figure 9 which represents mole fraction of oxygen that increased from 0.1 to 0.22 along the channel. The results showed that oxygen was diffused at a higher rate in GDL with 0.88 porosity (Figure 9(a)) than with 0.63 porosity (Figure 9(b)). Furthermore, pathways of gas to CL are obstructed in the regions under the rib which exhibit the accumulation of water.

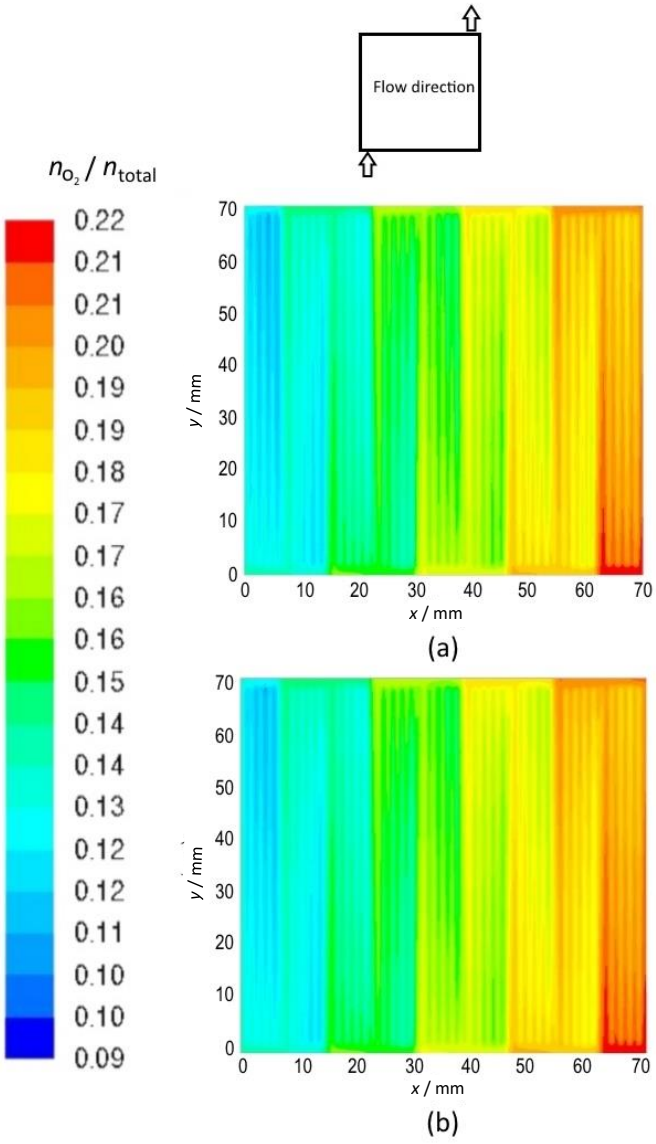

Figure 9. *Oxygen mole fraction at cathode side GDL-catalyst interface at GDL porosity of* ***(a)*** *0.88;* ***(b)*** *0.63*

The heat generated in the ORR is illustrated in Figure 10. A considerable change in both diagrams 10(a) and 10(b) is noticed which signifies the dependence of ORR rate on GDL porosity. Product heat was increased along the channel corresponding to the same phenomenon represented in Figure 9. Heat accumulated under rib while in the channel it was swept away by the gas stream. This suggests that an optimum porosity of GDL is highly decisive in efficient performance of PEMFC.

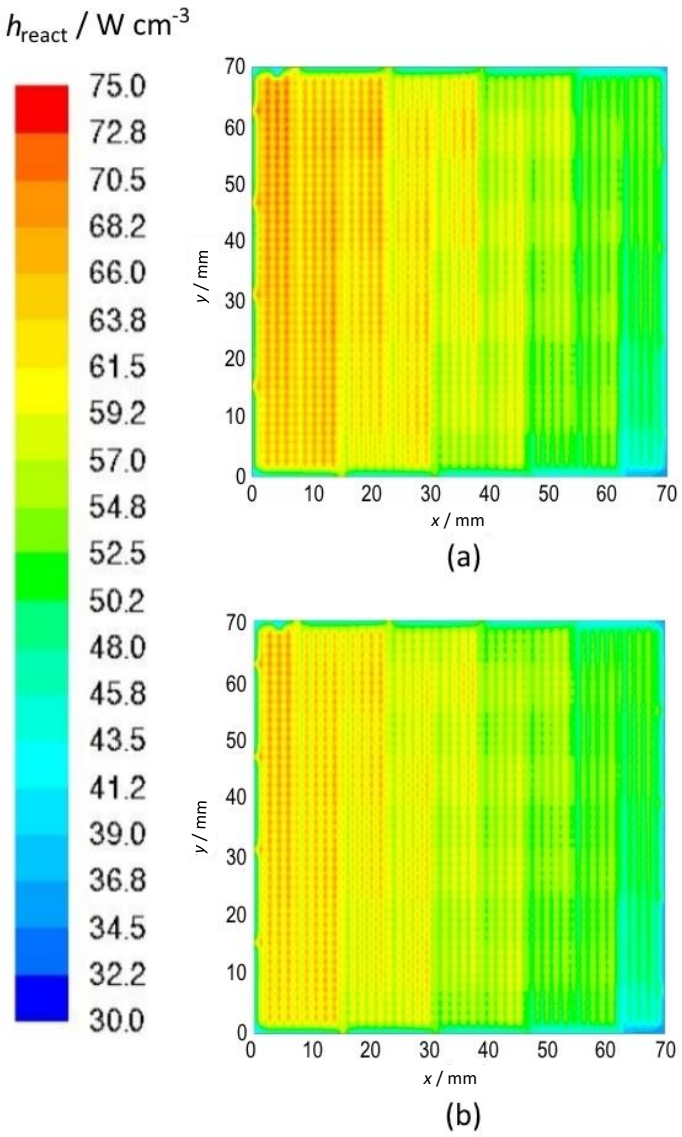

Figure 10. *Reaction heat source (W/cm^3) at GDL-catalyst interface at GDL porosity of* ***(a)*** *0.88;* ***(b)*** *0.63*

Conclusions

This study provides a numerical investigation of the effect of thermal and transport properties of GDL on the performance of PEMFC. The mathematical model was validated with experimental results by the comparison of the polarization and power density curves. Contours of different iso-surfaces were presented to show the impact of thermal conductivity and porosity of GDL on the electrochemical behavior of PEMFC. The results provide a substantial basis in understanding the actual phenomenon occurred inside the complex system of fuel cell. It is reported that higher thermal conductivity of GDL led to improved proton conductivity of PEM by maintaining low temperatures. It is also found that higher porosity of GDL promoted the reactant gas transport to CL but at the same time raised contact resistance which resulted in lower electrical conductivity. The compressive force in the cell also affected the performance by impeding the gas flow through porous GDL. These results suggest that the optimum GDL characteristics and compressive force is required for maximum efficiency of PEMFC.

Further study can be done by incorporating other GDL properties like gas permeability, thickness, electrical conductivity and interface resistance between the layers adjacent to GDL.

References

[1] M. F. B. Sunden, *Transport Phenomena in Fuel Cells (Developments in Heat Transfer)*. WIT Press, Southampton, UK, 2005.
[2] N. Sammes, Fuel Cell Technology Reaching Towards Commercialization. Springer, London, UK, 2006.
[3] X. L. David P. Wilkinson, Jiujun Zhang, Rob Hui, Jeffrey Fergus, *Proton Exchange Membrane Fuel Cells: Materials Properties and Performance*. CRC Press, Florida, USA, 2009.
[4] M. M. Mench, *Fuel Cell Engines*. John Wiley & Sons, Hoboken, USA, 2008.
[5] U. Pasaogullari, C. Y. Wang, *J. Electrochem. Soc.* **151(3)** (2004) A399–A406.
[6] P. C. Rieke, N. E. Vanderborgh, *J. Memb. Sci.* **32(2)** (1987) 313–328.
[7] N. Parikh, J. S. Allen, R. S. Yassar, *Fuel Cells* **12(3)** (2012) 382–390.
[8] R. Banerjee, J. Hinebaugh, H. Liu, R. Yip, N. Ge, A. Bazylak, *Int. J. Hydrogen Energ.* **41(33)** (2016) 14885–14896.
[9] Y. Zhang, A. Verma,R. Pitchumani, *Int. J. Hydrogen Energy* **41(20)** (2016) 8412–8426.
[10] Y. Gao, A. Montana, F. Chen, *J. Power Sources* **342** (2017) 252–265.
[11] T. E. Springer, T. A. Zawodzinski, S. Gottesfeld, *J. Electrochem. Soc.* **138(8)** (1991) 2334–2342.
[12] T. V NguyenR. E. White, *J. Electrochem. Soc.* **140(8**) (1993) 2178–2186.
[13] S. Um, C.-Y. Wang,K. S. Chen, *J. Electrochem. Soc.* **147(12)** (2000) 4485–4493.
[14] H. Ju, H. Meng, C. Y. Wang, *Int. J. Heat Mass Transf.* **48** (2005) 1303–1315.
[15] K. W. LumJ. J. McGuirk, *J. Power Sources* **143(1)** (2005) 103–124.
[16] Y. Wang and C.-Y. Wang, *J. Electrochem. Soc*. **153(6)** (2006) A1193–A1200.
[17] Y. M. FerngA. Su, *Int. J. Hydrogen Energ.* 32(17) (2007) 4466–4476.
[18] A. A. Shah, G.-S. Kim, P. C. Sui, and D. Harvey, *J. Power Sources* **163(2)** (2007) 793–806.
[19] A. D. LeB. Zhou, *J. Power Sources* **182(1)** (2008) 197–222.
[20] Y. Wang, S. Basu, C.-Y. Wang, *J. Power Sources* **179(2)** (2008) 603–617.
[21] J. J. BaschukX. Li, *Appl. Energy* **86(2)** (2009) 181–193.
[22] Z. Zhang, X. Wang, X. Zhang, L. Jia, *J. Fuel Cell Sci. Technol.* **5(3)** (2008) 31007–31009.
[23] Inamuddin, T. A. Cheema, S. M. J. Zaidi, S. U. Rahman, *Renew. Energ.* **36(2)** (2011) 529–535.
[24] I. Khazaee, M. Ghazikhani, M. N. Esfahani, *Appl. Surf. Sci.* **258(6)** (2012) 2141–2148.
[25] N. Alhazmi, D. B. Ingham, M. S. Ismail, K. J. Hughes, L. Ma, M. Pourkashanian, *Int. J. Hydrogen Energ.* **38(1)** (2013) 603–611.
[26] D. M. Fadzillah, C. L. Nee, M. I. Rosli, *Int. J. Mechan. Mechatron. Eng.* **15(5)** (2015) 83–89.
[27] N. H. Maslan, M. M. Gau, M. S. Masdar, M. I. Rosli, *J. Eng. Sci. Technol.* **11(1)** (2016) 85–95.
[28] N. Djilali, *Energy* **32(4)** (2007) 269–280.
[29] C. Siegel, *Energy* **33(9)** (2008) 1331–1352.
[30] W. M. H. Versteeg, *An Introduction to Computational Fluid Dynamics: The Finite Volume Method*, Second. Pearson Education Limited, London, UK, 2007.
[31] S. Kamarajugadda S. Mazumder, *Comput. Chem. Eng.* **32(7)** (2008) 1650–1660.
[32] A. Pfrang, D. Veyret, G. Tsotridis, *Convection and Conduction Heat Transfer*, Intech, Rijeka, Croatia, 2011, p. 215.
[33] Y.-X. Huang, C.-H. Cheng, X.-D. Wang, J.-Y. Jang, *Energy* **35(12)** (2010) 4786–4794.